Title
High-resolution U-Pb Geochronology of Terrestrial Cretaceous-Paleogene and Permo-Triassic Boundary Sequences in North America

Author
Mitchell, William

Publication Date
2014

Peer reviewed|Thesis/dissertation

High-resolution U-Pb Geochronology of Terrestrial Cretaceous-Paleogene and Permo-Triassic Boundary Sequences in North America

by

William Stuart Mitchell, III

A dissertation submitted in partial satisfaction of the

requirements for the degree of

Doctor of Philosophy

in

Chemistry

in the

Graduate Division

of the

University of California, Berkeley

Committee in charge:

Professor Paul Renne, Co-chair
Professor Evan Williams, Co-chair
Professor Heino Nitsche
Professor Donald DePaolo

Spring 2014

High-resolution U-Pb Geochronology of Terrestrial Cretaceous-Paleogene and Permo-Triassic Boundary Sequences in North America

Abstract

High-resolution U-Pb Geochronology of Terrestrial Cretaceous-Paleogene and Permo-Triassic Boundary Sequences in North America

by

William Stuart Mitchell, III

Doctor of Philosophy in Chemistry

University of California, Berkeley

Professor Paul Renne, Co-chair

Professor Evan Williams, Co-chair

High-resolution geochronology provides a means to evaluate the timescales of responses to major shifts in Earth history, such as ecosystem recovery following a major impact event or a mass extinction. Additionally, geochronology can be used to correlate sections across the marine and terrestrial realm and around the world. Changes in ecosystems or isotopic composition of deposited rocks will be influenced by local effects, but can also have a global signal. With geochronlogy, the same time interval can be found in distant regions, and if a phenomenon (e.g. a carbon isotope excursion) was global in scope, many different localities each from the same time interval would show the same signal.

Here I present high-resolution uranium-lead geochronology pertaining to two mass extinctions: the Cretaceous-Paleogene mass extinction (around 66 million years ago, Ma) and the Permo-Triassic mass extinction (around 252 Ma). In the first chapter, I introduce some of the complexities involved in using the rock record to piece together a picture of life on Earth back in time. Dating volcanic ash deposits (tephra) with uranium-lead geochronology is an important piece of the puzzle. In the second chapter, the chemical, analytical, and statistical methods used are presented in detail. Analyses of several reference materials are included, which illustrate the precision and accuracy attainable with these methods. The third chapter applies these high-resolution dating techniques to the Cretaceous-Paleogene boundary in Northeastern Montana. Although one of the volcanic ash deposits in the area has been dated by $^{206}Pb/^{238}U$, more than forty distinct volcanic ash deposits have been identified. Here I present new data on 12 samples representing at least 10 distinct tephra, at a precision and accuracy much higher than in the previous uranium-lead work. In the fourth chapter, $^{206}Pb/^{238}U$ techniques are again applied to volcanic tephra, this time in a section in the Texas Panhandle believed to be of latest Permian age, though possibly earliest Triassic. With extremely few fossils preserved, determining a precise age can only be done through radioisotopic geochronology. One such study used the K-Ar method, but the uncertainties in age were 4 million years. The new ages I have determined place this section within uncer-

tainty ($\leq$500 thousand years) of the global stratotype section and point at Meishan, China, and one tephra is distinctly younger than the boundary.

This work lays the foundation for other studies. Paleontologists studying the latest Cretaceous and earliest Paleogene in Northeastern Montana can use the dates provided here to constrain the age of fossil localities and develop a regional biochronology. It also allows for comparison with $^{40}Ar/^{39}Ar$ geochronology, and the combination of the two can be used to calibrate the geomagnetic polarity timescale. Determining the age of strata in the Texas Panhandle will enable stratigraphers to determine whether shifts in the carbon and oxygen isotope records are occurring at the Permo-Triassic boundary. Paleontologists will also be able to make use of these new dates to guide their interpretation of rare microfossils found in the rocks surrounding the volcanic ash bed.

To Beth and Johannah

For their support, in absence and in presence, throughout this great journey.

Contents

List of Figures

List of Tables

Acknowledgments

This work is the result of the support of many people, chief among them Paul Renne and Roland Mundil, my advisers, for whose support I am very thankful. I also thank Evan Williams, Heino Nitsche, and Don DePaolo for their time, comments, and willingness to serve on my dissertation committee.

Thanks also to many other faculty who have been of great help on these projects, including Bill Clemens, Walter Alvarez, Cindy Looy, David Shuster, Seth Finnegan, Mark Richards, Steve Self, Neil Tabor, and John Geissman. The staff and students at the Berkeley Geochronology Center also have my thanks, particularly Warren Sharp, Francoise Spaulding-Keller, Christina Polito Halter, Nick Fylstra, Abed Jaouni, Ryan Ickert, Regina Mertz, Steve Denyzyn, Courtney Sprain, Marissa Tremblay, and William Cassata. I also thank Sean Mulcahy, Dylan Collins, and Tim Teague.

My officemates past and present deserve thanks as well, not only for their support and advice but for their assistance with the daily trivia questions: Kathleen, Heidi, Daniella, Marisa, Christian, Haopeng, Hyojin, John, Amadu, and Emily. Thanks to the EPS department for being so welcoming to an outsider, and the chemistry gamenights group for all the fun games.

Furthermore, my thanks go to those far afield who have been so willing to talk with me about how things are going, including Kestrel, Katie, Kristine, Karen, Kisha, Sarah, Leah, Maria, Maraia, Megan, Rex, Bitsy, the Graces, John, Joanna, and Jen. Thanks to the UC Berkeley Amateur Radio Club (W6BB), in particular Jack, Fritz, Chris, and Anita, for their willingness *not* to talk with me about how things are going but to encourage me talk to people all around the world.

I have also received an incredible amount of support, inspriation, and encouragement from the staff and volunteers at the Lawrence Hall of Science. Of those, I would especially like to thank Gretchen Walker, Elizabeth Stage, Sue Guevara, Megan Gray-Banes, Sherry Hsi, Dustin Perry, Timothy Hurt, Terry Chang, and Deborah Wang.

I give my thanks to those people who supported me in my studies before graduate school: Margaret Wong, Chelen Johnson, Beckie Alexander, Evan Jones, Brad Kohl, Lois Fruen, Virginia Amundson, Tom Hegg, Gretchen Hofmeister, Marion Cass, Bereket Haileab, and Jerry Mohrig.

A most special thanks goes Beth and Johannah, to whom this work is dedicated, for their editorial assistance, advice, inspiration, and love.

Finally, I thank my family—my parents, aunts, uncles, cousins, and grandparents—for their love, support, and interest in my graduate work.

Chapter 1

Introduction

What does a mass extinction look like as it happens? Does it occur over the course of a few days, a few years, or a hundred thousand years? What mechanisms are in play during the extinction event, and what are the typical causes of death for the individuals, species, and higher-order taxa? As the changes in ecosystems across the globe have become rapid in the anthropocene, it is possible that the beginning of the next mass extinction has started (*1*). Understanding the mass extinctions of the past could be key to guiding decisions to avert an impending mass extinction, to adapt so that the extinction is less severe, or to determine that the changes in ecosystems is not consistent with a mass extinction.

These questions are the driving motivation for the two studies in radioisotopic dating presented here. Although it may be impossible to answer these questions to the full degree of detail which is asked for, a high-resolution record of mass extinctions could still yield enlightening results. Rates of ecological change can be better understood, distant sections from marine, terrestrial, and transitional environments can be linked in space and time, and other chemical and isotopic data can be brought together.

Our understanding of Earth history stems from several records: geochronologic, biostratigraphic, chemostratigraphic, and magnetostratigraphic. Each has its own story to tell. However, the pieces only fit together if we understand the sequence of events. In this chapter, I will discuss how these different records inform how we think about events in Earth history—such as the fossil record across mass extinctions—and how those records can be combined with geochronology or how they benefit from high-resolution geochronology. In Chapters 3 and 4, I will apply the $^{206}Pb/^{238}U$ dating techniques discussed both later in this chapter and in Chapter 2 to two systems: the Cretaceous-Paleogene Boundary ($\sim$66 million years ago) and the Permo-Triassic Boundary ($\sim$252 million years ago).

To the best of my knowledge, this study is the first in more than 30 years to use $^{206}Pb/^{238}U$ dating to determine the age of strata in Northeastern Montana at the very end of the Cretaceous and into the Paleogene (*2*). Many advances in techniques have been made since the previous studies. The results presented in Chapter 3 provide more accurate, higher-precision dates than the previous work, and cover a wide stratigraphic and areal range, including numerous important paleontological sites.

Chapter 4 presents data for an enigmatic section in the Texas Panhandle, of an age which roughly matches the Permo-Triassic Boundary. Some previous studies have assigned a Triassic age for the strata, others have emphatically argued that the strata are Permian. Extremely few fossils are present, rendering biochronology practically useless. The iron-bearing, oxidized strata are good recorders of paleomagnetism, but because polarities are non-unique, there needs to be some other means to establish an absolute age from which to count reversals. Precise dating of these strata would influence interpretations of whether carbon and oxygen isotope excursions at the Permo-Triassic Boundary are a global phenomenon, or whether they are regional or local effects: in order to evaluate what was happening in the isotopic records at a given time, it is important to be able to pinpoint where in the record that time is found. While a little work has been done here using $^{206}Pb/^{238}U$ geochronology (*3*), only three strata were dated, some of them with techniques which are no longer state-of-the-art. There have also been $^{40}Ar/^{39}Ar$ (*3*) and $^{40}K/^{40}Ar$ (*4*) dates collected here, although the uncertainties were much larger than what should be available with modern $^{206}Pb/^{238}U$ dating.

1.1 Biostratigraphy

Studying mass extinctions necessarily involves facing the challenges surrounding the paleontological data. Chief among them is the incompleteness of the fossil record; indeed, preservation is generally rare. The consequences of this incompleteness manifest in several different ways, including the Signor-Lipps effect (*5*) and through Lazarus taxa.

The Signor-Lipps effect is premised on how the incompleteness of the fossil record will assure that any fossil that is found will be neither the true first appearance, nor the last. Within the strata leading up to an instantaneous extinction event, different species will have varying levels of last appearances (*5*), an effect which will be particularly pronounced for large species and rare species. These varying species-specific extinction levels can make it easy to erroneously conclude that the extinction is protracted, even though in actuality the event was abrupt. Similarly, first appearances are only a recent limit on the true first appearance, so it is possible for a species to have inhabited two sections simultaneously, but the first appearance may be stratigraphically—and more importantly, chronologically—different (*6*).

Additionally, the amount of sampling has an effect on the apparent diversity. As more samples are collected, the chances that rare taxa are found will increase. Signor and Lipps demonstrated this with a general correlation between the area of deposited sediments and the species richness (*5*). While this effect is not necessarily important for the specific conclusions drawn in this dissertation, these are biases which need to be considered, and which may have bearing on the validity of conclusions made in cited references.

Lazarus taxa provide another cautionary tale about interpreting the evidence of taxonomic absence as evidence for extinction. Species which appear to have become extinct in the fossil record, yet are found occurring later seemingly unscathed are termed Lazarus taxa,

after the biblical character who came back from the dead (*7*). In these cases, while species may become extirpated, there is some refuge elsewhere that allows the species to survive and reappear later hundreds of thousands of years later. Such instances can provide an estimate of biases in sampling which do not necessarily reflect true extinction events, but rather artifacts of preservation (*7*).

Hiatuses in deposition and preservation can make continuous processes of diversification and extinction appear as an abrupt turnover in fossil assemblages (*8*). Unless the stratigraphic section is known to have no hiatuses, or the hiatus can be demonstrated to be brief, it is impossible to rule out this type of bias in the data.

Identifying taxa and quantifying richness is not an exact science either. In 1997, paleontologists (Gerta Keller and Jan Smit) working on the Cretaceous-Paleogene extinction who held vastly differing views on the tempo and duration of the event agreed to have a blind test. That test would be resistant to arguments that one dataset was obtained in a much different fashion than another (*9–18*). Four micropaleontology laboratories, each independent of the two main investigators, were given splits of samples collected in El Kef, Tunisia, but were not told what the stratigraphic order was of the samples (*10*, *11*). Each of the four laboratories reported results (*12–15*), and those results were then given to Keller (*16*) and Smit (*17*). Of the reported results, there were large discrepancies in number species identified within identical samples, and in the abundances of those species. Significant discrepancies also existed in the biostratigraphic ranges of the taxa. In short, while the blind test failed to solve the question of the tempo of the marine extinction observed at El Kef, it succeeded in highlighting the challenges associated with biostratigraphy and interpreting fine-scale paleontological data.

1.2 Paleomagnetism

Throughout Earth's history, the magnetic pole has changed polarity sporadically. As rocks containing magnetic minerals cool or are deposited, their net magnetic moment will align with the prevailing magnetic field direction. If they are subsequently kept under their Curie temperature (among other constraints), they will provide a record of the paleomagnetic field direction. Because the dipolar magnetic field is assumed to be a global phenomenon throughout Earth's history, two rocks which were deposited or cooled at the same time will record the same magnetic polarity. Thus if the ages of the reversals are known, the magnetic record can provide a tool with which to constrain the age of a rock even in the absence of material which can be dated via radioisotopic means.

Unfortunately, a magnetic polarity datum in isolation does not an age provide, and the polarities are non-unique. Sections which are amenable to radioisotopic dating or other absolute dating methods can be and have been used to calibrate the geomagnetic polarity timescale (*19*). Once calibrated, and with at least one tie-point to determine where in the calibrated GPTS an unknown section occurs, the paleomagnetic record can yield constraints on age even in the absence of radioisotopic dates.

Paleomagnetism can also be used as a rough correlative tool. Synchronously deposited strata will record the same magnetic polarity: thus if two strata from different sections preserve opposite magnetic polarity, they cannot have been deposited simultaneously. Put another way, to be correlative, two strata must preserve the same magnetic polarity.

1.3 Chemostratigraphy

Coincident with many of the major mass extinctions are excursions in the isotopic record of minerals precipitated at that time. The main signature is found in marine carbonate, which can record variations in oxygen and carbon isotopic compositions, as well as calcium and magnesium. Isotopic signatures in carbonate reflect the isotopic signature of the oxygen and carbon present when they formed. These isotopes in turn are influenced by changes in the hydrologic and carbon cycles. A cooling world will lead to more massive ice caps and glaciers, which are preferrentially enriched in light isotopes of hydrogen and noxygen. Changing rates of carbon fixation, weathering, CO_2 emission, and carbon burial will affect the carbon isotopic record.

In strata spanning both the Cretaceous-Paleogene event (∼66 Ma) and the Permo-Triassic event (∼252 Ma), a significant change in carbon isotopic composition is observed (*20–24*). Such excursions are thought to be of global scope, and reflect a major shift in the carbon cycle. To the extent that these phenomena occur globally, finding such an isotopic shift could be a geochemical proxy for the boundary of interest, since such rapid and dramatic shifts in isotopic composition appear only rarely in the geologic record.

Calcite $^{44}Ca/^{40}Ca$ from southern China exhibits an excursion toward less ^{44}Ca coincident with the Permo-Triassic mass extinction and with the carbon isotope excursion (*25*). Not only is this record preserved in the calcite, but conodont teeth from Meishan, China, also record a shift of the same magnitude, duration and timing (*26*). When the flux of calcium into the oceans from continental weathering and the flux out due to carbonate deposition are in steady-state, the isotopic composition of seawater is steady. However, if deposition becomes rapid, the calicum isotopic composition can deviate from the steady-state composition. Hinojosa *et al.* (*26*) found that the conodont tooth record across the boundary is consistent with rapid ocean acidification, which may not be dissimilar from the expected effects of modern carbon-dioxide-induced climate change. Finding similar records in other locations will provide further support for the hypothesis that these changes in calcium isotopes represent global signals rather than local phenomena.

1.4 The Role of Radioisotopic Geochronology

Radioisotopic geochronology of juvenile volcanic tephra (ash deposits) is the most convincing way to establish a chronology of events in Earth history. These dating techniques are not dependent on recognition and differentiation of taxa, on sampling a sufficiently broad

distribution of taxa to infer population statistics, or on biota which occur only terrestrially or only in marine environs. Uranium-lead geochronology in particular provides a tool with which to quantify time in an absolute sense. Even if the tephra in one section comes from a regional eruption, and one seen on the other side of the world comes from another regional eruption, if the uranium-lead ages match, those horizons can be conclusively shown to be synchronous.

Calibrating the geomagnetic polarity timescale is another important role of radioisotopic geochronology. If there are several volcanic tephra and rocks which record a paleogeomagnetic polarity, geochronology can be used to determine the absolute dates of those reversals. Then if there is a section without a suitable tephra, the geomagnetic polarity can be used in combination with other evidence—including biostratigraphy—to then derive absolute ages for events in the section.

For samples in the Phanerozoic (the most recent 541 Ma) that are >1 Ma, two radioisotopic systems are excellent for determining high-precision ages: $^{40}Ar/^{39}Ar$ and $^{206}Pb/^{238}U$. The $^{40}Ar/^{39}Ar$ system is widely applicable, being useful with minerals having significant potassium (e.g. sanidine), because the parent nuclide (^{40}K) is abundant and the daughter nuclide (^{40}Ar) is usually degassed at magmatic temperatures and thus is not usually found within rocks except in minerals containing potassium which have had time to decay.

Measuring the ratio of ^{40}K to ^{40}Ar is extremely difficult, due to the vastly difering chemical properties and ionization efficiencies within a mass spectrometer. To get around this problem, the samples are irradiated with neutrons to convert some of the ^{39}K to ^{39}Ar (*27*). Then, using a standard of known age—often Fish Canyon sanidine (28.294 Ma, Renne *et al.*(*28*, *29*))—the measured $^{40}Ar/^{39}Ar$ ratio of the sample can be used to determine the relative age of the unknown sample compared to the standard. The standard serves to provide a normalization for the percentage of ^{39}K converted to ^{39}Ar.

Because there is a standard, these age determinations are only accurate if the standard age is correct and homogenous; in the case of Fish Canyon sanidine, consensus has yet to be reached (*30–34*). Only natural samples can be used as standards for $^{40}Ar/^{39}Ar$ dating. Synthetically incorporating Ar and K into a solid matrix with a precisely known, non-zero Ar/K ratio is not feasible.

Unlike $^{40}Ar/^{39}Ar$, $^{206}Pb/^{238}U$ geochronology does not involve standardizing to a natural sample of known age. Instead, a synthetic mixture of ^{205}Pb, ^{233}U, and ^{235}U with a very precisely known $^{205}Pb/^{235}U$ is used, allowing the naturally-occurring isotopes in the sample to be directly compared, even if the detection efficiencies of U and Pb within the mass spectrometer are vastly different. U-Pb dating typically uses the mineral zircon ($ZrSiO_4$), which generally incorporates 10–1000 ppm U when it crystallizes, and does not uptake Pb. The non-radiogenic Pb abundances (measured as ^{204}Pb, a non-radiogenic isotope) for samples are no higher than those of laboratory blanks. Because there are two naturally-occurring isotopes of uranium which decay to different isotopes of lead at different rates—^{238}U to ^{206}Pb, and ^{235}U to ^{207}Pb—there is an internal consistency check for the age: both systems should agree if the sample is pristine.

The curve along which the two uranium decay systems agree is termed *Concordia*. In

the absence of other effects, samples wil evolve along that curve. However, if lead is preferentially lost from the system, the sample will fall along a mixing line from the original point on the curve towards the plot origin (*35*). The same phenomenon occurs when juvenile zircon precipitates onto a pre-existing core. Because zircon is stable, resistant to weathering, and has very slow diffusion, it is not uncommon for zircon grains to go through a magmatic system without being fully dissolved. In these cases, the U/Pb radioisotopic clocks are not completely reset, the ages will be older than the most recent crystallization event, and the two U/Pb ages will not be concordant.

Although the half-life of ^{235}U (704 Ma) is shorter than that of ^{238}U (4.47 Ga), ^{235}U is much less abundant (0.72%) than ^{238}U (99.27%), and as a consequence less ^{207}Pb is produced over a given unit of time than ^{206}Pb. For samples younger 1.2 Ga, the ^{206}Pb/^{238}U system will be more precise than the ^{207}Pb/^{235}U system. Older samples had more ^{235}U available to incorporate and a longer time for decay to happen, and for very old samples (>1.2 Ga), the ratio of ^{207}Pb/^{206}Pb can be used to determine the age of the sample with higher precision than ^{206}Pb/^{238}U.

By measuring both ^{206}Pb/^{238}U and ^{40}Ar/^{39}Ar ages from a sample, the consistency of the two methods can be tested. If both methods produce similar results, the age of the sample is well known. If the results do not match, then something more complicated may be happening: zircon crystals may have inherited cores, zircon crystals may be recording a pre-eruptive crystallization age (*36*), reheating events may have allowed some or all of the argon to diffuse out of the crystals, or alteration has allowed argon to diffuse out of the crystal more readily.

An NSF-funded project, EARTHTIME, is underway to address some of the challenges within the geochronology field: understanding and reconciling the discrepancies between the ^{206}Pb/^{238}U and ^{40}Ar/^{39}Ar systems, and reducing the inter-laboratory age discrepancies. To that end, three synthetic U/Pb age intercomparison standards have been prepared (100 Ma, 500 Ma, and 2 Ga) (*37*), and two new tracers (ET-535, a ^{205}Pb-^{233}U-^{235}U tracer, and ET-2535, a ^{202}Pb-^{205}Pb-^{233}U-^{235}U tracer) were mixed and calibrated (Condon *et al.*, in review; McLean *et al.*, in review), although they have not yet been sent to the Berkeley Geochronology Center.

References

1. A. D. Barnosky *et al.*, *Nature* **486**, 52–58 (June 2012).
2. H. Baadsgaard, J. F. Lerbekmo, *Canadian Journal of Earth Sciences* **20**, 1282–1290 (1983).
3. S.-C. Chang, PhD thesis, University of California, Berkeley, 2008.
4. M. A. Fracasso, A. Kolker, *West Texas Geological Society Bulletin* **24**, 5–10 (1985).
5. P. W. Signor, J. H. Lipps, *Geological Society of America Special Papers* **190**, 291–296 (1982).

6. D. H. Erwin, *The great Paleozoic crisis: life and death in the Permian* (Columbia University Press, 1993).

7. D. Jablonski, in, ed. by D. K. Elliot (Wiley, 1986), chap. Causes and consequences of mass extinctions: a comparative approach, pp. 183–229.

8. T. Birkelund, E. Hakansson, *Geological Society of America Special Papers* **190**, 373–384 (1982).

9. J. H. Lipps, *Marine Micropaleontology* **29**, 65–66 (1997).

10. R. N. Ginsburg, *Marine Micropaleontology* **29**, 67–68 (1997).

11. J. Smit *et al.*, *Marine Micropaleontology* **29**, 69–72 (1997).

12. J. I. Canudo, *Marine Micropaleontology* **29**, 73–76 (1997).

13. B. A. Masters, *Marine Micropaleontology* **29**, 77–79 (1997).

14. R. K. Olsson, *Marine Micropaleontology* **29**, 80–84 (1997).

15. X. Orue-etxebarria, *Marine Micropaleontology* **29**, 85–88 (1997).

16. G. Keller, *Marine Micropaleontology* **29**, 89–93 (1997).

17. J. Smit, A. Nederbragt, *Marine Micropaleontology* **29**, 94–100 (1997).

18. R. N. Ginsburg, *Marine Micropaleontology* **29**, 101–103 (1997).

19. J. Ogg, in *The Geologic Time Scale*, ed. by F. M. Gradstein, J. G. Ogg, M. D. Schmitz, G. M. Ogg (Elsevier, Boston, 2012), pp. 85–113, DOI: http://dx.doi.org/10.1016/B978-0-444-59425-9.00005-6.

20. N. C. Arens, A. H. Jahren, *Geological Society of America Special Papers* **361**, 75–93 (2002).

21. S. D'Hondt, P. Donaghay, J. C. Zachos, D. Luttenberg, M. Lindinger, *Science* **282**, 276–279 (1998).

22. C. Korte, H. W. Kozur, *Journal of Asian Earth Sciences* **39**, 215–235 (2010).

23. M. Magaritz, W. T. Holser, in *Abhandlungen der Geologischen Bundesanstalt in Wien 45*, ed. by W. T. Holser, H.-P. Schönlaub (Abhandlungen der Geologischen Bunesanstalt, May 1991), chap. The Permian-Triassic of the Gartnerkofel-1 Core (Carnic Alps, Austria): Carbon and Oxygen Isotope Variation, pp. 149–163.

24. M. R. Saltzman, A. R. Sedlacek, *Geology* **41**, 399–402 (2013).

25. J. L. Payne *et al.*, *Proceedings of the National Academy of Sciences* **107**, 8543–8548 (2010).

26. J. L. Hinojosa *et al.*, *Geology* **40**, 743–746 (2012).

27. C. Merrihue, G. Turner, *Journal of Geophysical Research* **71**, 2852–2857 (1966).

28. P. R. Renne, R. Mundil, G. Balco, K. Min, K. R. Ludwig, *Geochimica et Cosmochimica Acta* **74**, 5349–5367 (2010).

29. P. R. Renne, G. Balco, K. R. Ludwig, R. Mundil, K. Min, *Geochimica et Cosmochimica Acta* **75**, 5097–5100 (2011).

30. K. F. Kuiper *et al.*, *Science* **320**, 500–504 (2008).

31. T. A. Rivera, M. Storey, C. Zeeden, F. J. Hilgen, K. Kuiper, *Earth and Planetary Science Letters* **311**, 420–426 (2011).

32. T. Westerhold, U. Röhl, J. Laskar, *Geochem. Geophys. Geosyst.* **13**, Q06015 (June 2012).

33. J.-F. Wotzlaw *et al.*, *Geology* **41**, 867–870 (2013).

34. D. Phillips, E. Matchan, *Geochimica et Cosmochimica Acta* **121**, 229–239 (2013).

35. G. W. Wetherill, *Geochimica et Cosmochimica Acta* **9**, 290–292 (1956).

36. J. I. Simon, P. R. Renne, R. Mundil, *Earth and Planetary Science Letters* **266**, 182–194 (2008).

37. D. J. Condon, *Guidelines for Interlaboratory Calibration Experiment*, Accessed Jan. 23, 2014 (May 2008; `http://www.earth-time.org/ICE_guidelines.pdf`).

Chapter 2

Methods

2.1 Sample Preparation and Handling

Separation

Whole rock samples of tuffs were crushed, then rinsed with water to remove clays. For samples where coal or highly carbonaceous material was present, the samples were treated with warm hydrogen peroxide (5–10%) to oxidize the organic matter. Samples were then separated magnetically. The non-magnetic fraction was subject to two separations with lithium metatungstate (LMT) solutions, one which separated at 2.8 g/cm^3 and one at 2.63 g/cm^3. Zircon was hand-picked from the densest fraction, and sanidine for Ar-Ar dating was contained in the 2.63–2.8 g/cm^3 fraction. Zircons from a representative sample are shown in Figure 2.1.

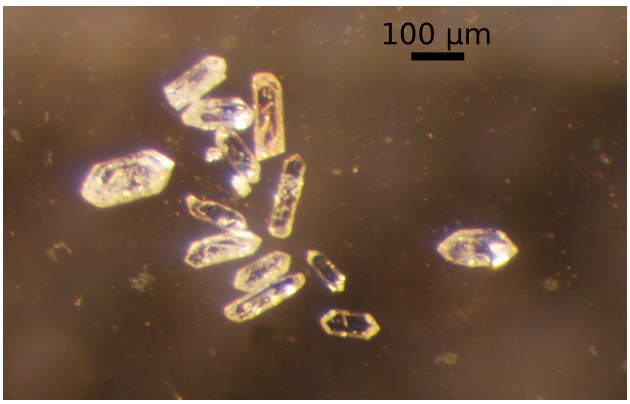

Figure 2.1: Microscope image of zircon separates from the tephra within the Bug Creek Null Coal (Section 3.2), of a generally representative size, shape, and clarity.

Annealing and Chemical Abrasion

Following the procedures of Mattinson (*1*), as demonstrated by Mundil *et al.* (*2*), the zircons were leached to remove any surfaces which may have been affected by preferrential loss of lead from the crystal.

After $\sim$ 50 zircons had been picked, they were photographed at high magnification and transferred to a quartz crucible. The zircons were annealed at 850 ℃ for 12 h. Following annealing, zircons were again photographed at high magnification, then transferred to Krogh-type teflon capsules. One drop of concentrated nitric acid and nine drops of concentrated HF were added to the capsule. The sealed capsules were then fitted into steel pressure sleeves and placed in an oven at 220 ℃ for 6–12 h. In general, 12 hours was more time than was necessary, and led to small samples being overly abraded. Abrasion times of 6–8 h are recommended for future work. Abrasion also is sensitive to the temperature, and even an extra 10 ℃ will cause over-abrasion; the teflon capsules also become difficult to remove from the steel sleeves.

Upon cooling, the samples were transferred to 2-mL screwtop teflon (Savillex) vials. As much of the supernant as possible was removed, and 8 drops of concentrated nitric acid and 20 drops of 8 *M* HCl were added to the vial. The vials were then sonicated for 10 minutes, rinsed three times with concentrated nitric acid, and finally stored in 1 mL of concentrated nitric acid.

Final Dissolution and Filament Loading

Supernatant was removed from chemically abraded zircons and replaced with 1 mL concentrated nitric acid. Zircons were then transferred individually to teflon capsules and photographed at high magnification with a microscope, and the supernatant again was removed. One drop ^{205}Pb–^{233}U–^{235}U (535) or ^{202}Pb–^{205}Pb–^{233}U–^{235}U (2535) spike was added to each capsule. Capsules were then placed onto a rack within a teflon liner containing 20 drops concentrated nitric acid and $\sim$5 mL concentrated HF. The liner was sealed in a Parr bomb and placed in an oven at 220 ℃ for 4–7 days to ensure complete dissolution.

Samples which were to be chemically separated were placed back in the Parr bomb with $\sim$5 mL 8 *M* HCl and heated at 170 ℃ for 12 hours.[1] After cooling, the capsules were dried to salts, then redissolved in 3 *M* HCl. Columns were run as described in the column chromatography section below. The Pb/U fraction was subsequently handled in the way as the unseparated zircon samples.

Samples were dried down to a microdroplet after the addition of two drops 3 *M* HCl and one drop 0.03 *M* phosphoric acid. Microdroplets were loaded onto outgassed, high-purity, zone-refined Re filaments with 3–4 μL colloidal silica gel solution prepared and cleaned as described by Schmitz (*3*) after Gerstenberger and Haase (*4*). The filaments were dried by

[1]Secondary dissolution with 8 *M* HCl at 170 ℃ appears to help remove reverse discordance, even in cases where no column chemistry is performed.

slow heating from 0.8 A filament current to a dull glow, around 2 A. A turret of up to 20 filaments was then placed in the mass spectrometer source.

Column Chromatography

Anion exchange resin (BioRad AG-X8, 200-400 mesh) was cleaned by alternating deionized water and 8 *M* HCl treatments. Each treatment involved swirling the resin in the reagent, using fresh reagent three times to make sure the acid concentrations were unaffected by residual liquid from a previous step. Columns and procedures are very similar to the those established by Krogh (*5*, *6*).

Teflon microcolumns, with a resin volume of ∼100 μL and a reservoir of 1 mL, were rinsed thoroughly with deionized water. Column reservoirs were filled much of the way with deionized water, then clean resin was added to fill the constricted volume and extend just into the reservoir. Once the resin was in the column, the reservoir and resin were washed by filling the reservoir with 8 *M* HCl, then deionized water, then 8 *M* HCl, and more 8 *M* HCl, before conditioning with 3 *M* HCl and adding the sample (itself in 3 *M* HCl). Rare Earth elements (REEs) were eluted with 100 μL 3 *M* HCl. Lead and uranium were eluted into a clean 2-mL teflon beaker with 200 μL 8 *M* HCl followed by 250 μL deionized water.

2.2 Mass Spectrometry

Mass spectrometry was performed with a Micromass (VG) Sector 54 thermal ionization magnetic sector mass spectrometer in peak-hopping mode using a Daly detector. The filament voltage was brought up to 8 kV, and the current was increased slowly until the sample was heated to 1300–1350 ℃. The Pb isotopes were measured at this temperature, then the filament was ramped up to 1400–1420 ℃ and U data was measured. Count rates at the beginning of measurement were around 200 kcps on spike isotopes, and typically dropped by a factor of 2–10 over the course of 30–60 minutes.

2.3 Data Reduction

Data was reduced either with *Isoplot* (*7*) or with *Tripoli* and *U-Pb Redux* (*8*, *9*), and include corrections for laboratory common Pb, spike Pb, mass fractionation, oxygen isotope interference for UO_2, and initial ^{230}Th disequilibrium. The data reported was handled with *Isoplot* when measuring only one synthetic Pb isotope, and *U-Pb Redux* when measuring two. Using *Tripoli* and *U-Pb Redux* required slightly different methods and outputs from the mass spectrometer. Data collected since April, 2013 are compatible with either data reduction scheme (though are more easily reduced with *U-Pb Redux*), while prior to that the formats were not compatible with *U-Pb Redux*. Using a *U-Pb Redux* compatible measurement routine and output format is recommended for future measurements.

Spike	$^{206}Pb/^{204}Pb$	$^{207}Pb/^{204}Pb$	$^{208}Pb/^{204}Pb$	$\frac{^{206}Pb}{^{204}Pb}/\frac{^{207}Pb}{^{204}Pb}$ corr.
BW ^{205}Pb-^{233}U-^{235}U	18.55 ± 0.63	15.50 ± 0.55	38.07 ± 1.56	0.9
BDS ^{202}Pb-^{205}Pb-^{233}U-^{235}U	18.32 ± 0.32	15.61 ± 0.28	37.92 ± 0.32	0.78

Table 2.1: Isotopic composition of blanks. All uncertainties here are 2σ of the population.

Decay constants used are those of Jaffey et al. (*10*), $\lambda_{^{238}U} = 1.55125 \times 10^{-10}\ y^{-1}$, and $\lambda_{^{235}U} = 9.8485 \times 10^{-10}\ y^{-1}$. Blank compositions are found in Table 2.1. For the ^{230}Th correction, a Th/U_{magma} value of 4 was used, as a typical Th/U ratio for silicic volcanic magmas.

2.4 Spike Calibration and Validation

BW spike

The BW spike is a ^{205}Pb-^{233}U-^{235}U spike mixed at the Berkeley Geochronology Center. Repeated analyses of R33 with this spike have yielded a mean age of 418.9 ± 0.4 Ma (n=9) (*11*). Analyses of the 100 Ma EARTHTIME solution yielded a mean age of 100.19 ± 0.07 Ma (n=7) and the 500 Ma EARTHTIME solution yielded a mean age of 499.97 ± 0.34 Ma (n=9) (*12*).

BDS spike

The BDS spike is a ^{202}Pb-^{205}Pb-^{233}U-^{235}U spike mixed at the Berkeley Geochronology Center. Replicate analyses of Temora 2 (collected by Black et al. (*11*)) zircon yielded a weighted mean of 417.69 ± 0.17 Ma (n=10, MSWD 1.2, 0 rejects, Figure 2.2), which is consistent with the age of 417.43 ± 0.06 Ma (n=11, MSWD=0.8) reported by Davydov et al. (*13*) using the EARTHTIME 535 tracer. The 100 Ma EARTHTIME solution yielded a mean age of 100.247 ± 0.040 Ma (n=7, MSWD 1.5, 0 rejects, Figure 2.3). Note, however, that the EARTHTIME reference solution is not necessarily 100.000 Ma (*14*).

Weighted Means and the MSWD

When combining dates from individual single-crystal analyses, an inverse-variance weighted mean is used to give greater weight to analyses with smaller uncertainties. However, a simple weighted mean of some arbitrary number of analyses may be misleading if there is significant scatter in the data outside uncertainties. To quantitatively assess the degree of scatter in the data, a measure called the mean square of weighted deviates (MSWD) is used (*15*). When the MSWD is >1, there is more scatter to the data than would be accounted for by the individual uncertainties, while if the MSWD is <1, the agreement between points is better than would be expected given the uncertainties on each point. Where there is significant

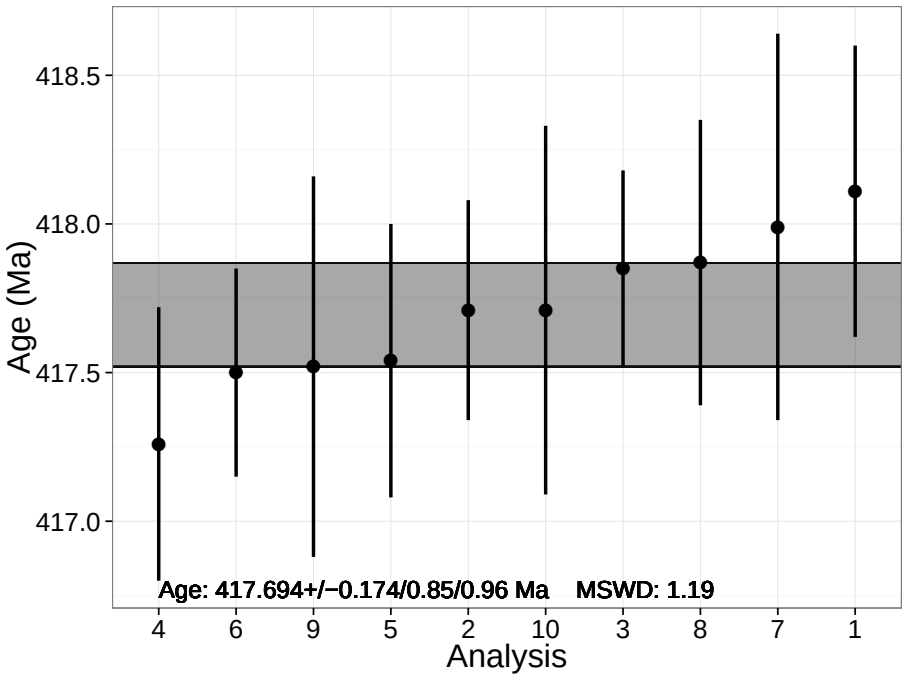

Figure 2.2: Temora 2 zircon measured with the BDS spike. Each single-grain analysis is a point accompanied by its uncertainty, and analyses are plotted in age rank from youngest to oldest. The grey bar corresponds to a 2σ interval around the weighted mean. Uncertainties of the form $\pm x/y/z$ represent the different sources of analytical and systematic uncertainty. Analytical uncertainty is stated as x, while y and z successively incorporate systematic uncertainties from the tracer (0.1%) and decay constant (0.054%).

indication of excess scatter, the uncertainties of the weighted mean are expanded by a factor of $\sqrt{\text{MSWD}}$ times the student's t parameter.

Plotting and Notation Conventions

When displaying weighted mean ages and individual age analyses, a standardized plotting format is used in this document. Each single-grain analysis is a point accompanied by its 2σ uncertainty, and analyses are plotted in age rank from youngest to oldest. Points in light red are excluded from the weighted mean calculation. The grey bar corresponds to a 2σ interval around the weighted mean.

Where uncertainties are expressed throughout this work, they are stated at the 2σ level unless otherwise specified. Uncertainties in decay constants are excluded unless stated otherwise.

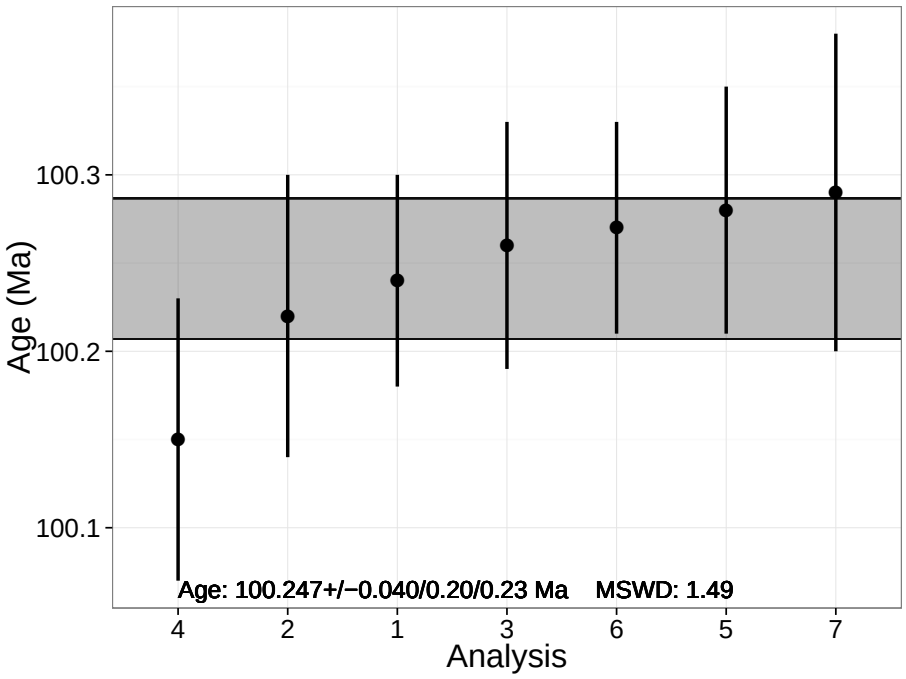

Figure 2.3: EARTHTIME 100 Ma solution measured with the BDS spike.

References

1. J. M. Mattinson, *Chemical Geology* **220**, 47–66 (2005).
2. R. Mundil, K. R. Ludwig, I. Metcalfe, P. R. Renne, *Science* **305**, 1760–1763 (2004).
3. M. D. Schmitz, *Silica Gel Preparation & Cleaning*, Isotope Geochemistry Laboratory, Boise State University (Feb. 2007; `http://earth.boisestate.edu/isotope/files/2010/07/Silica-gel-emitter.doc`).
4. H. Gerstenberger, G. Haase, *Chemical Geology* **136**, 309–312 (1997).
5. T. E. Krogh, *Geochimica et Cosmochimica Acta* **37**, 485–494 (1973).
6. M. D. Schmitz, *Column Chemistry Guidebook*, Isotope Geochemistry Laboratory, Boise State University (May 2009; `http://earth.boisestate.edu/isotope/files/2010/07/Column-Chemistry-Guidebook.doc`).
7. K. R. Ludwig, "Isoplot 3.75", Berkeley Geochronology Special Publication 5 (Berkeley Geochronology Center, 2012).
8. J. F. Bowring, N. M. McLean, S. A. Bowring, *Geochem. Geophys. Geosyst.* **12**, Q0AA19 (June 2011).

9. N. M. McLean, J. F. Bowring, S. A. Bowring, *Geochem. Geophys. Geosyst.* **12**, Q0AA18 (June 2011).

10. A. H. Jaffey, K. F. Flynn, L. E. Glendenin, W. C. Bentley, A. M. Essling, *Phys. Rev. C* **4**, 1889–1906 (5 Nov. 1971).

11. L. P. Black *et al.*, *Chemical Geology* **205**, 115–140 (2004).

12. R. B. Irmis, R. Mundil, J. W. Martz, W. G. Parker, *Earth and Planetary Science Letters* **309**, 258–267 (2011).

13. V. I. Davydov, J. L. Crowley, M. D. Schmitz, V. I. Poletaev, *Geochemistry, Geophysics, Geosystems* **11**, n/a–n/a (2010).

14. D. J. Condon, *Guidelines for Interlaboratory Calibration Experiment*, Accessed Jan. 23, 2014 (May 2008; `http://www.earth-time.org/ICE_guidelines.pdf`).

15. G. A. McIntyre, C. Brooks, W. Compston, A. Turek, *Journal of Geophysical Research* **71**, 5459–5468 (1966).

Chapter 3

High-Resolution U/Pb Geochronology Across the Cretaceous-Paleogene Boundary in the Hell Creek Region of Northeastern Montana

3.1 Introduction

As the most recent of the five major mass extinctions of the Phanerozoic, the Cretaceous-Paleogene (K-Pg) mass extinction is the one which can yield the highest temporal resolution. The Hell Creek region of northeastern Montana has been a hotbed for paleontological research over the past 40 years because of its highly fossiliferous terrestrial sediments (*1*). While the final throes of the extinction coincide with a bolide impact (*2*, *3*), there is still disagreement on whether other factors, such as volcanism in the Deccan Traps, contributed to the extinction (*4–9*), and indeed whether there was an extinction underway when the bolide struck has not yet been resolved (*10–12*).

One resolution, which combines multiple causes, is that temperature swings of ∼8 ℃ in the last 300 ka before the boundary (*13*, *14*)—possibly caused by Deccan Traps volcanism in what is now India—caused the ecosystems to become predisposed for catastrophe, and that the Chixulub impact was a *coup de grace* on an already fragile ecosystem (*2*). Such an interpretation acknowledges the synchrony of the impact to the major extinction pulse, but also provides a testable mechanism for pre-impact diversity loss observed in mainly in terrestrial vertebrates. With high-resolution geochronology from near the fossil localities (this work) and precise dating of the most voluminous phases of Deccan Traps volcanism (yet to be done), this hypothesis can be tested.

Over the past century, research in the Hell Creek region (including western North and South Dakota) has evolved from a search for museum-quality dinosaur fossils (*1*). Extensive mapping was undertaken (*15*), and as paleocene mammalian fauna were recognized in the

older collections—particularly at the Fort Peck Reservoir power plant—interest in vertebrate paleontology of the area greatly increased (*16*, *17*). Other vertebrates, such as crocodilians, champsosaurs, and turtles, as well as invertebrates and plants were recognized and collected (*13*, *17–19*). Despite the efforts of many field teams, one thing remained clear: the lateral continuity of any given stratum is poor over a scale of meters to a few kilometers, so lateral correlation of specimens is tenuous at best. Fossils found in channel deposits also may be reworked, so it is possible to have both older reworked fossils preserved alongside younger fossils (*20*).

Within the uppermost reaches of the Cretaceous Hell Creek Formation, and the lower portion of the overlying, mostly Paleogene Tullock Formation, a series of coal lenses are found, which have been canonically used to correlate stratigraphy in the Tullock formation (*20*). Many of these coal lenses include volcanic tephra, and because the airfall deposition of such volcanic ash would be synchronous throughout the region, these tephra can be used as stratigraphic marker beds. While it is possible for these volcanic tephra to be reworked and appear in an anomalously high (young) stratum, the tephra are assumed to be primary because the energy of the deposition environment required to form these lignites is very low.

Because the area is of such high paleontological value and because these tephra are present, the Hell Creek region has been the subject of numerous geochronological studies using U/Pb, $^{40}Ar/^{39}Ar$, and Rb/Sr techniques (*21–23*). The summarized results of Swisher *et al.* are shown in Figure 3.1, and have been updated to the decay constant and standard age of Renne *et al.* (*24*, *25*). However, there have been significant technological and methodological improvements since that time (*26*, *27*), particularly in the U-Pb system. Recent re-collection and analysis of several tephra dated by Swisher *et al.* (*23*) and Baadsgaard and Lerbekmo (*22*) yielded more precise ages (*2*). Of more than 40 distinct tephra which have been found, many have never been dated and many of those may be amenable to dating (Sprain *et al.*, in revision).

According to estimates based on modern deposition and compaction rates in Okefenokee Swamp and the likely mix of plants near the K-Pg boundary in southern Saskatchewan (roughly 200 km north of the Hell Creek region), each centimeter of coal records 80–320 years, so for the meter-thick lignite lenses found in the Hell Creek and Tullock Formations, each likely represents 8–32 ka (*28*, *29*). Consequently, even the most high-precision radioisotopic dating is unlikely to resolve the difference in age between tephra within a single lignite lens. Dating one tephra within a lignite, combined with the estimate of lignite deposition rate, should allow for good estimation of the age of any tephra within that lignite. If the tephra is geochemically unique, then if a tephra at another outcrop is found with that geochemical signature, the date can be applied to the new outcrop. In this way, a regional correlation can be built up, but without the need for high-precision dating of a tephra from every lignite at every site.

Defining the K-Pg boundary can be more difficult than it seems on its face. In the Hell Creek region, the iridium-bearing impact layer, where it is found, is very near the Hell Creek/Tullock formational boundary. However, there are areas in the region where Paleogene fauna and pollen are found below the formational contact—that is, based on lithology they

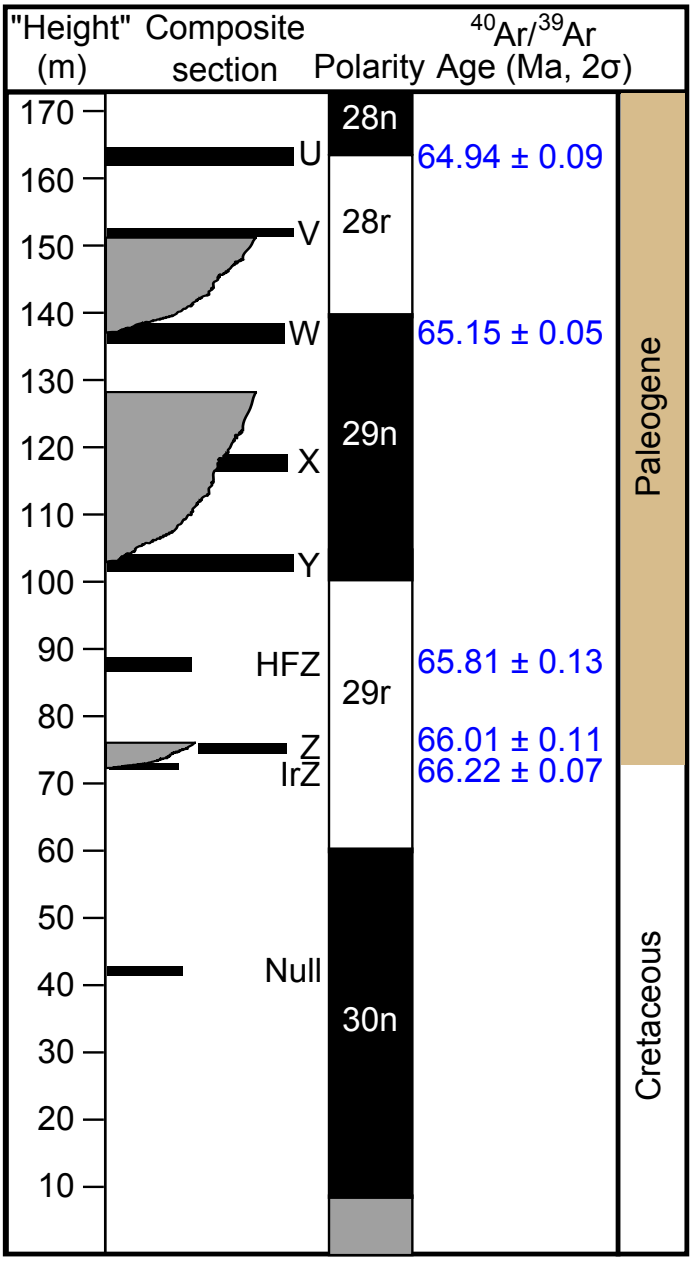

Figure 3.1: Composite section showing dates of Swisher *et al.* (*23*) updated per Renne *et al.*(*24*, *25*). Note that because this is a composite section and lateral continuity is not very good, the height is approximate, and the coals found in different outcrops may be separate lenses in about the same stratigraphic position.

would be considered latest Cretaceous (*17*). Yet using the impact horizon as the boundary definition is also unsatisfactory. Although the impact horizon is preserved in many places in the region, there are many sections where it is not preserved or recognizable. Just as any modern terrestrial environment would not be expected to preserve a single stratum over a 100×50 km area, so too we should not expect that from a region where few beds are preserved on length scales of more than a few km.

High-resolution geochronology in this area will not only shed light on the paleobiological changes taking place, but it offers an opportunity to calibrate the geomagnetic polarity timescale around this boundary (Sprain *et al.*, in revision). Geomagnetic polarity is often the highest-resolution chronometer which can be successfully applied to much of the Deccan Traps, although efforts are underway to obtain higher-precision radioisotopic dates. The geomagnetic polarity timescale can also be used to correlate changes seen in terrestrial and marine environments where high-precision geochronology is unavailable or unobtainable. Indeed, there has already been considerable effort in determining a paleomagnetic sequence throughout the Hell Creek Formation (*23*, *30*, *31*).

3.2 Sample Locations

The geology of the region consists primarily of flat-lying sandstones and siltstones, but includes several lignites (often called coals in the literature) of up to 1.5 m thickness. Two formations are found in this area, the *Hell Creek Formation* and the overlying *Tullock Formation* (sometimes the Tullock Member of the Fort Union Formation). These lignites were mapped and named by Collier and Knechtel (*15*); the lowest persistent lignite was given the designation *Z*, and overlying lignites were *Y*, *X*, *W*, etc.

However, as Collier and Knechtel note, "Bed Z... is probably not a single continuous bed but rather a succession of lenses of coal in about the same stratigraphic horizon." More recent work has established that indeed there seem to be several separate lenses at nearly the same horizon, and these different lenses are given variant names such as *HFZ* for the Hauso Flats Z-coal and *IrZ* for the iridium-bearing Z-coal (*23*). Like the Z coal, the Y coal also appears to be laterally discontinuous, but occurance of a lignite at a similar stratigraphic level is widespread. High-precision dating, geochemistry, and patterns of zircon inheritance can all be used to determine whether tephra within the "Y" coal are the same from outcrop to outcrop. Further details about the regional geology and sampling locations can be found in Sprain *et al.*, in revision. Figure 3.2 shows the approximate geographic location of samples used in this study.

On an outcrop scale, there can be several complicating factors present. Some outcrops have clear channels being cut through many of the strata, and others have faults which can hinder correlation based on elevation. Both of these phoenomena are present in the outcrop shown in Figure 3.3

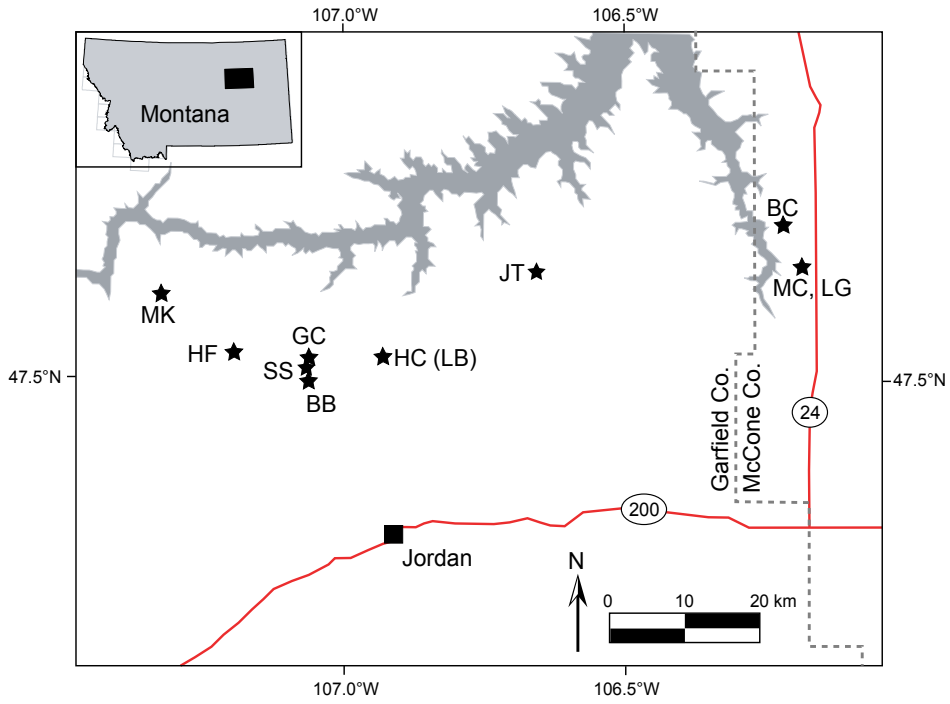

Figure 3.2: Sampling locations used in this study, modified from the map in Sprain *et al.* One locality, Hell Creek (HC), is referred to as Lerbekmo (LB) in Sprain *et al.* (in review) and LeCain *et al.* (*32*), and is shown here as both to reinforce that correspondence. BB: Biscuit Butte, BC: Bug Creek, GC: Garbani Channel, HC (LB): Hell Creek (Lerbekmo section), HF: Hauso Flats, JT: Jared's Trike, LG: Lofgren section [Section B of Lofgren (*20*)] (synonymous with MC), MC: McGuire Creek (synonymous with LG), MK: McKeever Ranch, SS: Saddle Section.

Hauso Flats

Hauso Flats iridium-Z (IrZ)

Near the base of the section at Hauso Flats is the IrZ coal, a lignite containing both an iridium-bearing impact layer and, 2 cm above the impact layer, a 1–3 mm thick volcanic tephra. The tephra was collected as HF-1PR (and in a subsequent year as HF11-1). Its location is 47° 31.593' N, 107° 12.462' W.

Hauso Flats Z (HFZ)

About 20 m above the IrZ coal is the Hauso Flats Z coal (HFZ), which contans one tephra (HF-3PR). The tephra containing visible crystals and glass shard pseudomorphs, is ∼1 cm thick, occuring ∼30 cm beneath the top of the lignite, and is located at 47° 31.504' N, 107° 11.992' W.

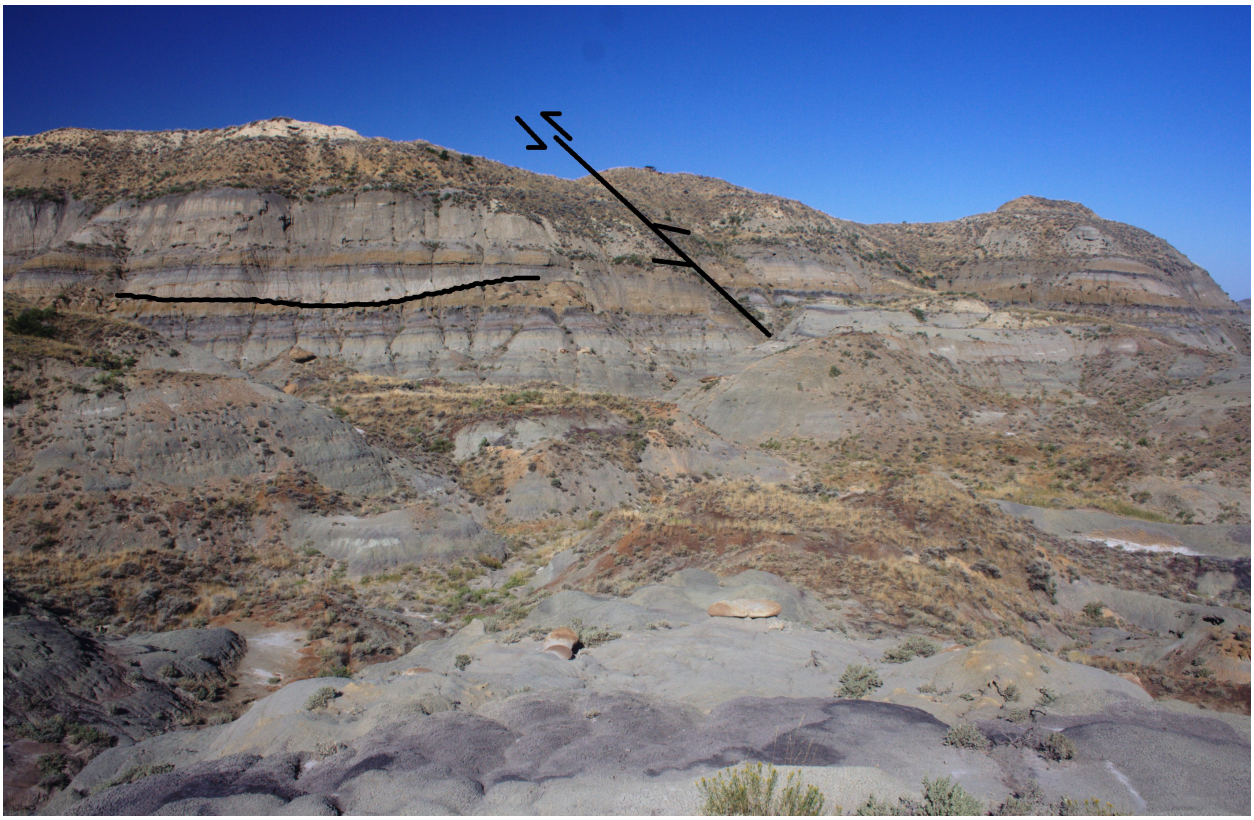

Figure 3.3: A representative outcrop, showing a channel and a fault, near the Jared's Trike site

Bug Creek

Null Coal

In the valley of Bug Creek, a 50-cm thick lignite appears near the top of the Hell Creek Formation, and underneath a point bar deposit capped by the Z coal. Below the top of the lignite 3 cm is one pinkish tephra, 1–2 cm thick (BC-1PR, and BC11-1). The outcrop is located at 47° 40.810' N, 106° 12.826' W.

Z Coal

Capping a point-bar deposit at Bug Creek is the Z coal. Two tephra were found in this lignite, a thin orangish tephra 0.5–2 cm thick, and 9 cm above it a beige-green tephra, 8–10 cm thick, with coarse sanidine and biotite, especially at the base. These tephra were sampled at 47° 40.875' N, 106° 11.734' W.

McKeever Ranch

At McKeever Ranch, a tephra was found within a lignite given a tentative designation of Y Coal (sample MK12-1), located at 47° 35.864' N, 107° 20.414' W. This tephra contains easily visible sanidine crystals.

Biscuit Butte

Within a small biscuit-shaped butte alongside the road, a thick (10–15 cm) tephra occurs within a roughly meter-thick lignite, mapped as the U coal. The tephra contains large crystals of sanidine, and is located at 47° 29.218' N, 107° 4.127' W.

Jared's Trike

Near the Jared's Triceratops locality of the Museum of the Rockies, a lignite is found in outcrop. Within the 1 m thick lignite are four tephra. The first (JT11-3) is found 15 cm beneath the top of the lignite, and is 5 cm thick. Beneath that tephra 10–15 cm, the second (JT11-2) is found, with a thickness of 4 cm. The next tephra is 1 cm thick and 15 cm beneath JT11-2, and was not sampled. Finally, 15 cm beneath the third tephra is a 4 cm-thick tephra (JT11-1), which is only 4 cm above the base of the lignite. These tephra were sampled at 47° 37.777' N, 106° 37.535' W, a little over a hundred meters to the south of the Jared's Triceratops locality. This lignite and the tephra in it are probably correlative with the Z coal at Bug Creek, at the Lerbekmo section, and at the Lofgren section (Sprain, pers. comm. 2014).

Garbani Channel

On the southwest slope of Garbani Hill, located at 47° 30.960' N, 107° 4.101' W, a richly fossiliferous channel fill deposit, the Garbani Channel, is exposed, cutting down from between the W and X Coals to the Y Coal. The site has been divided into numerous paleontological sublocalities, and includes many terrestrial mammal fossils. Here, the Y Coal is present as a doublet with a ∼50-cm thick lower lignite, a 1-meter shale, and a 1-meter thick upper lignite. Roughly 2 cm beneath the top of the lower Y Coal lignite, a 1–3 cm thick pink-grey tephra occurs, which contains abundant sanidine. This tephra was sampled as GC12-3. A date from this sample constrains the maximum age for the Garbani Channel deposit, and hence for the fossils within the Garbani Channel.

Saddle Section

At the Saddle Section, the W coal is found as a doublet of 1-m thick lignites. Each lignite contains 6–10 tephra, though almost all are 4 cm thick or less and variable in thickness over meter distances or less. Of these, the uppermost tephra of the upper W coal, a 1–2 cm thick

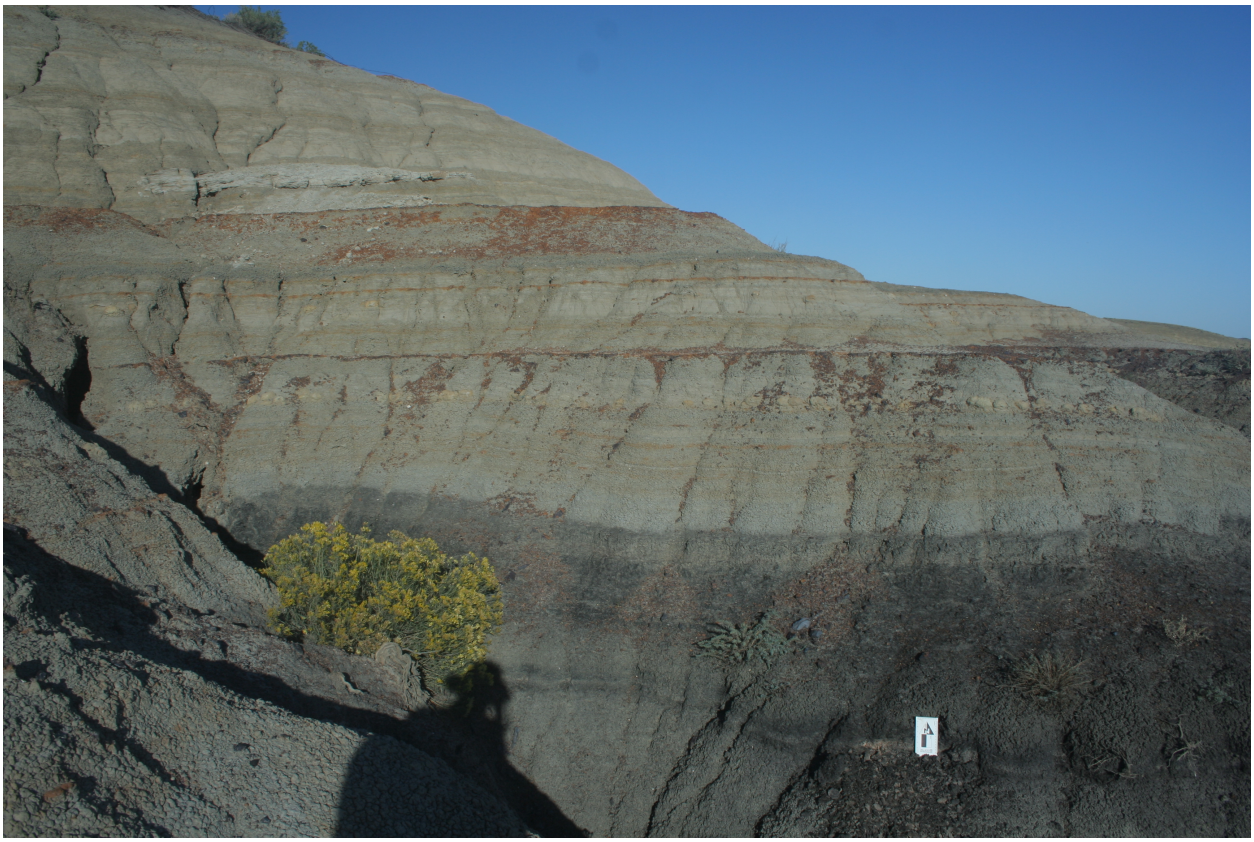

Figure 3.4: Photo of the LG11-1 Tephra at the Lofgren section, with a little excavation seen to the lower left of the card. Arrow height is 10 cm, and the black bar on the lower left of the arrow is 5 cm. The photo was taken looking generally east in the mid- or late-afternoon, and a circular polarizing filter was used. Photo by William S. Mitchell, III.

bed with coarse crystals (SS11-3) was collected. A second tephra from the upper W coal, 0.5–4 cm thick and 15 cm beneath the top of the lignite was collected (SS11-2). Finally, a tephra from near the bottom of the lower lignite was also collected (SS11-1).

Lofgren Section

Z Coal

Lofgren's Section B, transect Y includes two lignites, the lower of which is the McGuire Creek Z (MCZ) (*20*), located at 47° 37.792' N, 106° 10.207' W. This lignite contains several tephra. A 1–3 cm thick tephra was collected from about 5 cm above the base of the lignite (LG11-1, Figure 3.4). Additional tephra which are equally thick have ben found higher in the 0.5–1 m thick lignite (Sprain, pers. comm. 2014).

X Coal

Near the top of Lofgren's Section B, an additional tephra-bearing lignite is present, and is mapped as the X coal by Rigby and Rigby (*33*). One tephra from this lignite was collected and dated (MC11-3).

Lerbekmo Site

Along the road to the Hell Creek Marina, a small outcrop on the east side of the road contains a tephra-bearing lignite (47° 31.593' N, 106° 56.397' W). This outcrop has been well-studied through the years, and includes an iridium layer at the base of the lignite (*21–23*, *34*). Within the lignite, three tephra appear. The thickest, with large crystals, is in the center, with thinner tephra above and below. Samples of each of these tephra were collected, and the 1-cm thick tephra (HC-1PR) ∼25 cm beneath the prominent 5-cm thick tephra was used for $^{206}Pb/^{238}U$ dating. This tephra is extremely crystal rich. It grades into the lignite on both the upper and lower boundaries. Locally where it is thickest, the tephra is pink in color.

3.3 Sample Preparation Methods

Samples were prepared by soaking in water and decanting the fine clays. Where lignite was still present, hydrogen peroxide and gentle heating was used to remove it. Further separation was achieved by sieving, magnetic separation, and density separation. Zircons were hand-picked to select only the clearest, most euhedral, most pristine grains. Grains with visible cores were not picked.

Zircons were annealed, leached, and loaded onto filaments as described in Chapter 2. Optimal leaching conditions were determined—after a series of failures—to be around 6 h at 220 ℃.

For many samples, inheritance generally presented itself as Precambrian cores, so during the Pb analysis it was possible to use the $^{207}Pb/^{206}Pb$ age to determine if the analysis was likely to yield a juvenile age. In cases where the $^{207}Pb/^{206}Pb$ age was Precambrian, less Pb and U data was gathered.

3.4 Results

Inheritance was pervasive among almost every sample, even in clear, relatively euhedral zircons. Concordia plots (with insets showing the youngest zircons) for GC12-3, HC-1PR, HF-1PR, MC11-3, and SS11-1 are shown in Figures 3.5, 3.6, 3.7, 3.8, and 3.9 respectively. Several of the zircons in SS11-1 form a discordia line (*35*), shown in Figure 3.10. The exceptional samples where inheritance was not problematic are the McKeever Ranch Y Coal tephra (MK12-1), Bug Creek Z Coal thick tephra (BC-2PR), Hauso Flats HFZ Coal tephra

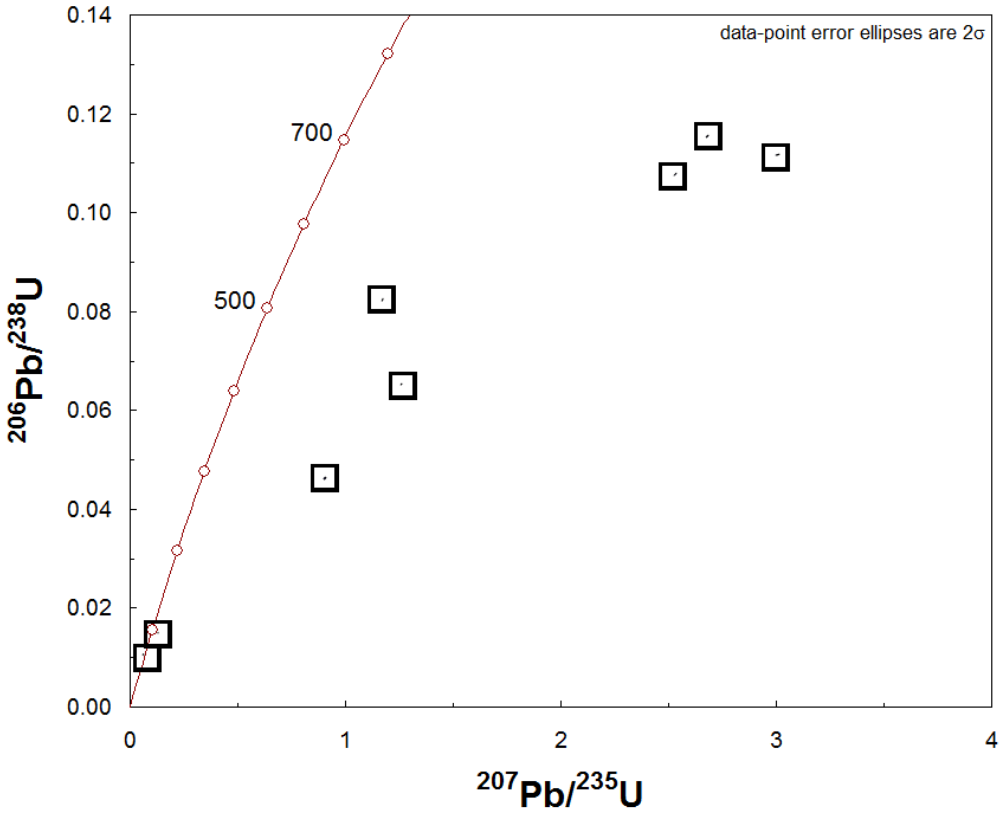

Figure 3.5: Concordia plot of a Garbani Channel Y Coal tephra (HC-1PR). Because the uncertainties on the points are small, they have been highlighted with boxes. The box in the lowest left (youngest) region of the plot contains the three analyses shown in the weighted mean plot (Figure 3.14).

(HF-3PR), and the Biscuit Butte U Coal (BB11-1). Several samples (HC-1PR, HF-1PR, GC12-3, LG11-1, SS11-1, and SS11-3) yielded only one or two analyses which could be considered juvenile, and thus these ages should not hold much weight.

Samples where two or more juvenile zircons (<68 Ma and in agreement with each other) were measured are presented in Figures 3.11–3.20. Other samples, especially the uppermost tephra in a probable Z Coal near Jared's Trike showed a complicated inheritance pattern, either from very small inherited cores, or from protracted (1–2 Ma) pre-eruptive crystallization or reworking. In such cases, the ages were cut from the high end but it is not clear that an objective, high-precision date can confidently be teased out.

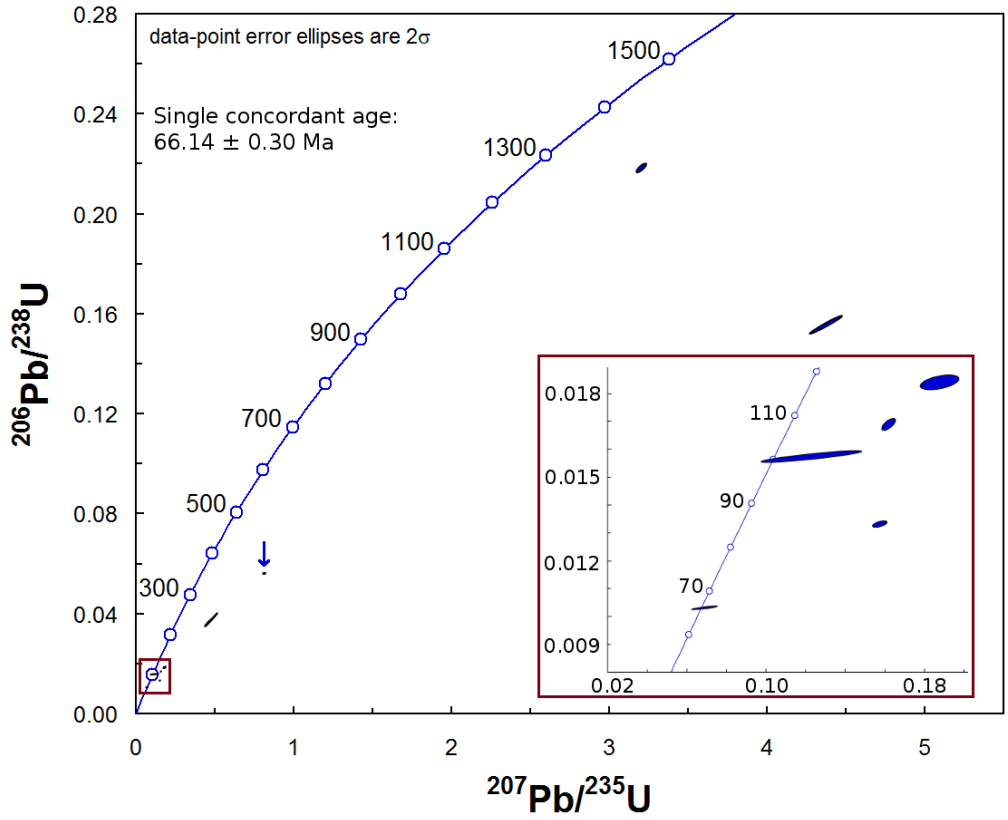

Figure 3.6: Concordia plot of the Lerbekmo Site Z Coal tephra (HC-1PR). Because the uncertainties on one of the points are small, it has been highlighted with an arrow. The lower left (youngest) region of the plot has been expanded in the inset.

3.5 Discussion

Although some sites and samples show primarily juvenile zircon, the majority of samples analyzed show clear and pervasive inheritance, even among the most pristine zircon grains. Strongly discordant analyses are interpreted to result from inherited Precambrian cores with Cretaceous/Paleogene rims. In more complicated samples, such as JT11-3 (Figure 3.16), the inheritance may be reflecting either a pre-eruptive residence time, or remobilization of zircons crystallized ~ 1 Ma before the eruptive event.

Compared to the age determinations for the Z coal by Baadsgaard and Lerbekmo (*22*), these results are much more precise and accurate, though that work represented the state-of-the-art when it was published. In their work, rather than running single zircon crystals, large loads of 80–90 mg zircon separates were used for each analysis. Such large multi-grain samples can be inaccurate if there is inheritance present. Because the lead and uranium are averaged over the entire sample, a few Precambrian zircons in with many

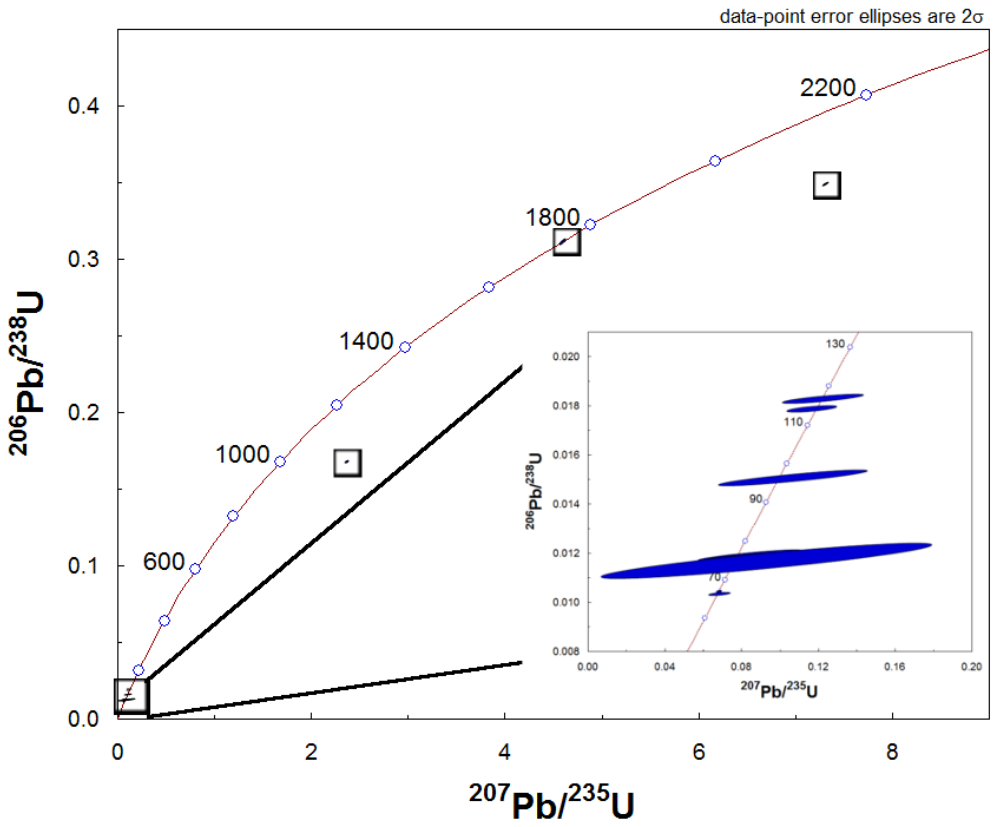

Figure 3.7: Concordia plot of the Hauso Flats IrZ Coal tephra (HF-1PR). Small points have been highlighted with boxes, and the youngest region (lower left) has been expanded in the inset.

Cretaceous-Paleogene zircons will yield data which are slightly discordant but largely reflect the Cretaceous-Paleogene age. By analyzing single grains, it is often possible to determine on a grain-by-grain basis whether the age is biased from inheritance.

Other factors leading to the improvement in precision and accuracy are the drastic reduction of lead backgrounds and the use of "chemical abrasion". Laboratory lead blanks in the Baadsgard and Lerbekmo work were 2.3 ng, over three orders of magnitude larger than the blanks for the results shown above. Reduced lead blanks allow the analysis of individual crystals, rather than the multi-grain samples used previously.

Chemical abrasion (*26*) has also improved the precision and accuracy of $^{206}Pb/^{238}U$ dating by leaching away the outer surfaces of the zircon crystals (*27*). Not only are the surfaces removed, but any water-accessible cracks or fractures will also have the surfaces dissolved, leaving the most pristine areas of the crystal intact. Without this treatment, the water-accessible areas are susceptible to lead loss, where lead is mobilized and removed by fluids more readily than uranium. Such lead-loss yields spurious ages, and because the effects are

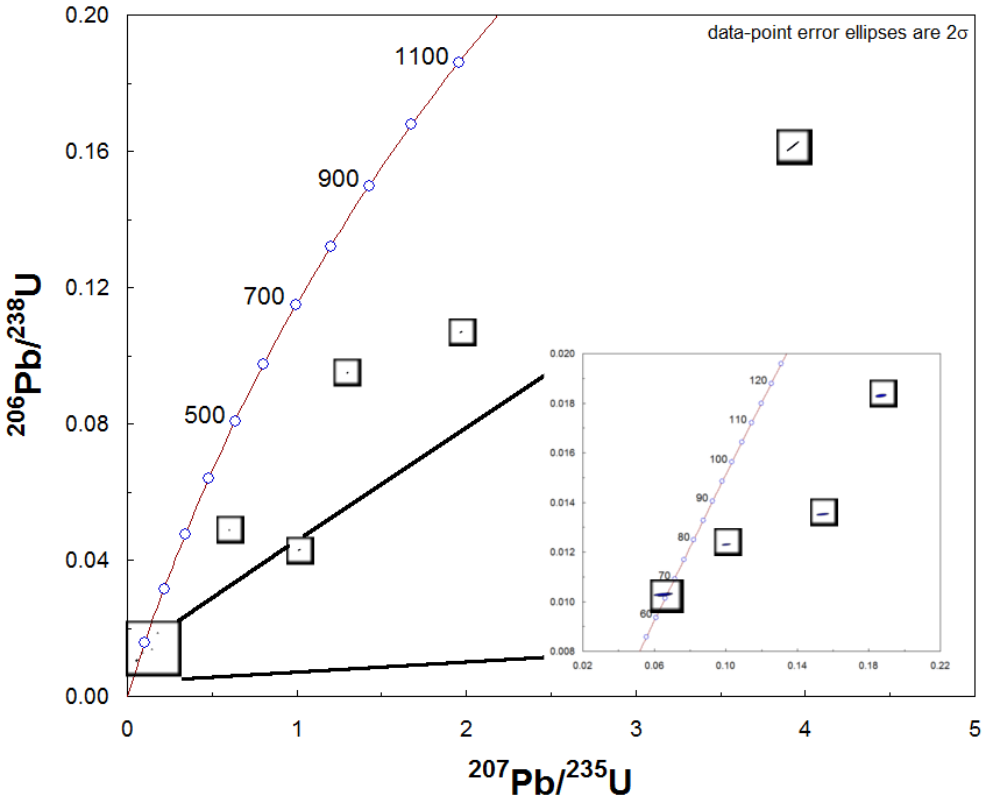

Figure 3.8: Concordia plot of the McGuire Creek X Coal tephra (MC11-3). Points have been highlighted with boxes, and the youngest region (lower left) has been expanded in the inset.

not uniform grain-to-grain, the dispersion of ages within a sample will be elevated(*27*).

Remarkably, given the level of inheritance of zircons within many of these samples, Baadsgaard and Lerbekmo (*22*) sampled one of the few units which *does not* suffer from pervasive inheritance. Despite being sampled at the same locality (Lerbekmo Site), the Baadsgaard and Lerbekmo results are from a different tephra within the same lignite as HC-1PR. While their results show coherent ages and a dominant mode of juvenile material, the results from HC-1PR show so much inheritance that multi-grain analyses would be utterly worthless. Choosing the right tephra can make a big difference, and often there is no way to tell which tephra is the right one until the mass spectrometry is underway.

Additional work on these tephra and many others is being carried out at the Berkeley Geochronology Center and the University of California, Berkeley, including $^{40}Ar/^{39}Ar$ dating, chemical characterization of feldspars and titanite with EPMA, and Pb isotopic characterization of feldspars. Some of this work has led to the suggestion that the tephra dated by Baadsgaard and Lerbekmo is laterally equivalent to the Bug Creek Z Coal tephra sampled

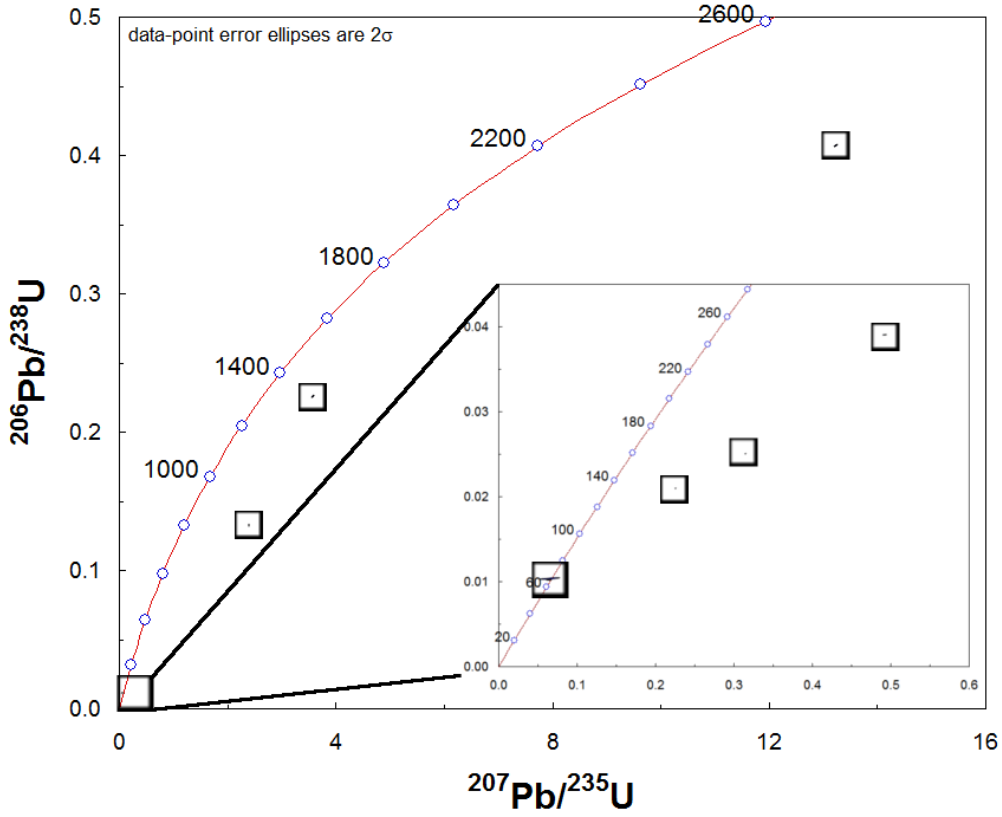

Figure 3.9: Concordia plot of the lower Saddle Section W Coal tephra (SS11-1). Points have been highlighted with boxes, and the youngest region (lower left) has been expanded in the inset.

here as BC-2PR (Sprain, pers. comm.). The pattern of inheritance—or rather the lack thereof—is consistent with this interpretation.

Using the approximate stratigraphic locations of the lignites, a chronology of the composite section similar to that of Figure 3.1 can be made using the new data (Figure 3.21). Stratigraphic height in that figure must be interpreted with caution, as it is a composite of many different sections, and the thicknesses of sections can vary significantly over the region. Additionally, the assignments of tephra to a specific coal designation may be incorrect. In one case, the X coal, the $^{206}Pb/^{238}U$ date appears to be much older than the $^{40}Ar/^{39}Ar$ date, which is in contrast to the other tephra. It is very likely that the age assigned here to the X coal is significantly older than the eruption age.

Paleomagnetic studies are also underway to use the high-resolution geochronology in this region to calibrate the geomagnetic polarity timescale. The results of this U-Pb dating work and these other projects are already facilitating exciting new paleontological work in the region as the timescales over which events happened becomes clearer.

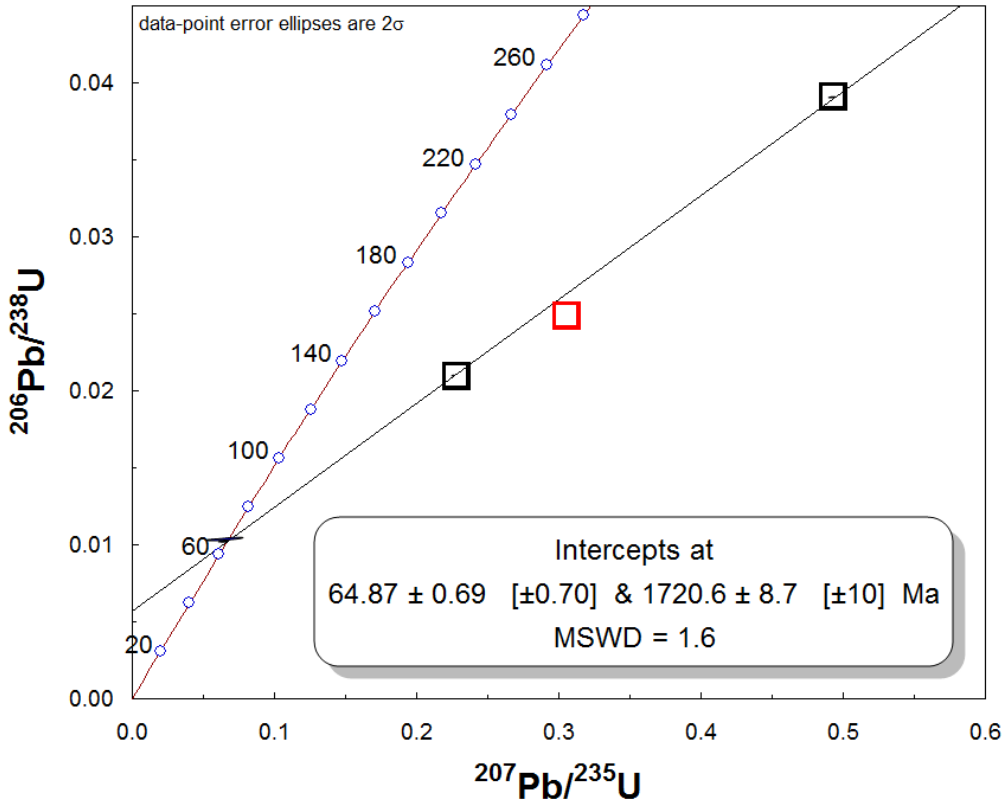

Figure 3.10: Discordia plot of the lower Saddle Section W Coal tephra (SS11-1), showing the region in the inset of Figure 3.9. Points have been highlighted with boxes. The red point has been excluded from the discordia line, as have the points which fell outside the inset. Uncertainties in brackets include decay constant uncertainties, but no tracer uncertainties are included in either stated uncertainty. Unlike the interpretation of Wetherill (*35*) where the upper age intercept corresponds to the crystallization age and the lower age intercept represents a time when lead was lost, here the interpretation is that a core crystallized at the upper age intercept and a younger rim crystallized around that core at the time indicated by the lower intercept.

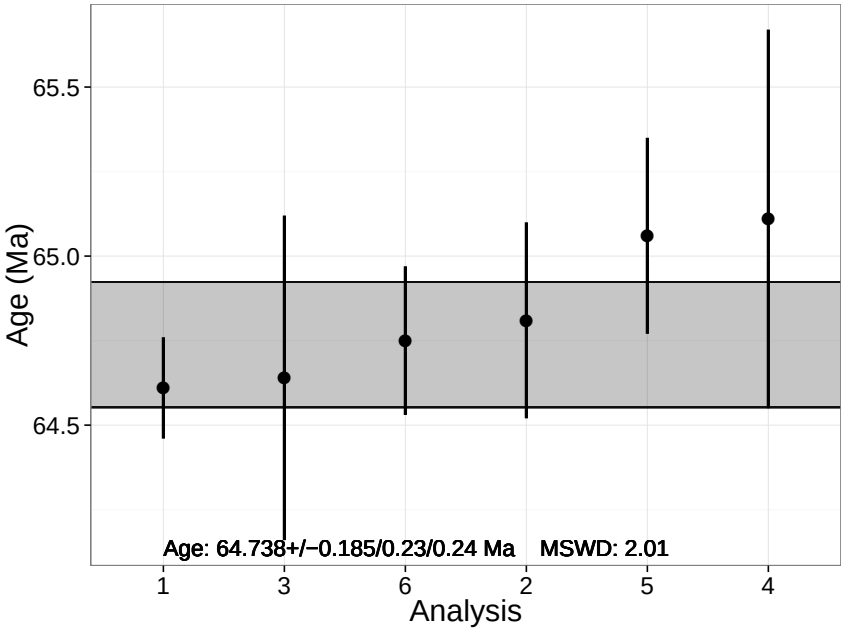

Figure 3.11: Biscuit Butte U Coal Ages

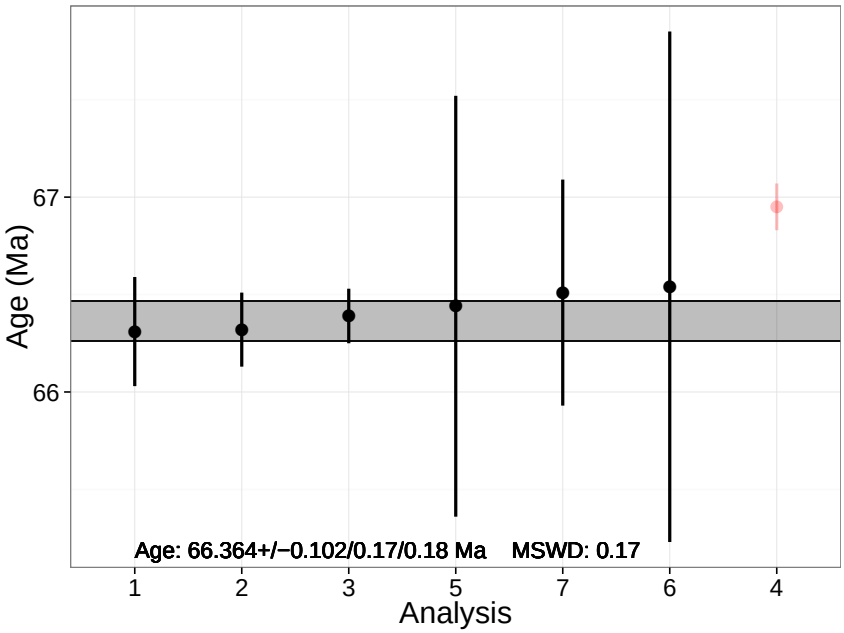

Figure 3.12: Bug Creek Null Coal Ages

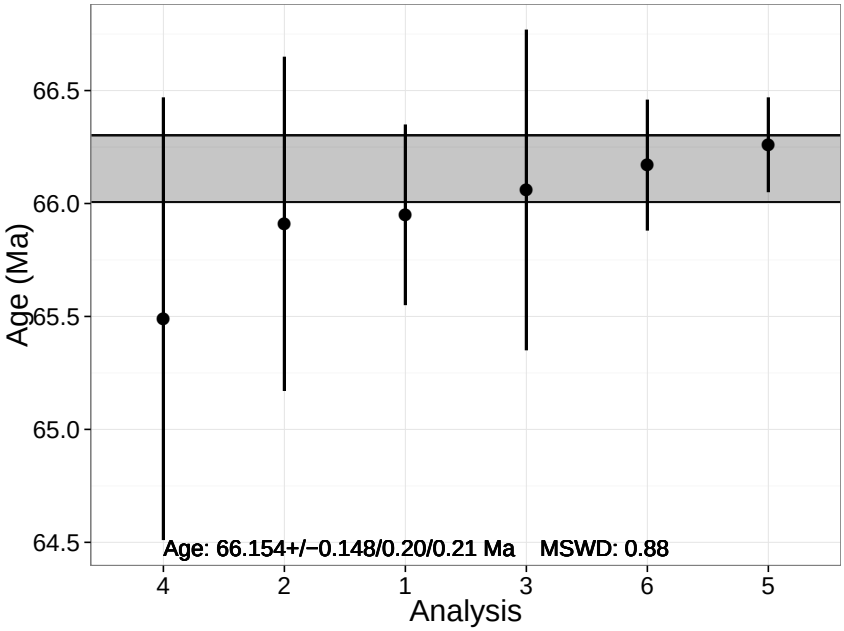

Figure 3.13: Bug Creek Z Coal Ages

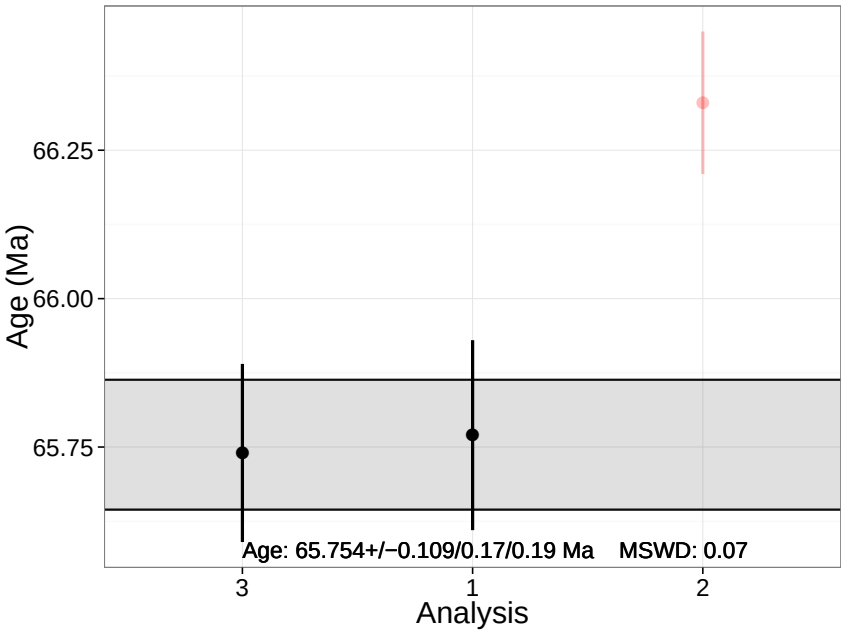

Figure 3.14: Garbani Channel Y Coal Ages

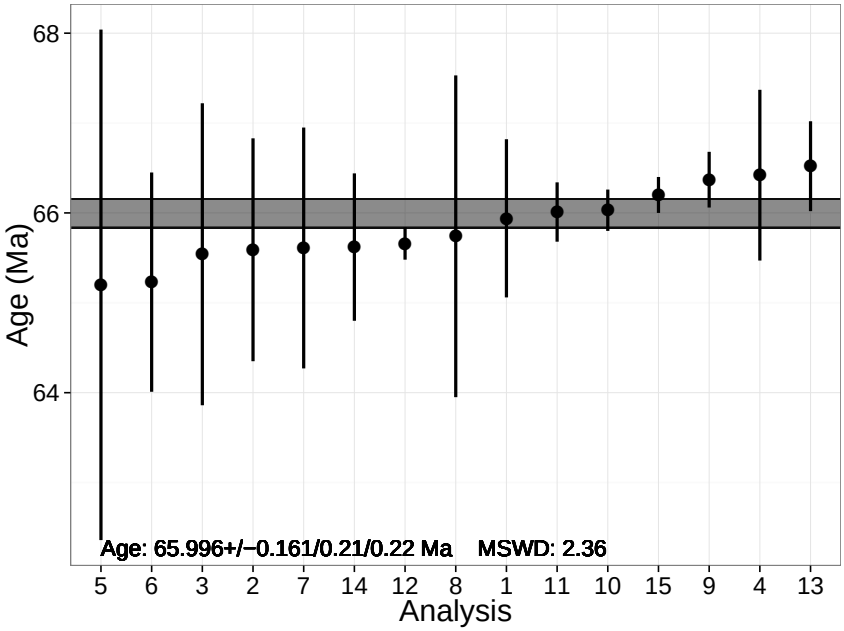

Figure 3.15: Hauso Flats HFZ Coal Ages

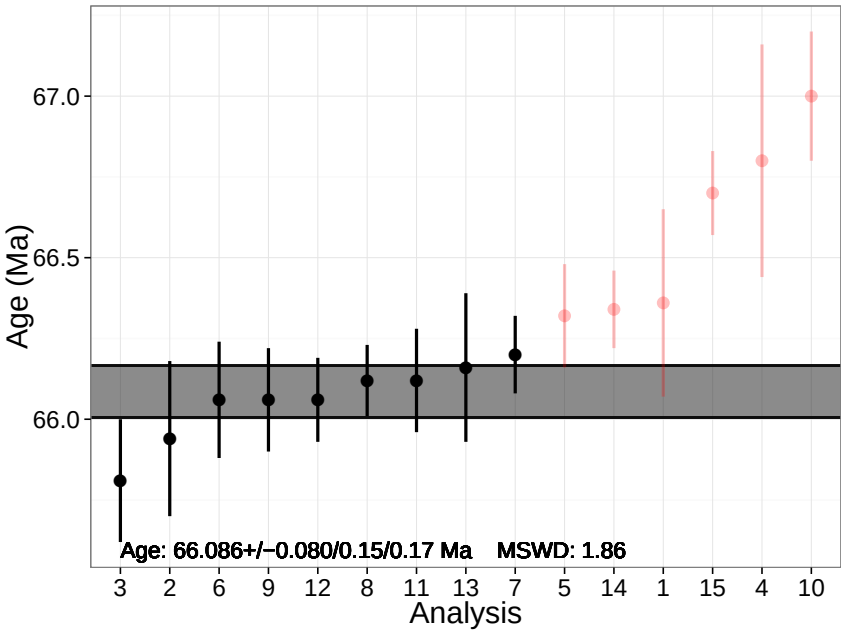

Figure 3.16: Jared's Trike Z Coal Ages

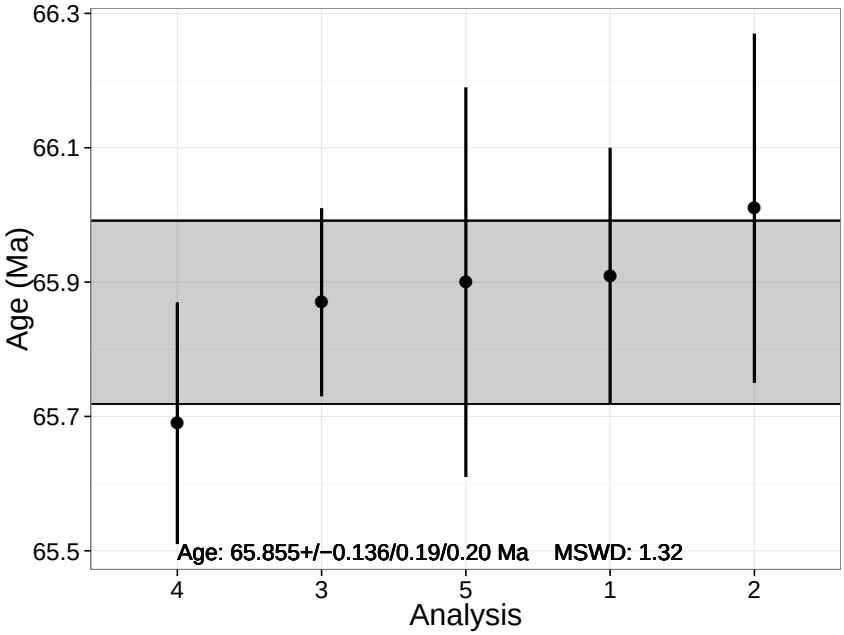

Figure 3.17: McGuire Creek X Coal Ages

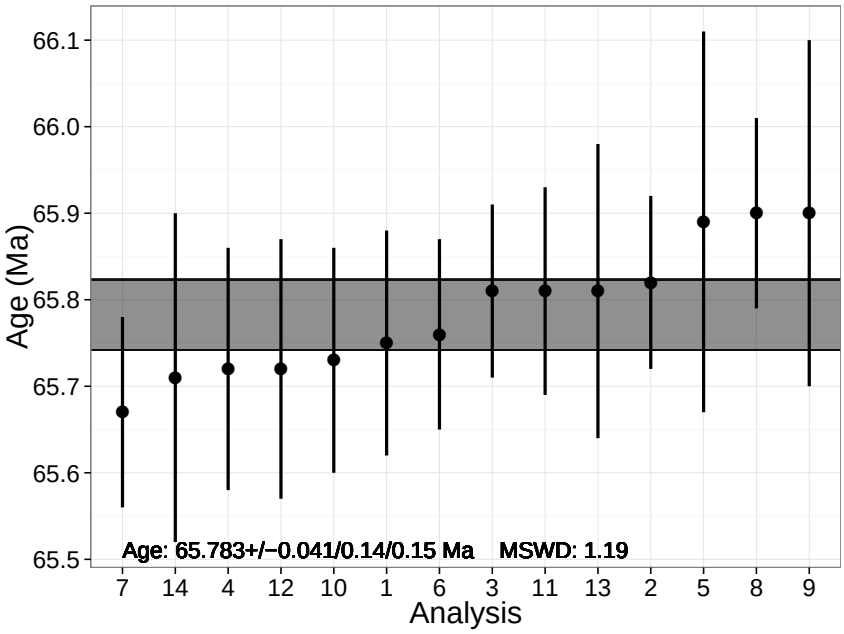

Figure 3.18: McKeever Ranch Y Coal Ages

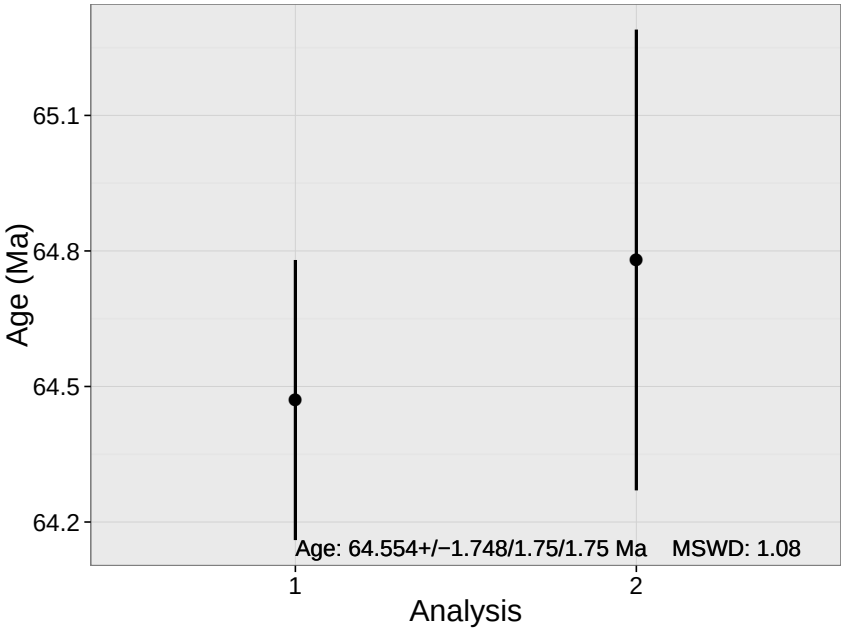

Figure 3.19: Saddle Section Upper W Coal Ages

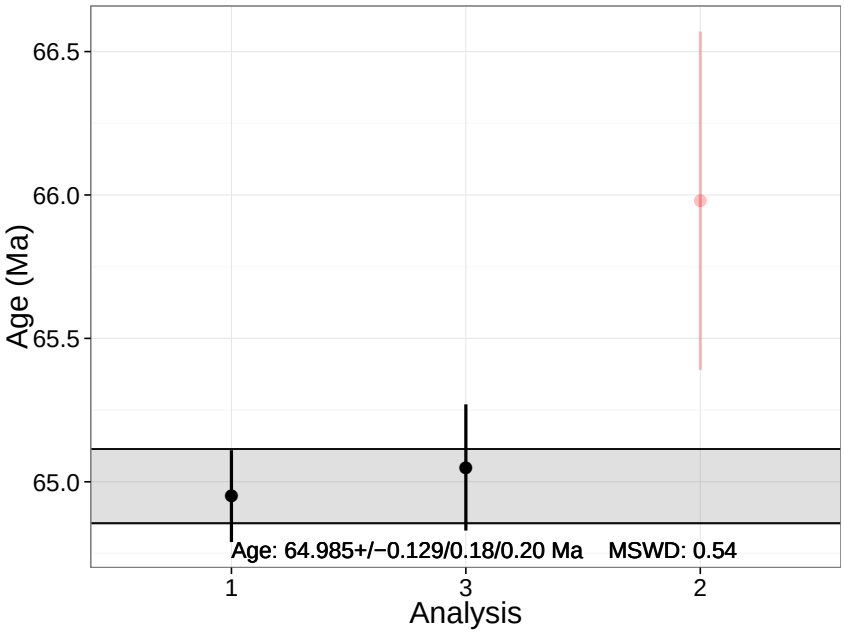

Figure 3.20: Saddle Section Lower W Coal Ages

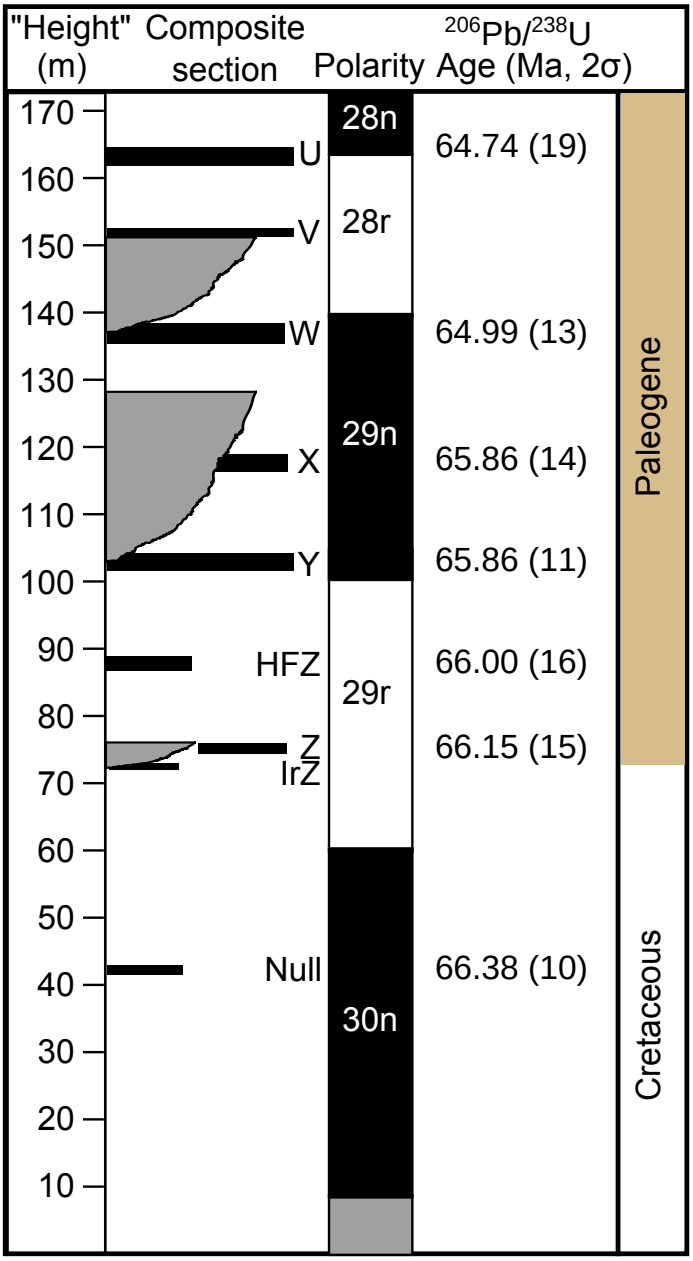

Figure 3.21: Composite section showing the new $^{206}Pb/^{238}U$ dates. Note that the date for the X coal (MC11-3) is based on two zircon crystals, and that those dates are ∼300 ka older than the sanidine $^{40}Ar/^{39}Ar$ date for the same tephra. The lateral variations in strata thickness can be quite large, so this composite section may not be suitable for determining a typical sediment accumulation rate for the region.

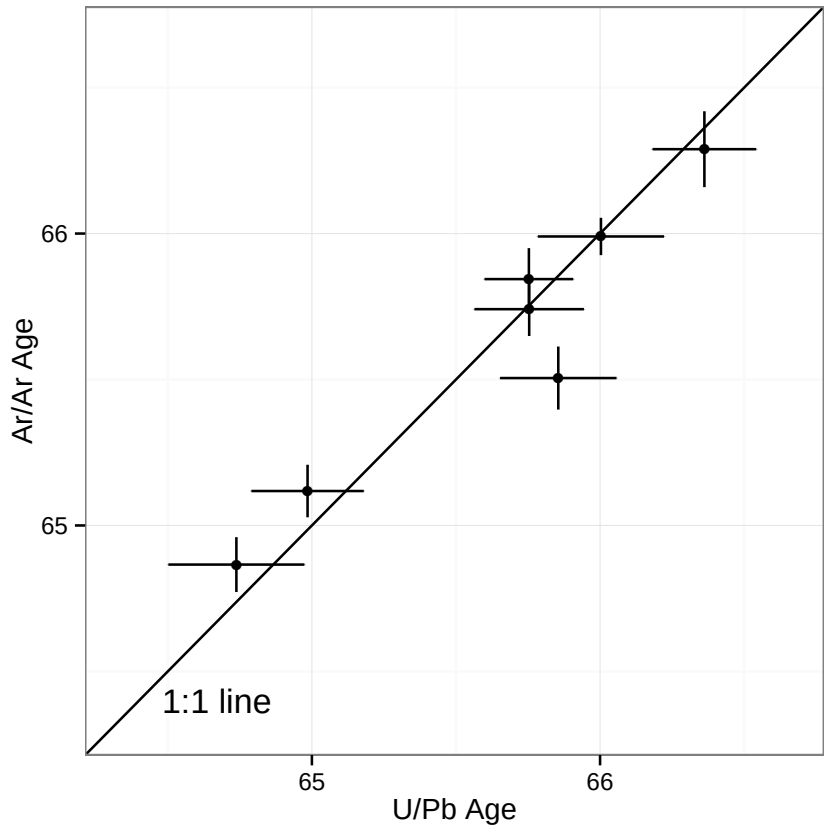

Figure 3.22: Comparison of $^{206}Pb/^{238}U$ and $^{40}Ar/^{39}Ar$ ages, each shown with 2σ uncertainties including tracer and decay constant uncertainties. The line is the 1:1 line, where the two systems agree on the age. In general points falling below and to the right of the line are not unexpected, as those points show either a pre-eruptive residence time or subtle effects of inheritance (*36*).

3.6 Conclusion

The results reported here are the first U-Pb zircon dates for this important paleontological region since the debelopment of the chemical abrasion technique in 2004, and represent a great improvement in precision and accuracy compared to Baadsgaard and Lerbekmo (*22*). Where juvenile zircons are present, the data are consistent with an age for the K-Pg Boundary of 66.043 ± 0.022 Ma as determined by $^{40}Ar/^{39}Ar$ dating (*2*), and are clearly inconsistent with a boundary age of 65.0 Ma as presented by Swisher *et al.* (*23*). They are also in very good agreement with the $^{40}Ar/^{39}Ar$ dates of Sprain *et al.* (in revision) (see Figure 3.22).

With these U-Pb dates for a number of tephra in the Hell Creek Region, the foundation has been laid for a thorough geochoronological framework for the region. This framework

could then be used to refine the geomagnetic polarity timescale for this interval. Ultimately that refined timescale could help address whether the Deccan Traps volcanism (in present-day India) was synchronous with the extinction event, or whether the two events occurred at distinctly different times.

3.7 Acknowledgments

Paul Renne, Roland Mundil, Alan Deino, Courtney Sprain, Jessica Banaszak, Andrew Tholt, and Denver Fowler provided assistance in the field. Abed Jaouni, Andrew Tholt, and Jessica Banaszak prepared samples. William Clemens, Walter Alvarez, Steve Self, Mark Richards, Seth Finnegan, Ryan Ickert, Sean Mulcahy, Paul Renne, Roland Mundil, Courtney Sprain, Jessica Banaszak, Andrew Tholt, Dori Contreras, and Ashley Poust participated in helpful discussions and related work.

References

1. W. A. Clemens, J. H. Hartman, *Geological Society of America Special Papers* **503**, 1–87 (2014).
2. P. R. Renne *et al.*, *Science* **339**, 684–687 (2013).
3. L. W. Alvarez, W. Alvarez, F. Asaro, H. V. Michel, *Science* **208**, 1095–1108 (1980).
4. A.-L. Chenet, F. Fluteau, V. Courtillot, M. Gérard, K. V. Subbarao, *Journal of Geophysical Research: Solid Earth* **113**, n/a–n/a (2008).
5. P. Schulte *et al.*, *Science* **327**, 1214–1218 (2010).
6. J. D. Archibald *et al.*, *Science* **328**, 973 (2010).
7. G. Keller *et al.*, *Science* **328**, 974–975 (2010).
8. V. Courtillot, F. Fluteau, *Science* **328**, 973–974 (2010).
9. P. Schulte *et al.*, *Science* **328**, 975–976 (2010).
10. J. Smit, A. Nederbragt, *Marine Micropaleontology* **29**, 94–100 (1997).
11. G. Keller, *Marine Micropaleontology* **29**, 89–93 (1997).
12. R. N. Ginsburg, *Marine Micropaleontology* **29**, 101–103 (1997).
13. P. Wilf, K. R. Johnson, B. T. Huber, *Proceedings of the National Academy of Sciences* **100**, 599–604 (2003).
14. T. S. Tobin, G. P. Wilson, J. M. Eiler, J. H. Hartman, *Geology* **NA**, NA (2014).
15. A. J. Collier, M. M. Knechtel, *USGS Bulletin* **905**, 1–77 (1939).
16. R. E. Sloan, L. Van Valen, *Science* **148**, 220–227 (1965).

17. W. A. Clemens, *Geological Society of America Special Papers* **361**, 217–245 (2002).

18. J. H. Hartman, J. I. Kirkland, *Geological Society of America Special Papers* **361**, 271–296 (2002).

19. N. C. Arens, S. E. Allen, *Geological Society of America Special Papers* **503**, 173–207 (2014).

20. D. L. Lofgren, *The Bug Creek Problem and the Cretaceous-Tertiary Transition at McGuire Creek, Montana* (UC Press, 1995).

21. H. Baadsgaard, J. F. Lerbekmo, *Canadian Journal of Earth Sciences* **17**, 671–673 (1980).

22. H. Baadsgaard, J. F. Lerbekmo, *Canadian Journal of Earth Sciences* **20**, 1282–1290 (1983).

23. C. C. Swisher III, L. Dingus, R. F. Butler, *Canadian Journal of Earth Sciences* **30**, 1981–1996 (1993).

24. P. R. Renne, R. Mundil, G. Balco, K. Min, K. R. Ludwig, *Geochimica et Cosmochimica Acta* **74**, 5349–5367 (2010).

25. P. R. Renne, G. Balco, K. R. Ludwig, R. Mundil, K. Min, *Geochimica et Cosmochimica Acta* **75**, 5097–5100 (2011).

26. J. M. Mattinson, *Chemical Geology* **220**, 47–66 (2005).

27. R. Mundil, K. R. Ludwig, I. Metcalfe, P. R. Renne, *Science* **305**, 1760–1763 (2004).

28. E. E. McIver, *Canadian Journal of Earth Sciences* **36**, 775–789 (1999).

29. K. Chin, D. Pearson, A. A. Ekdale, *PLoS ONE* **8**, e70920 (Aug. 2013).

30. J. D. Archibald, R. F. Butler, E. H. Lindsay, W. A. Clemens, L. Dingus, *Geology* **10**, 153–159 (1982).

31. J. F. Hicks, K. R. Johnson, J. D. Obradovich, L. Tauxe, D. Clark, *Geological Society of America Special Papers* **361**, 35–55 (2002).

32. R. LeCain, W. C. Clyde, G. P. Wilson, J. Riedel, *Geological Society of America Special Papers* **503**, 137–147 (2014).

33. J. K. Rigby, J. K. Rigby Jr., *Brigham Young University, Geology Studies* **36**, 69–134 (1990).

34. H. Baadsgaard, J. F. Lerbekmo, I. McDougall, *Canadian Journal of Earth Sciences* **25**, 1088–1097 (1988).

35. G. W. Wetherill, *Geochimica et Cosmochimica Acta* **9**, 290–292 (1956).

36. J. I. Simon, P. R. Renne, R. Mundil, *Earth and Planetary Science Letters* **266**, 182–194 (2008).

Chapter 4

Locating the Permo-Triassic Boundary in the Texas Panhandle Using U-Pb Geochronology

4.1 Introduction

Over the past 540 million years (Ma), there have been five major mass extinctions. Of those, the largest is the Permian-Triassic (P-T) extinction event, occurring at 251.941±0.037 Ma as determined by U-Pb CA-TIMS of zircon (*1*). At that time, 90% of species went extinct (*2*). Much of what we know of this extinction comes from the marine record within the Paleo-Tethys ocean (present-day localities ranging from Iran east to China).

The boundary between the Permian and Triassic is defined as the first appearance of the conodont *Hindeodus parvus*, specifically in the type section at Meishan, China(*3*). However, much less is know about what was happening on land at that time; terrestrial sections are less well preserved, often do not have the near-continuous deposition of the marine sections, and lack the microfossils which provide convenient high-resolution biochronology.

In order to understand what happened at the boundary, to piece together a picture of what mechanism or mechanisms caused the extinction, and to determine what reaction the biosphere had to the changes, it is important that we use evidence not only from the marine realm, but also from terrestrial sources. The rarity of terrestrial P-T sections and P-T sections distal to the Paleo-Tethys ocean make such sections interesting and worthy of detailed study. Additionally, to develop an understanding of events at the boundary, sections from these distant sites need to be correlated in space, in time, and across biomes (*4*).

One issue which complicates discussion of the events surrounding this boundary is the definition of the boundary itself. There are two important events, which are asynchronous: the first is the "mass extinction event", above which many species are never again seen, and the second is the defining feature of the boundary, the first appearance of the conodont *Hindeodus parvus* (*3*).

As the resolution used to study this extinction event and boundary becomes finer and finer, these definitions will become increasingly problematic. For the mass extinction event, there is a fundamental minimum duration for the extinction to happen, possibly as short as days in the case of a catastrophic event (e.g. an impact), but it could be happening over a much longer timescale, up to around 700 ka (*5*). The duration of this extinction depends on the specific kill mechanism, the timescale over which it operates, and the ecological resilience. While the shortest extinction timescales (days to thousands of years) are probably beyond possible resolution, the longer end of the range is larger than the uncertainty on radioisotopic dates from this time period. Treating the extinction as instantaneous in that case would be erroneous. Another problem with the extinction events comes from the Signor-Lipps effect (*6*). In brief, the Signor-Lipps effect states that neither the first nor last occurrence of a particular taxon will be preserved in the fossil record. The effect of this observation is that even if several species go extinct simultaneously, because of their infrequent preservation in the fossil record the extinction will appear more gradual than it truly is. Whatever beginning is chosen for the extinction horizon, the Signor-Lipps effect would suggest it is placed too low.

Defining the boundary with the first appearance is also problematic: the first fossil appearance will necessarily come later than the true first appearance. Additionally, the choice of any taxon for a biostratigrapic reference will not suit all needs, because no taxon would be evenly distributed between marine and terrestrial sections, and even less likely would be simultaneous first appearances in differing biomes in vastly different parts of the paleo-world. While the use of *H. parvus* is fine for many marine sections, that a conodont would be preserved in a terrestrial section is, although possible, so unlikely as to safely be deemed never occurring—at which point some other means of knowing the P-T boundary is needed for sections where *H. parvus* would not be found.

Many Permo-Triassic boundary sections, especially marine sections, display a significant shift in carbon isotopic compositions (*3*, *7*–*9*), which indicate changes in the carbon cycle. Additionally, shifts have also been oserved in the oxygen isotopic record, which suggests changes in temperature or the hydrologic cycle (*7*). Sampling within any given section, however, gives only an understanding of the isotopic changes at that location. For an isotopic excursion to be global, it needs to be found in many different sections from areas which were quite distant 252 million years ago. Sediments in modern-day Texas were on the western margin of Pangea 252 million years ago, far from the marine records of the Tethys ocean and the shallow marine and terrestrial basins of what is now Central Europe. Finding an isotopic signature in these sediments—or not finding one—would allow hypotheses of global carbon cycle and hydrologic cycle changes to be evaluated.

In the Palo Duro basin of the Texas Panhandle, sediments of roughly P-T age from sabkha and deltaic environments are present. Although there are not enough fossils of the right types to allow biostratigraphic ages to be determined, there are a few microfossils which have been found at Caprock Canyons State Park (*10*). These fossils are phytoliths (plant-stones), silicic buildups that form in the vascular structure of woody plants. At Caprock Canyons, the phytoliths are from conifers—if the age truly is of earliest Triassic, the western

margin of Pangea may have been a refuge for conifers at this time.

Previous work in this area by Fracasso and Kolker (*11*), found a volcanic tephra from the Quartermaster Formation in Caprock Canyons State Park to be 251±4 Ma, and identified—but did not date—a second tephra bed higher in the section at Caprock Canyons. However, the K-Ar method of dating which they used is less precise than modern dating techniques, specifically $^{40}Ar/^{39}Ar$ and zircon U-Pb dating. With no effective means of assessing whether there has been argon lost to alteration or reheating, these dates may be inaccurate as well as imprecise. Along with the magnetostratigraphy and scant fossil evidence, these K-Ar dates led Lucas and Anderson to assign a latest-Permian age for the Quartermaster Formation (*12*). Chang revisited this area and obtained sanidine and biotite $^{40}Ar/^{39}Ar$ dates and some non-chemical-abrasion zircon U-Pb dates (*13*). The $^{40}Ar/^{39}Ar$ dates of Chang have been recalculated according to the revised ^{40}K decay constant and Fish Canyon Sanidine standard age of Renne *et al.* (*14*, *15*).

Because there are extremely few fossils in this section and dating with the geomagnetic polarity timescale is non-unique without high-precision dating somewhere in the section, dating these strata with today's high-precision techniques will yield critical insight into the age of deposition relative to the Permo-Triassic boundary. At least two previous studies, those of Steiner (*16*) and of Chang (*13*), have studied the geomagnetic polarity at sections in this area.

Paleomagnetism can be an important tool here in several respects. First, the polarity (normal or reverse) will be a distinctive feature of a tephra—one in a normal polarity zone will not correlate to a tephra in a reverse zone in another section. Additionally, from the type section at Meishan, China, the boundary is known to occur in a normal polarity zone, around 200 ka after the reversal. These two facts allow for tephra to be distinguished from each other even if their isotopically determined ages are overlapping, and further constrain the placement of the Permo-Triassic boundary within the stratigraphic section.

Because volcanic tephra are deposited at the same time over a wide area, they can be used as marker beds for stratigraphic and geomagnetic correlation, provided that the tephra can be distinctly identified. Volcanic glass gives an excellent representation of the chemical composition of the magma during an eruption, but in these samples all of that glass has been altered. However, earlier work in this area by Chang identified several locations where tephra are found in outcrop, and analyzed biotite major element composition with electron probe microanalysis (EPMA) to test for correlation (*13*). Because biotite can have a wide range of compositions, with major elements such as Fe and Mg differing by several weight percent or more between samples, it is useful for establishing correlation (or, more easily, non-correlation). Building on the work of Chang, biotite from two additional tephra were analyzed: one along Highway 207, and one near Clarendon.

In a few cases, zircon trace element chemistry (primarily Hf, U, Th, and Ce) was also studied with EPMA. As in the case of major elements in biotite, the trace element composition in zircon would be expected to have a fairly narrow range if the zircon crystallized at a similar time from a chemically similar magma. Separate magma sources, however, would not be expected *a priori* to have the same trace element composition, and once again the

chemical differences can be used to demonstrate non-correlation.

Without reliable high-resolution biostratigraphy, and given the coarse nature of the geomagnetic polarity time scale, the primary tool for determining where the P-T boundary occurs within these sections is geochronology. Once ages have been determined for the tephra layers in our section, they must be compared to the date of the extinction at the Meishan, China type section, or at the Shangsi, China para-stratotype section. Because this extinction and boundary interval is an important event in Earth history, there have been many attempts to date the boundary in the type section, both with Ar/Ar (*17*, *18*) and U-Pb (*19*, *20*)

To address these questions, samples were collected from volcanic tephra within these sequences, and were dated using zircon U-Pb geochronology. The results of these experiments are presented below, along with a discussion of how these results fit within the stratigraphic context.

Geologic Setting

There are three major sedimentary packages in this study: the Whitehorse Formation (also Alibates Formation in subsurface; equivalent to the Rustler Formation of western Texas and southeast New Mexico), the Quartermaster Formation above it (Dewey Lake Formation in subsurface), and the Dockum Group (Chinle in New Mexico), which unconformably overlies the Quartermaster Formation. The Whitehorse Formation is gypsiferous red sandstones and mudstones, and would have formed in a tidal or supratidal environment. The Quartermaster Formation lacks the gypsum, and is predominantly red mudstones and sandstones deposited in an intratidal or supratidal environment, such as a subaqueous delta. Finally, the Dockum Group sediments are grey-brown sandstones. For more on the sedimentary units, see Tabor *et al.* (in prep).

Within the Whitehorse Formation, some of the gypsum veins can be seen cross-cutting the bedding, which indicates that those veinsare a secondary feature. It is unclear when—and over what period—this secondary featue developed, but this underscores the importance of paleomagnetic data and radioisotopic dating to determine accurate positions within the stratigraphy.

4.2 Sample Locations

Lithostratigrahy and Magnetostratigraphy

Samples were collected from five areas of the Texas Panhandle, in the southern United States (Figure 4.1). Results from lithostratigraphic (Tabor *et al.*, in prep.) and magnetostratigraphic (Collins *et al.*, in prep.; Chang (*13*); Steiner (*16*)) studies from these locations are summarized in Figure 4.2.

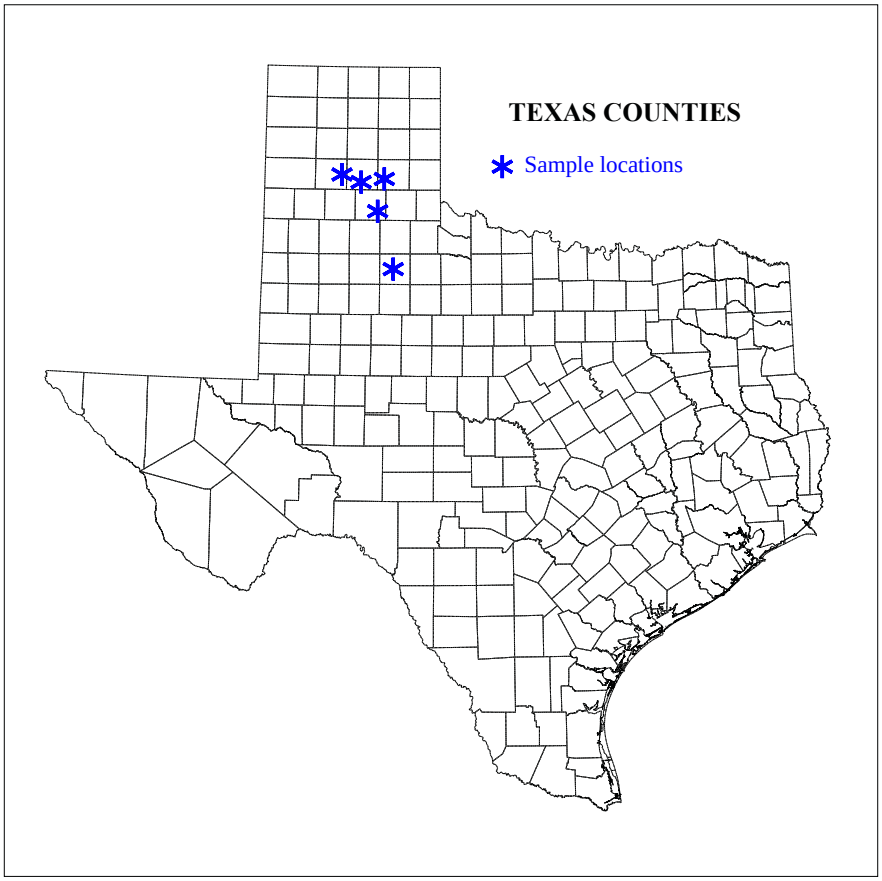

Figure 4.1: Sample locations from the Texas panhandle, southern US. The samples are, left to right across the top then down the right side, Palo Duro, Highway 207, Clarendon, Caprock Canyons, and Dickens. Basemap is from the Texas Parks and Wildlife Department GIS Lab.

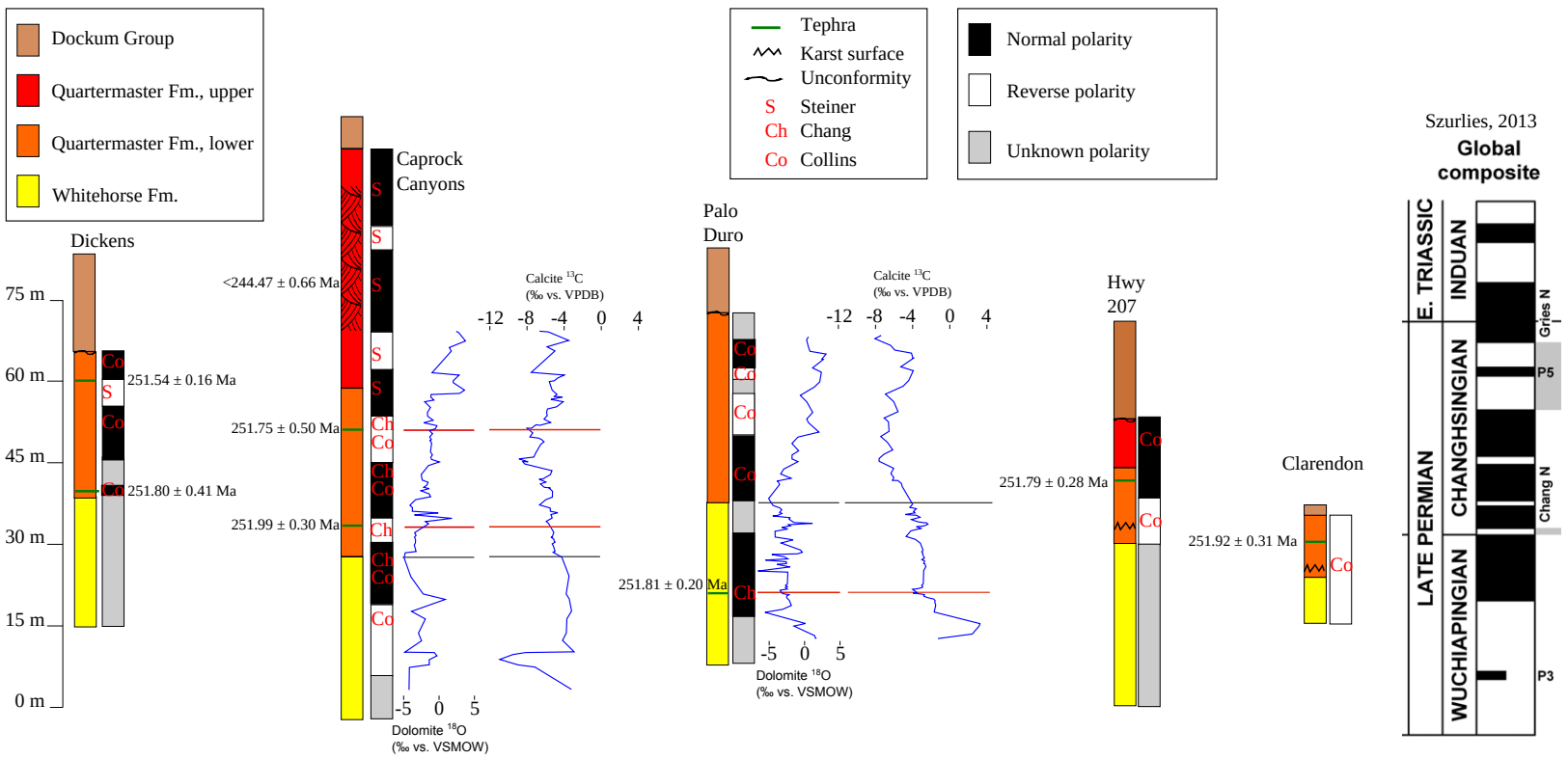

Figure 4.2: Lithostratigraphy and magnetostratigraphy of the sections. Lithostratigraphy is after Tabor *et al.*, and the magnetostratigraphy is a synthesis of data from Chang (*13*), Steiner (*16*), and Collins *et al.* (in prep). The global composite paleomagnetic column for the P-T boundary is from Szurlies (*21*).

Caprock Canyons

Two tephra, informally referred to here as Caprock Lower and Caprock Upper, were collected at Caprock Canyons State Park, TX. Steep canyon walls necessitated collecting the two tephra in slightly different locations (see Figure 4.3). The lower tephra was collected near the South Prong parking lot (34° 26.318' N, 101° 5.611' W), and the upper was collected on an exposure about one kilometer to the northeast (34° 26.926' N, 101° 5.044' W) and laterally correlated from traceable beds.

The lower tephra occurs about two meters above the Whitehorse-Quartermaster contact, is 4-8 cm thick and appears pink to purple. It is quite friable, and has abundant biotite. Fracasso and Kolker's description of the location and appearance of their lower ash bed is very consistent with what was sampled here, and we conclude that they sampled the same bed (*11*). This unit was sampled as OCH11-1, and comes from the same tephra at the same outcrop as these samples from previous work: CR97-4 and CRC07-2 (*13*).

The upper tephra occurs about a meter below the massive cliff-forming sandstones, is ∼1 cm thick, and is dark red to purple. This unit was sampled as OCH11-3, and is synonymous with these sample names from previous work: CR97-3, CRC07-1 (*13*).

Within the red-orange sandstone from the cross-bedded upper reaches of the Quartermaster Formation (34° 27.200' N, 101° 6.878' W), fossilized wood was found—a rare find in this formation. A sample of the sandstone near the fossilized wood was collected (OCH12-13) with the intent of finding a maximum age of deposition. While the zircons found in this cross-bedded sandstone are clearly not primary volcanic zircons, some may be freshly eroded from a young igneous rock, and must have been deposited some time after crystallization. Further, because the cross-bedding implies active surface processes (wind or streams), it is quite possible for significant gaps in deposition to occur within these units. At the very least, the cross-bedded sandstone is likely to have a vastly different (and fluctuating) sediment accumulation rate compared with the flat-lying beds lower in the section. Having a good idea of the deposition date will inform the conclusions paleontologists make by studying the fossils found at this outcrop.

Dickens

Along US Highway 82 just east of Dickens, TX, there is a roadcut which contains a redbed sequence very similar to the one found at Caprock Canyons, including the Whitehorse-Quartermaster contact, and fairly high into the Quartermaster Formation.

One tephra (OCH12-3) occurs as a 6–10 cm thick white bed immediately under a resistant 30-cm thick red bed (see Figure 4.4). The tephra has abundant biotite, and has tentatively been correlated to the upper tephra at Caprock Canyons (*13*). A sample was collected at 33° 37.504' N, 100° 48.970' W, and this unit is synonymous with DK07-1 of Chang (*13*).

On the basis of the stratigraphic similarity to Caprock Canyons, a lower tephra was predicted to occur within this section, corresponding to the lower tephra at Caprock. Although along the road this portion of the section is covered, permission was obtained to collect

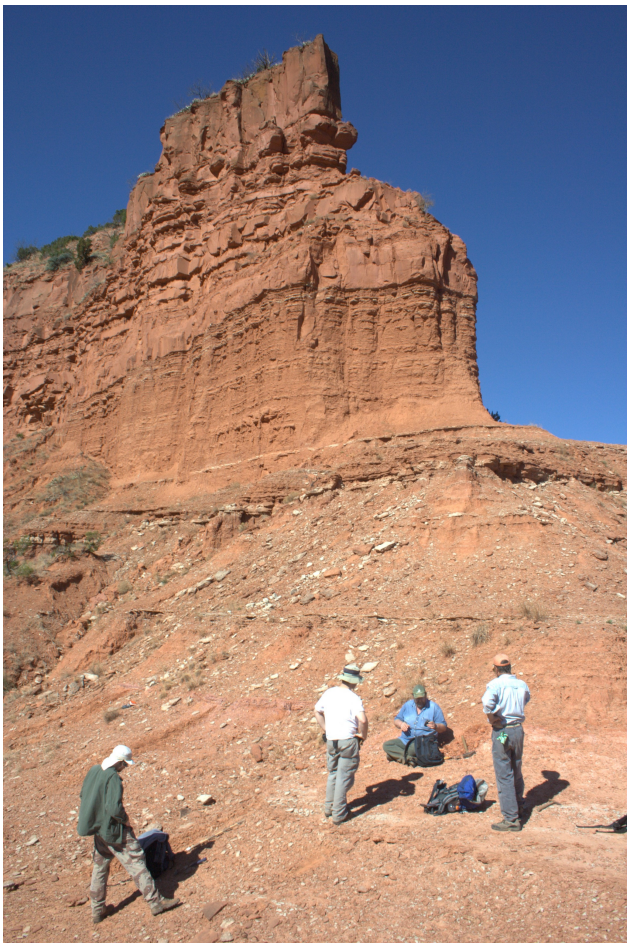

Figure 4.3: Outcrop at Caprock Canyons State Park where the Caprock Lower tephra was sampled. Only the Quartermaster Formation is visible. Photo by William S. Mitchell, III.

from private land (33° 37.419' N, 100° 48.779' W). In the expected position, a discontinuous "layer"—manifested as blebs of a pink-to-purple color—was found which contained significant biotite. This "layer" occurred within a red-orange mudstone. However, collection of a fist-sized amount of the pink and purple material yielded clear euhedral zircon, biotite, and apatite (OCH12-2*). An additional collection of two 1-gallon bags (OCH12-2) was made without as much care to only get the pink parts. Dense separates from this additional collection are rich in apatite and zircon.

Palo Duro

At Palo Duro Canyon, a white, well-consolidated, 6-cm thick tephra (OCH11-6) containing biotite and grey nodules was collected (34° 57.072' N, 101° 39.801' W). The tephra outcrops

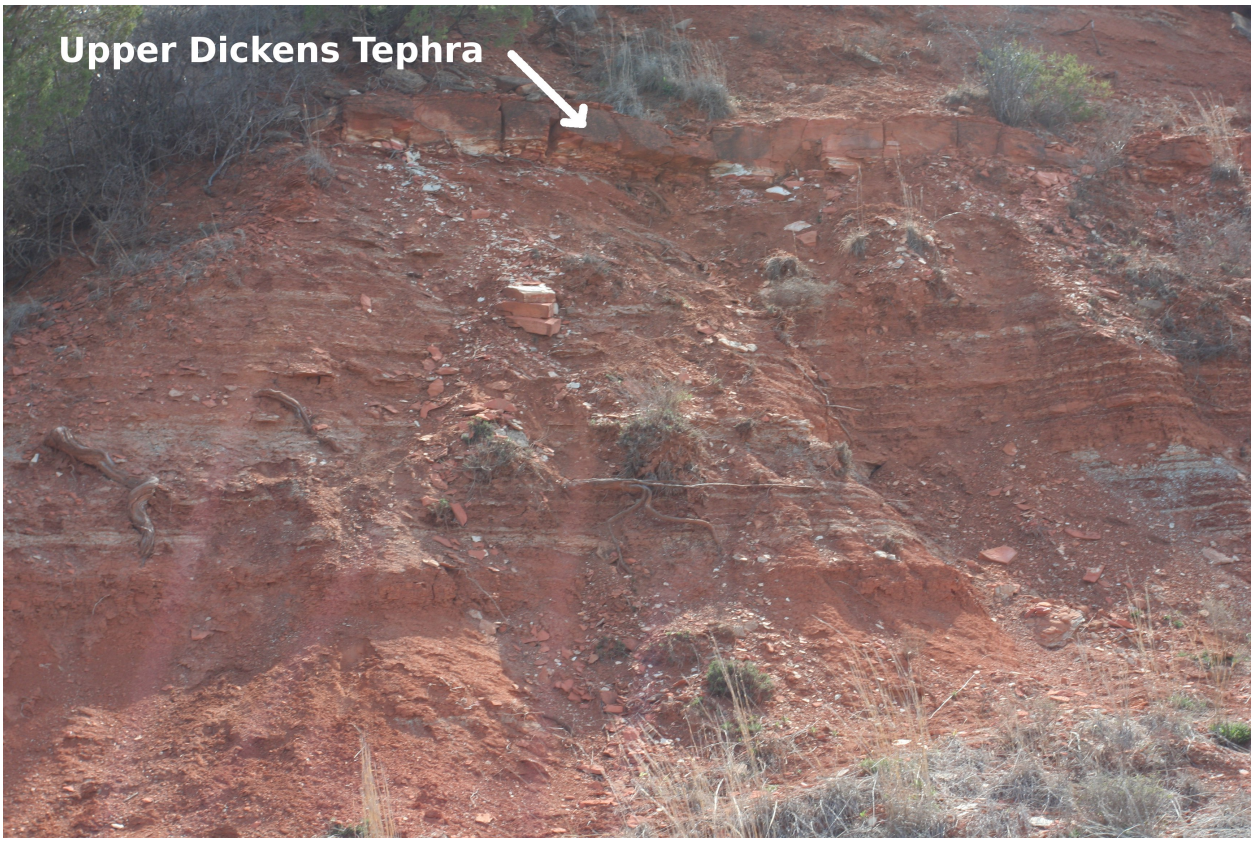

Figure 4.4: Photograph of the Dickens outcrop from where the Upper Dickens tephra was sampled. Photo taken by William S. Mitchell, III.

along the side of a drainage, and was most easily collected on the south side. Another unit was also sampled nearby (OCH12-7, 34° 57.640' N, 101° 40.132' W), with the same stratigraphic position and the same description. These are believed to be laterally correlative. Furthermore, this tephra is believed to be synonymous with PD97-2 and PD08-1 of Chang (*13*).[1]

Highway 207

A tephra sample was also collected from a roadcut (see Figure 4.5) along Texas State Highway 207 (OCH11-4, 34° 48.814' N, 101° 26.071' W). Occurring 10 m above the base of the

[1]The coordinates given by Chang may have been misreported to be 0.6' further east, perhaps from a 7 being mistaken for a 1. With the steep topography to the east, the location as reported would be above the Quartermaster Formation. It is further unclear whether PD97-2 and PD08-1 were separate collections of the same unit, or come from tephra known to be distinct (see p. 117 of Chang).

Figure 4.5: Photograph of the outcrop along Texas Highway 207 (OCH11-4), looking east. In this photograph, only the Quartermaster Formation is visible, although the Whitehorse Formation is not far down the road. The tephra was collected just to the left of center, where lighter rock can be seen on the slope. Photo taken by William S. Mitchell, III.

Quartermaster Formation and roughly 8 m above a Karst surface with paleo-sinkholes of 30–60 cm depth, this tephra appears light pink, is quite friable, and is 4–6 cm thick.

Clarendon

Along County Road X near Clarendon, a 4–6 cm thick light pink tephra was collected (OCH11-5, 34° 50.173' N, 101° 0.637' W). Although the outermost, weathered material was quite friable, the rock was quite competent away from the face of the outcrop. Because the tephra held together well, it was the easiest sample to collect. Unlike other samples which could take an hour or more to collect, this tephra held together and separated from the surrounding rock easily, so collection only took five or ten minutes.

4.3 Methods

Geochronology was performed as described in Chapter 2.

Electron probe microanalysis (EPMA) measurements were carried out on a Cameca SX-50/51 (PC11 DLL) electron microprobe equipped with 5 tunable wavelength dispersive spectrometersat the University of California, Berkeley with the help of Sean Mulcahy.

Biotite EPMA

For biotite measurements, the operating conditions were 40 degrees takeoff angle, and a beam energy of 15 keV. The beam current was 10 nA, and the beam diameter was 10 microns. Elements were acquired using analyzing crystals LIF for Ti ka, Mn ka, Fe ka, PET for Ca ka, K ka, Cl ka, TAP for Al ka, Si ka, Na ka, Mg ka, and WSi60 for F ka. The standards were Fluor-phlogopite (synthetic) for F ka, $Ca_{10}(PO_4)_6Cl_2$ (synthetic chlor-apatite) for Cl ka, Rhodonite for Mn ka, Jadeite (san benito) for Na ka, Diopside (Chesterman) for Si ka, Ca ka, Orthoclase MAD-10 for K ka, Hornblende (Kakanui) USNM 143965 for Al ka, Ilmenite USNM 96189 for Ti ka, and Olivine USNM 2566 (Fo 83) Springwater for Fe ka, Mg ka. The counting time was 30 seconds for all elements. The intensity data was corrected for Time Dependent Intensity (TDI) loss (or gain) using a self calibrated correction for F ka, Na ka, Mg ka, K ka, Ti ka. The off peak counting time was 30 seconds for all elements. Off Peak correction method was Linear for Na ka, Mg ka, Al ka, Si ka, K ka, Ca ka, Ti ka, Mn ka, Fe ka, Cl ka, and High Only for F ka. Unknown and standard intensities were corrected for deadtime. Results are the average of 22 points and detection limits ranged from .014 wt.% for Al ka to .018 wt.% for Na ka to .025 wt.% for Si ka to .067 wt.% for Mn ka to .114 wt.% for F ka. Analytical sensitivity (at the 99% confidence level) ranged from 1.389% relative for Al ka to 2.851% relative for Fe ka to 6.785% relative for F ka to 16.780% relative for Na ka to 144.861% relative for Ca ka. Oxygen was calculated by cation stoichiometry and included in the matrix correction. Oxygen equivalent from halogens (F/Cl/Br/I), was not subtracted in the matrix correction. Points having a concentration of an element indistinguishable from zero at 3σ (99% confidence) were set to zero.

Zircon EPMA

For zircon measurements, the operating conditions were 40 degrees takeoff angle, and a beam energy of 20 keV. The beam current was 100 nA, and the beam diameter was 3 microns. Elements were acquired using analyzing crystals LIF for Ce la, Fe ka, Nd la, Sm la, PET for U ma, Th ma, Zr la, Ca ka, Y la, P ka, Y la, Th ma, U ma, and TAP for Si ka, Hf ma, Hf ma, Mg ka, Al ka, Lu ma. The standards were U-2 (10.00% UO_2 in diopside glass) for U ma, U ma; Th-1 (4.91% ThO_2 in diopside glass) for Th ma, Th ma; Rare Earth glass 'A' for Ce la; Zircon crystal (synthetic) for Si ka, Zr la; Hornblende (Arenal) USNM 111356 for Mg ka, Al ka, Fe ka, Ca ka; Hafnium metal for Hf ma, Hf ma; Neodymium Fluoride (NdF_3) for Nd la; $LuPO_4$ (USNM 168491) for Lu ma; $SmPO_4$ (USNM 168494) for Sm la, and YPO_4

(USNM 168499) for Y la, Y la, P ka. The counting time was 30 seconds for Zr la, Si ka, and 60 seconds for Y la, Ce la, Fe ka, Hf ma, Mg ka, Al ka, Lu ma, Nd la, Sm la, P ka, U ma, Th ma, and Ca ka. The off peak counting time was 30 seconds for Zr la, Si ka, and 60 seconds for Y la, Ce la, Fe ka, Hf ma, Mg ka, Al ka, Lu ma, Nd la, Sm la, P ka, U ma, Th ma, Ca ka. Off Peak correction method was Linear for U ma, Th ma, Si ka, Ca ka, Y la, Ce la, Fe ka, Zr la, Mg ka, Al ka, Lu ma, Nd la, Sm la, P ka, Y la, Th ma, U ma, and Slope (Hi) for Hf ma, Hf ma. Unknown and standard intensities were corrected for deadtime. Standard intensities were corrected for standard drift over time. Results are the average of 14 points and detection limits ranged from .000 wt.% for Hf ma to .003 wt.% for Al ka to .009 wt.% for Fe ka to .021 wt.% for Nd la to .178 wt.% for P ka. Analytical sensitivity (at the 99% confidence level) ranged from .000% relative for Hf ma to .103% relative for Si ka to 13.351% relative for Y la to 61.625% relative for P ka to 385.854% relative for Sm la. Oxygen was calculated by cation stoichiometry and included in the matrix correction. The quantitative blank correction was utilized, and the aggregate intensity option was selected (*22*). Points having element concentrations indistinguishable from zero at 3σ (99% confidence) had that element set to zero for that point. For zircon data, only points having SiO_2 >14 wt.% and having total oxide composition of >90% were included in the analysis.

4.4 Results and Discussion

Tephra Zircon Geochronology

Each of the tephra samples analyzed yielded U-Pb ages of 251.5–252.0 Ma, as shown in Figures 4.6 and 4.7 and quantified in Table 4.1. Grains with a mean age of >255 Ma were not very abundant (∼6%, excluding the detrital sample). Individual analyses leading to the weighted means are shown in Figures 4.8–4.14. All analyses, including those rejected from the weighted means, are tabulated in Appendix B, Tables B.1–B.6.

Sample	Age (Ma)	MSWD	n
Caprock Lower	$251.99 \pm 0.30/0.59/0.69$	2.75	12
Caprock Upper	$251.75 \pm 0.50/0.71/0.76$	2.33	6
Dickens Lower	$251.80 \pm 0.41/0.65/0.70$	3.51	9
Dickens Upper	$251.54 \pm 0.16/0.53/0.59$	1.14	10
Palo Duro	$251.81 \pm 0.20/0.54/0.60$	1.45	23
Highway 207	$251.79 \pm 0.28/0.58/0.64$	2.38	23
Clarendon	$251.92 \pm 0.31/0.59/0.65$	0.89	8

Table 4.1: Age, uncertainty, MSWD, and number of analyses for each of the P-T samples. Uncertainties of the form $\pm x/y/z$ represent the different sources of analytical and systematic uncertainty. Analytical uncertainty is stated as x, while y and z successively incorporate systematic uncertainties from the tracer (0.1%) and decay constant (0.054%). For site-to-site comparison within this study, x should be used. Comparison with other $^{206}Pb/^{238}U$ datasets generated with other tracers, such as the EARTHTIME tracers, should use uncertainty y, and comparison with $^{40}Ar/^{39}Ar$ or other decay schemes should use z.

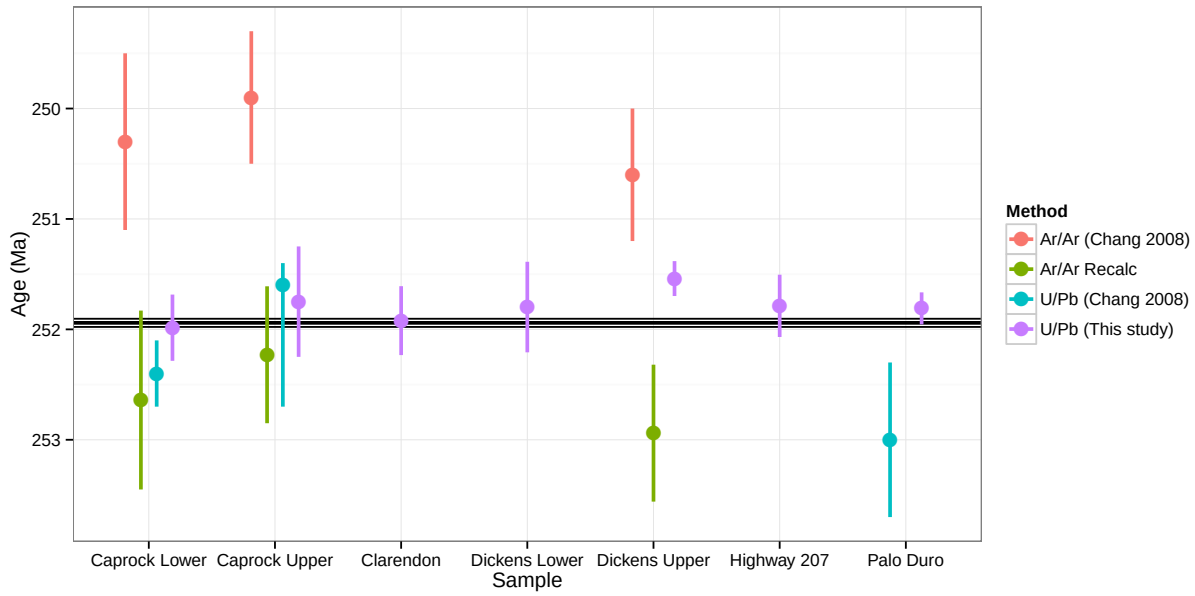

Figure 4.6: Summary of dates for each of the tephra in this study. The horizontal lines represent the age and uncertainty of the mass extinction according to Shen *et al.* (*20*). The Chang 2008 data is as reported in the dissertation (*13*), and the Ar/Ar Recalc has been recalculated according to Renne *et al.* (2010, 2011) (*14*, *15*). All uncertainties are at the 2-sigma level. $^{40}Ar/^{39}Ar$ ages include systematic uncertainties including decay constant uncertainties. U/Pb ages do not include uncertainties from tracer calibration or decay constant uncertainty. Note that the uncertainty in the ^{238}U decay constant would be partially correlated between the $^{40}Ar/^{39}Ar$and U/Pb systems due to its incorporation in the decay constant calibration (*14*).

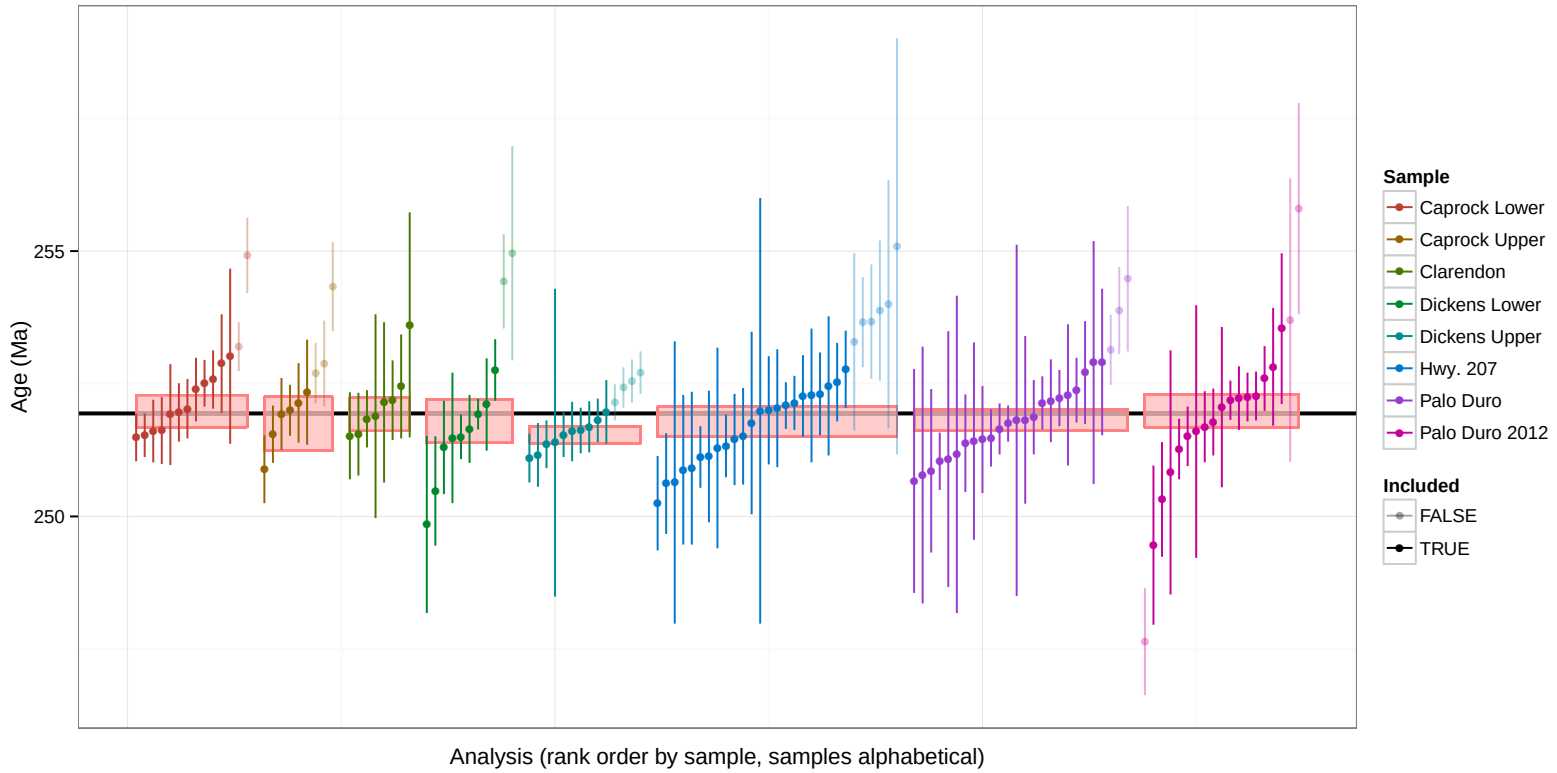

Figure 4.7: Comparison of individual zircon $^{206}Pb/^{238}U$ ages. Within each sample analyses are rank-ordered by age, and samples are in alphabetical order. Analyses which have been excluded from weighted mean calculation are shown in partially shaded symbols. The red boxes correspond to the 2σ uncertainty of the weighted mean for each sample (analytical uncertainty only). The black bar is the central value for the onset of the mass extinction, Bed 25 at the GSSP in Meishan, China, as determined by Burgess *et al.*(*1*).

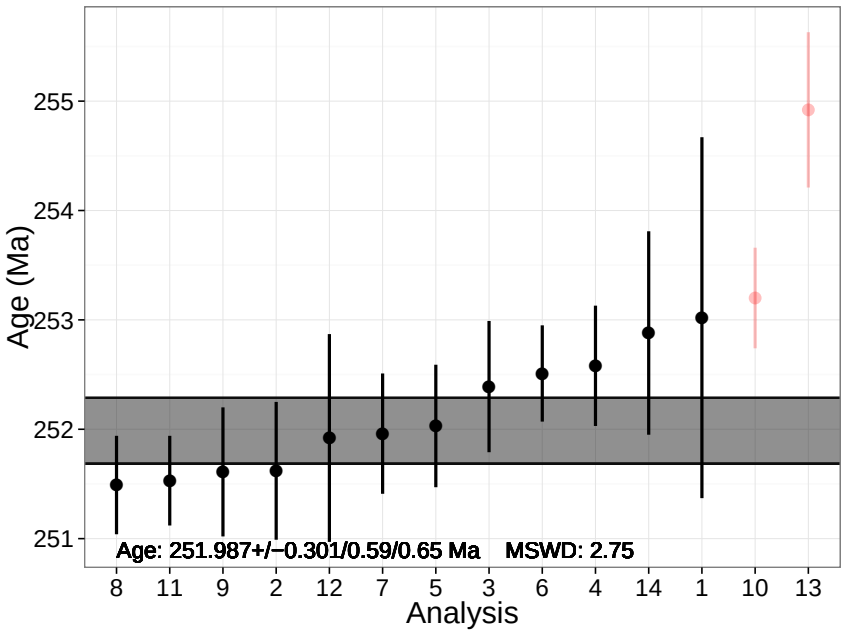

Figure 4.8: Lower Caprock U/Pb Ages

The zircon $^{206}Pb/^{238}U$ ages for Palo Duro are distinctly different than those reported by Chang (*13*), which also appear in the potassium decay-constant calibration of Renne *et al.* (*14*, *15*). When those data were collected, the zircons were not annealed prior to leaching, and were leached with hydrofluoric acid at atmospheric pressure. This treatment has been shown to cause slight reverse discordance in some cases, where uranium is preferrentially leached compared to lead, yielding a bias toward ages older than the "true age" (compare the results of D3t of (*23*) with those for the same sample in (*19*)). Effects of this nature are only observed when both $^{207}Pb/^{235}U$ and $^{206}Pb/^{238}U$ ages are determined with high precision, and even then mainly for older samples. For young samples, the linearity of the Concordia makes these biased ages appear concordant; only when Concordia begins to deviate from its first-order Taylor approximation by an amount greater than the precision of the measurement does the effect appear. While it is possible that a similar—but smaller—effect is present with the annealed and chemically abraded zircons of this study, the technique used here reflects current best practices (*19*, *24*).

At Upper Dickens, the tephra that was sampled appears directly on top of reverse-polarity rocks according to Steiner (*16*), and directly beneath normal-polarity rocks according to Collins *et al.*(in prep.). The tephra itself does not record a paleomagnetic polarity (Collins, pers. comm.). Interpreting the age of the tephra as the age of the reversal is therefore justified. However, Chang proposed a correlation based on mineralogy and biotite chemistry between the Upper Caprock and Upper Dickens tephra (*13*). For that correlation to be

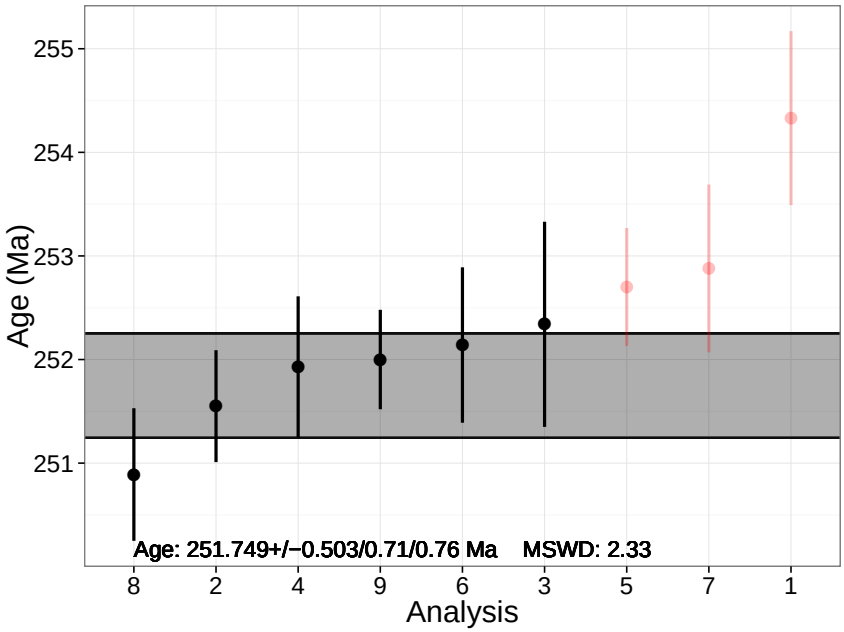

Figure 4.9: Upper Caprock U/Pb Ages

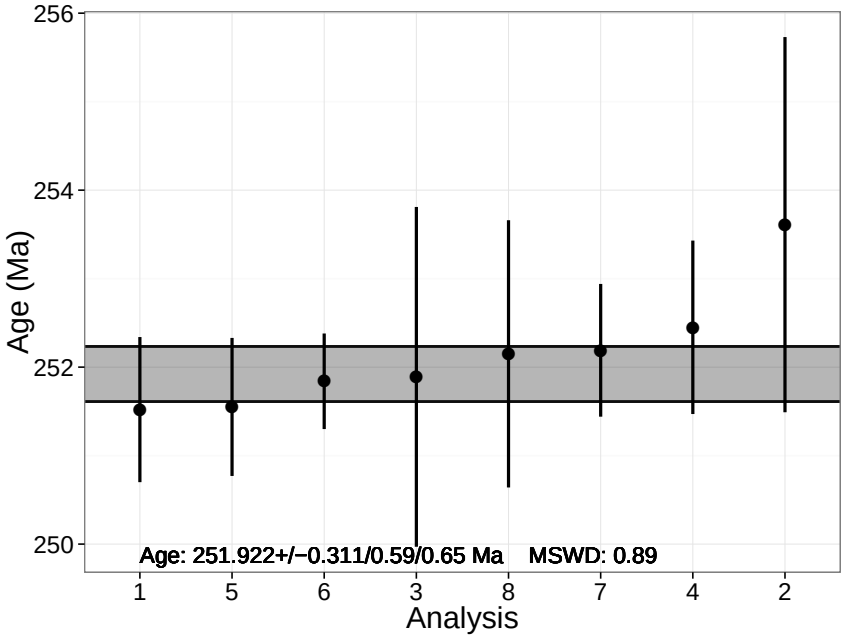

Figure 4.10: Clarendon U/Pb Ages

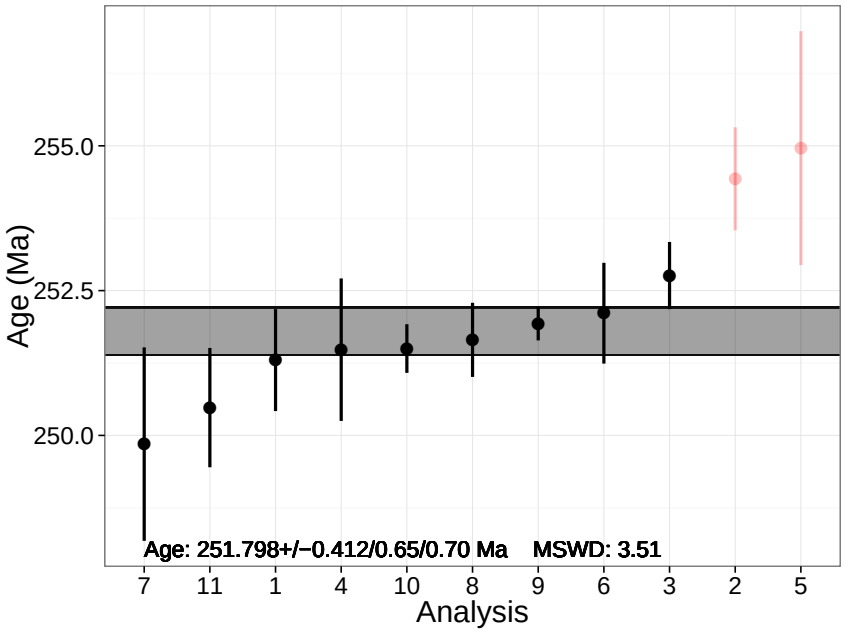

Figure 4.11: Lower Dickens U/Pb Ages

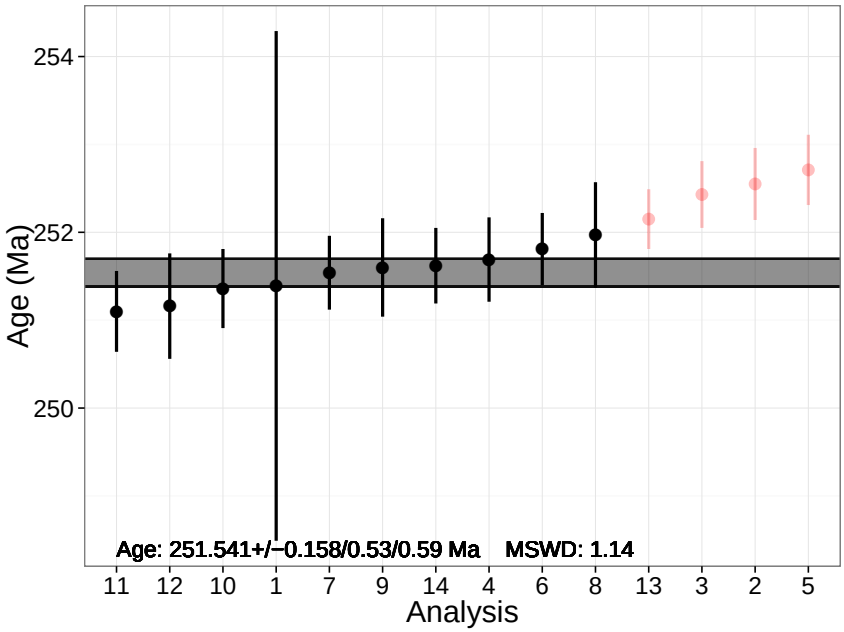

Figure 4.12: Upper Dickens U/Pb Ages

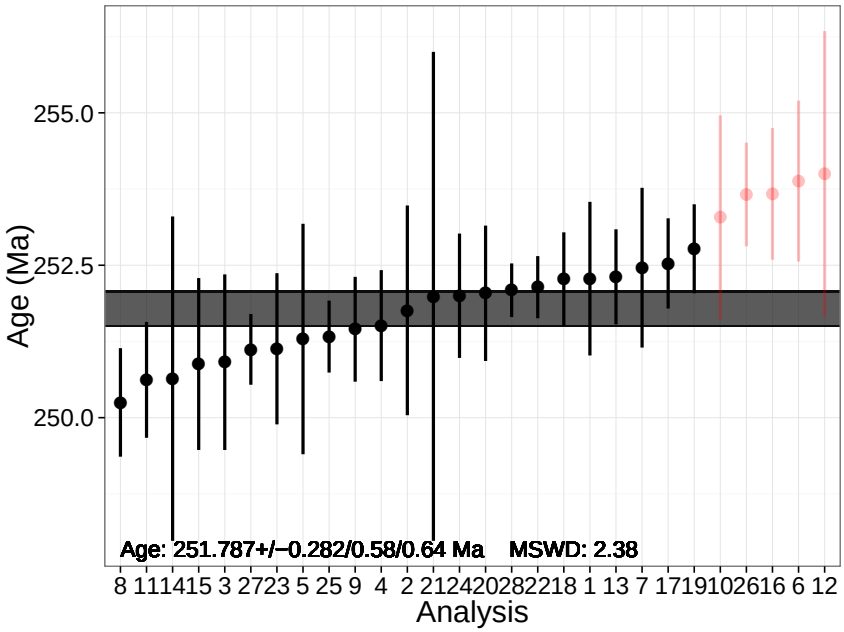

Figure 4.13: Highway 207 U/Pb Ages

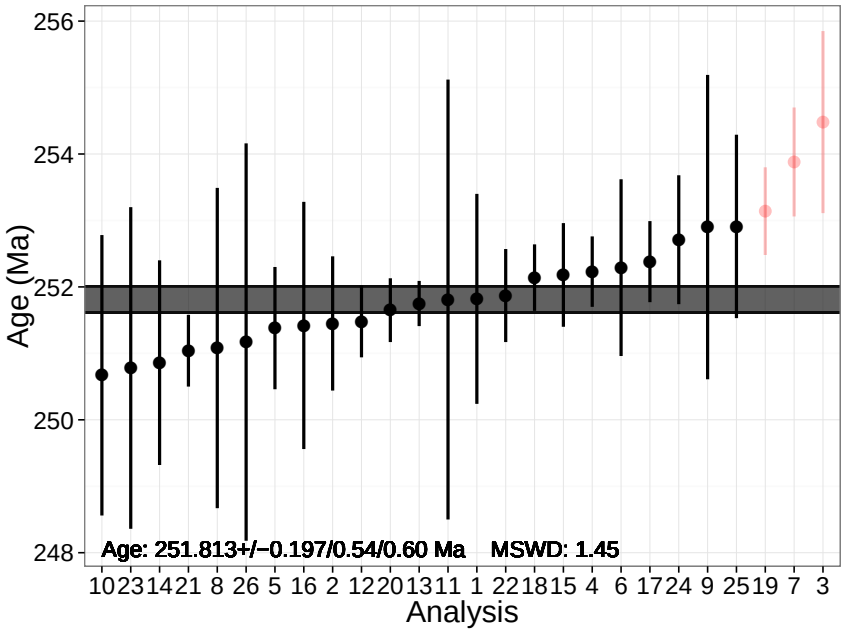

Figure 4.14: Palo Duro U/Pb Ages

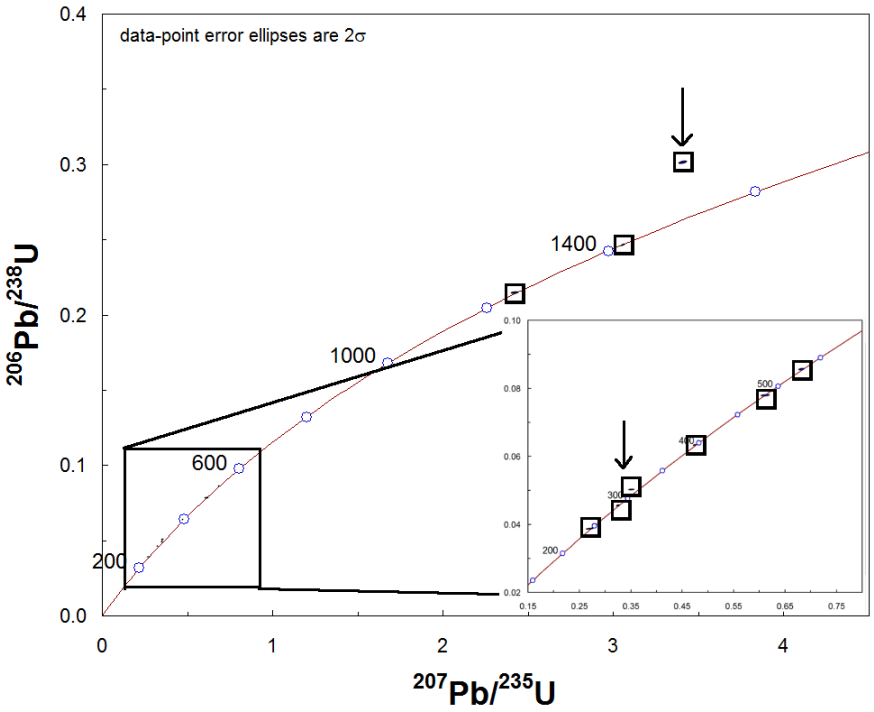

Figure 4.15: Detrital zircon Concordia of the cross-bedded sandstone at Caprock Canyons State Park (sample OCH12-13). Arrows indicate analyses with reverse discordance.

correct, either there is a hiatus directly overlying one of the two tephra, or the magnetic data is unreliable. From the geochronology and the paleomagnetic data, the most plausible interpretation is that the Upper Dickens and Upper Caprock tephra are not correlative.

Detrital Zircon Geochronology

Eleven zircons from the cross-bedded sandstone in the upper portion of the Quartermaster were analyzed, and nine of the analyses were concordant (see Table 4.2). The two analyses which were not on the Concordia are reversely discordant (see Figure 4.15), a result attributed to incomplete dissolution of the zircons or to incomplete dissolution of Pb salts during transfer after acid dissolution. Of the two reversely discordant analyses, one is well over 1 Ga, and the other has both the $^{206}Pb/^{238}U$ and $^{207}Pb/^{235}U$ systems yielding an age of over 300 Ma. Because these analyses are significantly older than the two tephra underlying this sample, they will be disregarded in determining a maximum age of deposition.

One crystal yielded a $^{206}Pb/^{238}U$ age of 244.47 ± 0.66 Ma, younger than the underlying tephra. Because the sandstone is composed of grains which underwent an unknown duration of transport, this youngest age is a maximum age of deposition. Just as with the Signor-Lipps effect in paleontology, it is quite possible that a younger specimen exists but has not yet been

Sample	$\frac{^{206}Pb}{^{238}U}$ Age (Ma)	$\frac{^{207}Pb}{^{235}U}$ Age (Ma)	$\frac{^{207}Pb}{^{206}Pb}$ Age (Ma)
OCH12-13.1_z01_BDS	395.49 ± 0.99	394.14 ± 1.82	386.26 ± 8.26
OCH12-13.1_z02_BDS	315.58 ± 0.85	306.14 ± 4.07	234.78 ± 28.77
OCH12-13.1_z03_BDS	529.65 ± 1.28	528.37 ± 3.46	522.80 ± 12.67
OCH12-13.1_z04_BDS	287.23 ± 0.60	286.60 ± 2.06	281.47 ± 15.00
OCH12-13.1_z05_BDS	286.14 ± 0.44	285.95 ± 1.59	284.41 ± 11.68
OCH12-13.1_z06_BDS	1417.87 ± 3.64	1421.36 ± 4.86	1426.59 ± 3.93
OCH12-13.1_z07_BDS	1250.93 ± 2.96	1248.72 ± 9.02	1244.92 ± 12.46
OCH12-13.1_z08_BDS	483.53 ± 1.11	484.91 ± 5.14	491.38 ± 21.71
OCH12-13.1 z09	244.47 ± 0.66	243.41 ± 4.46	233.24 ± 44.60
OCH12-13.1_z10_BDS	1697.17 ± 4.68	1505.63 ± 8.00	1245.58 ± 8.35
OCH12-13.1 z11	306.37 ± 1.04	306.20 ± 2.49	304.86 ± 18.67

Table 4.2: Detrital zircon ages for cross-bedded sandstone near fossil wood, upper Quartermaster Formation, Caprock Canyons State Park.

found. Given the difference in age of >5 Ma, it is clear that substantial time has been cut away by the channel deposits. The presence of cross-bedded units, formed by meandering streams, suggests that erosion has taken place in this portion of the section, and thus that the paleomagnetic data from these streams must be interpreted very cautiously.

Biotite Chemistry

EPMA results from the biotite found in these tephra are shown in Figures 4.16 and 4.17. In general and as expected, the agreement with Chang (*13*) is very good. Unfortunately, the results for Clarendon also show negatively correlated variation in potassium and calcium that suggest alteration of the biotite. These altered samples must be interpreted with great caution, if at all.

The biotite chemical data suggest that among Upper Caprock, Lower Caprock, and Palo Duro samples, each tephra is distinct. Clarendon shows a large range of compositions, but tellingly has significantly lower K_2O concentrations and substitution of Na and Ca for K, suggesting secondary alteration which renders these data unreliable (see Figure 4.18). Highway 207 has few data points, but it too shows the same signs of alteration.

Comparisons of the Upper Dickens sample to Caprock and Palo Duro are made using the data of Chang (*13*). Those data show Upper Dickens as similar to Upper Caprock, and distinct from Lower Caprock, and Chang concludes that the Upper Dickens tephra is also distinct from Palo Duro.

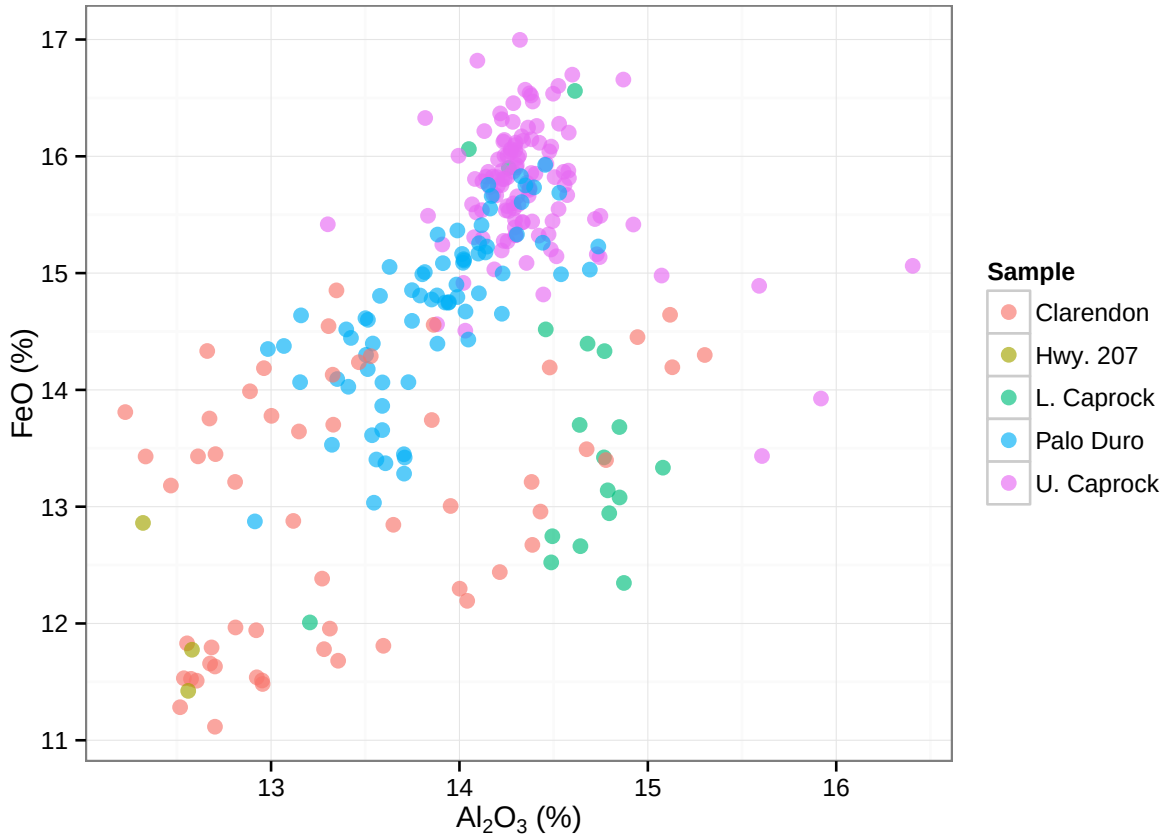

Figure 4.16: Al_2O_3 and FeO concentrations in biotite. Clarendon and the few Highway 207 points span a large range, likely due to alteration (see Figures 4.17 and 4.18). The Upper Caprock, Lower Caprock, and Palo Duro samples appear to be distinct from each other, and in the case of the two Caprock samples, are known to be from different tephra.

Zircon Chemistry

Zircon analyses from the EPMA experiments (Figure 4.19) show that zircons from Palo Duro and Highway 207 have very low UO_2 concentrations, while those from the Upper Caprock tephra have distinctly higher UO_2, suggesting that the Upper Caprock sample is distinct from the tephra at Palo Duro and Highway 207.

Another notable feature is that one of the zircons from Highway 207 contains one grain which has a core of measurable UO_2 but a rim with none (above detection limits). This core is interpreted to be inherited from an earlier crystallization event and may not represent juvenile material. Indeed, the excessive scatter of U-Pb ages in the Highway 207 sample could be caused by such inheritance. If the inherited core is only slightly older than the juvenile rim, it can cause the whole-grain date to be biased toward the older age, with the

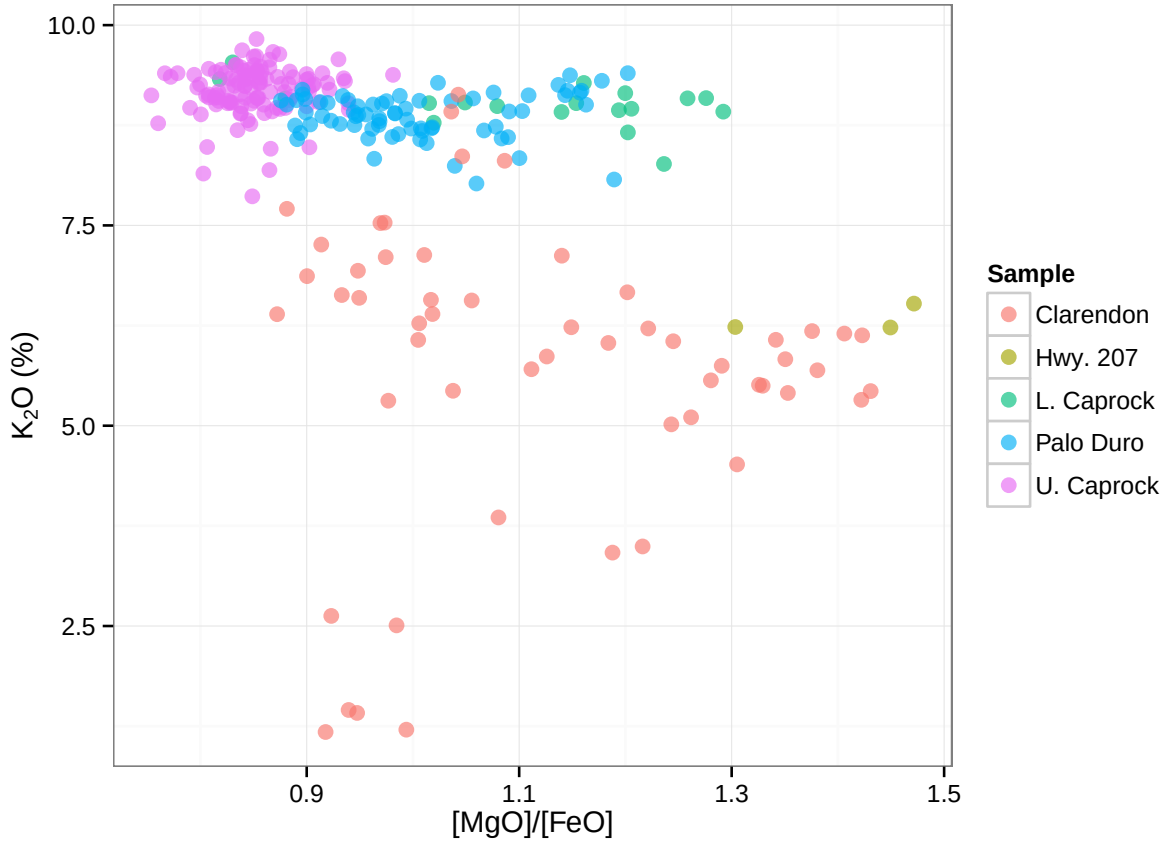

Figure 4.17: MgO/FeO and K_2O concentrations in biotite. Points under ~8.5% K_2O are likely indicative of alteration, suggesting that those points are unreliable for chemical correlation.

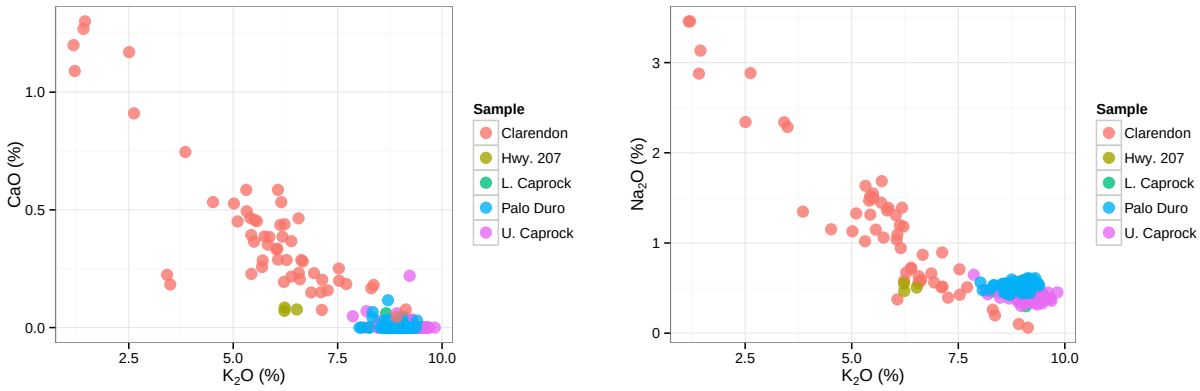

Figure 4.18: Alkali concentration relationships in biotite. Note the substitution of Na and Ca for K in the Clarendon sample, indicating secondary alteration, hence open-system behavior.

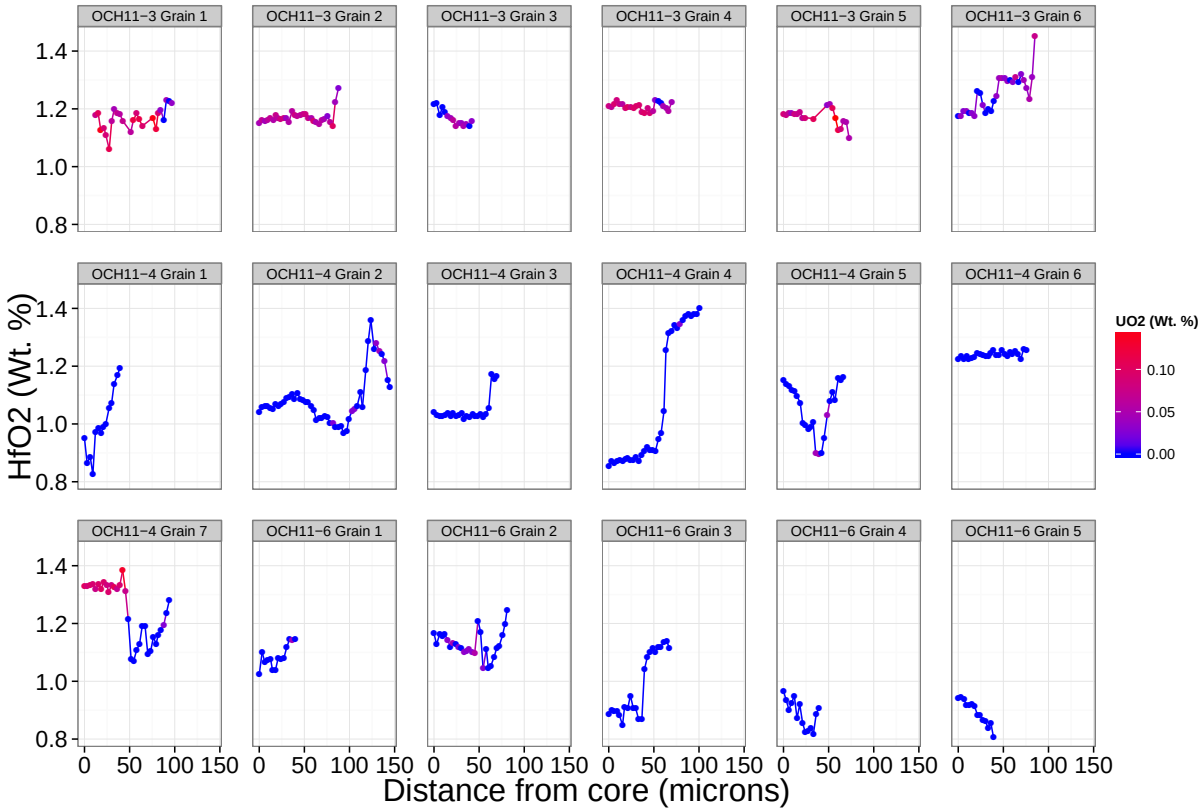

Figure 4.19: Core-to-rim EPMA profiles of Hf and U, reported as weight percent oxides. Upper Caprock (OCH11-3) has higher Hf and U concentrations than Highway 207 (OCH11-4) and Palo Duro (OCH11-6). OCH11-4 Grain 7 shows what appears to be an inherited core, which has a distinctly different chemical composition than the rim of that grain or of the other grains from that sample.

amount of bias for each grain dependent on the fraction of inherited U. Under this model, a juvenile age could be determined by removing data points from the old end of the spectrum until an MSWD of 1 is reached. Any age thus determined would be a model age, and not necessarily more meaningful than the weighted mean age of the original dataset.

Tephra Correlation

The array of data presented in this chapter, combined with paleomagnetic results (Collins *et al.*, in prep.) allow for some correlations (or non-correlations) to be inferred. These relationships and their evidentiary basis are expressed in the correlation matrix in Table 4.3. See Figure 4.2 and the text of the relevant sections for further discussion of these correlations.

Sample	Upper Caprock	Lower Caprock	Upper Dickens	Lower Dickens	Palo Duro	Highway 207	Clarendon
U. Caprock	Y	N[1,4]		N[2]	N[2,3,4]	N[2,3]	
L. Caprock		Y	N[4]	N[2]	N[2,4]	N[2]	
U. Dickens			Y	N[1]	N[4]		
L. Dickens				Y			N[2]
Palo Duro					Y		N[2]
Highway 207						Y	N[2]
Clarendon							Y

Table 4.3: Correlation matrix of tephra. [1] from stratigraphy; [2] from paleomagnetism; [3] from zircon UO_2; [4] from biotite chemistry, including that of Chang (*13*).

4.5 Conclusion

The Quartermaster formation encompasses up to 350 ka of the latest Permian, the P-T Boundary, and continues another 400 ka into the earliest Triassic. The U-Pb data presented here are much higher precision compared to the K/Ar dates of Fracasso and Kolker (*11*), and are more precise than the biotite and sanidine $^{40}Ar/^{39}Ar$ dates of Chang (*13*). Although Lucas and Anderson assigned a latest Permian age to this section (*12*) based on rare fossils found in Briscoe County (the county containing Caprock Canyons State Park) but known only from the Permian Whitehorse strata (*25*), these new zircon $^{206}Pb/^{238}U$ dates provide solid evidence that the strata are very near to—or span—the boundary, with the youngest being clearly Triassic in age.

In the cross-bedded units of the upper Quartermaster Formation, fossilized wood has been found. The youngest detrital zircon $^{206}Pb/^{238}U$ age from the sandstone bearing that fossilized wood is 244.47 ± 0.66 Ma, making the upper Quartermaster Formation definitively Triassic.

4.6 Acknowledgments

Many thanks to Nan West for access to outcrops just northeast of Caprock Canyons, Johnny Fisher for access to the lower Dickens collection area, and the Flying J Ranch for access to the Clarendon outcrop. Additional thanks to Abed Jaouni and J. D. Pierce for assistance with sample preparation and Jay Zambito for asistance in the field. Paul Renne, Roland Mundil, John Geissman, Neil Tabor, T. Scott Meyer, Dyllan Collins, and Jacob Jackson assisted in the field. Thanks to Sean Mulcahy for his assistance with the electron microprobe analyses.

This work was supported by NSF grant #EAR-0844098.

References

1. S. D. Burgess, S. Bowring, S.-z. Shen, *Proceedings of the National Academy of Sciences* **111**, 3316–3321 (2014).
2. I. Metcalfe, Y. Isozaki, *Journal of Asian Earth Sciences* **36**, 407–412 (2009).
3. H. Yin, K. Zhang, J. Tong, Z. Yang, S. Wu, *Episodes* **24**, 102–114 (2001).
4. D. H. Erwin, *The great Paleozoic crisis: life and death in the Permian* (Columbia University Press, 1993).
5. C. Huang, J. Tong, L. Hinnov, Z. Q. Chen, *Geology* **39**, 779–782 (2011).
6. P. W. Signor, J. H. Lipps, *Geological Society of America Special Papers* **190**, 291–296 (1982).
7. M. Magaritz, W. T. Holser, in *Abhandlungen der Geologischen Bundesanstalt in Wien 45*, ed. by W. T. Holser, H.-P. Schönlaub (Abhandlungen der Geologischen Bunesanstalt, May 1991), chap. The Permian-Triassic of the Gartnerkofel-1 Core (Carnic Alps, Austria): Carbon and Oxygen Isotope Variation, pp. 149–163.
8. M. J. d. Wit *et al.*, English, *The Journal of Geology* **110**, pages (2002).
9. C. Korte, H. W. Kozur, *Journal of Asian Earth Sciences* **39**, 215–235 (2010).
10. C. Looy, R. Kirchholtes, G. Mack, T. B. Van Hoof, N. Tabor, presented at the 2011 Geological Society of America Annual Meeting, October 9–12, Minneapolis, MN.
11. M. A. Fracasso, A. Kolker, *West Texas Geological Society Bulletin* **24**, 5–10 (1985).
12. S. G. Lucas, O. J. Anderson, in *New Mexico Geological Society Guidebook, 44th Field Conference, Carlsbad Region, New Mexico and West Texas*, ed. by D. W. Love, J. W. Hawley, B. S. Kues, G. S. Austin, S. G. Lucas (New Mexico Geological Society, 1993), chap. Stratigraphy of the Permian-Triassic Boundary in Southeastern New Mexico and West Texas, pp. 219–230.
13. S.-C. Chang, PhD thesis, University of California, Berkeley, 2008.
14. P. R. Renne, R. Mundil, G. Balco, K. Min, K. R. Ludwig, *Geochimica et Cosmochimica Acta* **74**, 5349–5367 (2010).
15. P. R. Renne, G. Balco, K. R. Ludwig, R. Mundil, K. Min, *Geochimica et Cosmochimica Acta* **75**, 5097–5100 (2011).
16. M. B. Steiner, in *New Mexico Geological Society Guidebook, 52nd Field Conference, Geology of the Llano Estacado*, ed. by S. G. Lucas, D. S. Ulmer-Scholle (New Mexico Geological Society, 2001), chap. Magnetostratigraphic Correlation and Dating of West Texas and New Mexico Late Permian Strata, pp. 59–68.
17. P. R. Renne, M. T. Black, Z. Zichao, M. A. Richards, A. R. Basu, *Science* **269**, 1413–1416 (1995).

18. M. K. Reichow *et al.*, *Earth and Planetary Science Letters* **277**, 9–20 (2009).

19. R. Mundil, K. R. Ludwig, I. Metcalfe, P. R. Renne, *Science* **305**, 1760–1763 (2004).

20. S.-z. Shen *et al.*, *Science* **334**, 1367–1372 (2011).

21. M. Szurlies, *Geological Society, London, Special Publications* **376**, 73–85 (2013).

22. J. J. Donovan, H. A. Lowers, B. G. Rusk, *American Mineralogist* **96**, 274–282 (2011).

23. R. Mundil *et al.*, *Earth and Planetary Science Letters* **187**, 131–145 (2001).

24. J. M. Mattinson, *Chemical Geology* **220**, 47–66 (2005).

25. R. I. Roth, N. D. Newell, B. H. Burma, *Journal of Paleontology* **15**, 312–317 (1941).

Appendix A

Data tables for Chapter 3

Sample	CA time (h)	Spk	U-Pb sep.	$\frac{^{206}Pb}{^{238}U}$ (Ma)	Pb_c (pg)	$\frac{Th}{U}$	$\frac{^{207}Pb}{^{235}U}$ (%2σ)	$\frac{^{206}Pb}{^{238}U}$ (%2σ)	ρ	$\frac{^{206}Pb}{^{204}Pb}$	$\frac{^{207}Pb}{^{206}Pb}$ (%2σ)
BB11-1.1_z01_BDS	12	BDS[a]	No	64.61 ± 0.15	1.0	0.5	0.0664 ± 2.69	0.01007 ± 0.23	0.58	289.5	0.0478 ± 2.57
BB11-1.1_z02_BDS	12	BDS[a]	No	64.81 ± 0.29	1.9	0.4	0.0656 ± 7.39	0.01010 ± 0.45	0.72	105.3	0.0471 ± 7.08
BB11-1.1_z03_BDS	12	BDS[a]	No	64.64 ± 0.48	2.2	0.6	0.0667 ± 13.40	0.01008 ± 0.75	0.79	67.4	0.0480 ± 12.82
BB11-1.1_z04_BDS	*12*	*BDS[a]*	*No*	68.16 ± 0.63	*2.0*	*0.6*	0.0583 ± 20.24	0.01063 ± 0.93	*0.78*	*56.1*	0.0397 ± 19.52
BB11-1.1_z05_BDS	12	BDS[a]	No	65.11 ± 0.56	0.9	0.9	0.0607 ± 16.75	0.01015 ± 0.85	0.81	66.9	0.0433 ± 16.07
BB11-1.1_z07_BDS	12	BDS[a]	No	65.06 ± 0.29	0.8	0.4	0.0684 ± 5.95	0.01014 ± 0.45	0.65	134.4	0.0489 ± 5.67
BB11-1.1_z09_BDS	12	BDS[a]	No	64.75 ± 0.22	0.6	0.5	0.0686 ± 5.17	0.01009 ± 0.35	0.71	161.2	0.0493 ± 4.93
HC-1PR.Z01	*12*	*BW[a]*	*No*	108.02 ± 1.17	*1.5*	*0.2*	0.1619 ± 1.73	0.01690 ± 1.08	*0.69*	*716.4*	0.0695 ± 1.26
HC-1PR.Z02	*12*	*BW[a]*	*No*	933.21 ± 17.23	*2.6*	*0.3*	4.3835 ± 1.90	0.15577 ± 1.85	*0.98*	*2023.4*	0.2041 ± 0.42
HC-1PR.Z03	*12*	*BW[a]*	*No*	117.61 ± 1.42	*1.9*	*0.7*	0.1876 ± 4.26	0.01841 ± 1.21	*0.48*	*280.9*	0.0739 ± 3.83
HC-1PR.Z04	12	BW[a]	No	66.14 ± 0.30	2.5	0.2	0.0691 ± 7.66	0.01031 ± 0.46	0.85	168.1	0.0486 ± 7.27
HC-1PR.Z05	*12*	*BW[a]*	*No*	85.34 ± 0.62	*1.5*	*0.3*	0.1575 ± 1.91	0.01333 ± 0.73	*0.56*	*389.6*	0.0857 ± 1.61
HC-1PR.Z06	*12*	*BW[a]*	*No*	237.52 ± 14.58	*1.6*	*0.1*	0.4836 ± 6.20	0.03753 ± 6.15	*0.99*	*778.8*	0.0934 ± 0.75
HC-1PR.Z07	*12*	*BW[a]*	*No*	100.71 ± 1.13	*1.6*	*0.7*	0.1229 ± 16.89	0.01575 ± 1.12	*0.88*	*76.9*	0.0566 ± 15.91
HC-1PR.Z08	*12*	*BW[a]*	*No*	1274.30 ± 8.29	*1.8*	*0.3*	3.2151 ± 0.84	0.21857 ± 0.65	*0.83*	*1338.1*	0.1067 ± 0.47
HC-1PR.Z09	*12*	*BW[a]*	*No*	351.07 ± 1.36	*1.9*	*0.3*	0.8155 ± 0.85	0.05597 ± 0.39	*0.56*	*1310.0*	0.1057 ± 0.71

Table A.1: Data from the Biscuit Butte U Coal tephra (BB11-1) and a Lerbekmo Site Z Coal tephra (HC-1PR). *CA Time* is the leaching time for chemical abrasion. *Spk* is the spike used for the analysis; [a] denotes samples corrected for mass fractionation using an average value for analyses of NBS 981, while [b] denotes cycle-by-cycle corrections from the $^{202}Pb/^{205}Pb$ ratio. *U-Pb sep.* indicates whether anion exchange chemistry was used. Pb_c is common Pb including analytical blank (blank composition is found in Table 2.1). *Th/U* ratio is the present-day Th/U ratio calculated from radiogenic $^{208}Pb/^{206}Pb$ and the $^{206}Pb/^{238}U$ age, assuming a Th/U of 4 for the crystallizing magma. The $^{206}Pb/^{204}Pb$ ratio is corrected for tracer contribution and mass fractionation. Other isotopic ratios are corrected for mass fractionation, tracer contribution, and common lead contribution. ρ is the correlation coefficient of radiogenic $^{207}Pb/^{235}U$ with $^{206}Pb/^{238}U$. Uncertainties are given at 2σ and do not include tracer calibration (0.1%) or decay constant (0.054%) uncertainties. Data excluded from weighted means are italicized and in red.

Sample	CA time (h)	Spk	U-Pb sep.	$\frac{^{206}Pb}{^{238}U}$ (Ma)	Pb_c (pg)	$\frac{Th}{U}$	$\frac{^{207}Pb}{^{235}U}$ (%2σ)	$\frac{^{206}Pb}{^{238}U}$ (%2σ)	ρ	$\frac{^{206}Pb}{^{204}Pb}$	$\frac{^{207}Pb}{^{206}Pb}$ (%2σ)
BC11-1.1_z02_BDS	*8*	*BDS*[a]	*No*	251.06 ± 0.79	*1.5*	*0.7*	0.2809 ± 1.39	0.03971 ± 0.31	*0.40*	*443.2*	0.0513 ± 1.29
BC11-1.1_z03_BDS	8	BDS[a]	No	66.31 ± 0.28	1.3	0.3	0.0670 ± 2.15	0.01034 ± 0.42	0.39	328.5	0.0470 ± 2.02
BC11-1.1_z04_BDS	*8*	*BDS*[a]	*No*	252.84 ± 1.84	*1.0*	*1.3*	0.2917 ± 7.75	0.04000 ± 0.73	*0.56*	*92.2*	0.0529 ± 7.37
BC11-1.1_z06_BDS	*8*	*BDS*[a]	*No*	246.47 ± 1.36	*0.7*	*1.1*	0.2752 ± 6.44	0.03897 ± 0.55	*0.62*	*134.7*	0.0512 ± 6.11
BC11-1.1_z07_BDS	*8*	*BDS*[a]	*No*	250.20 ± 1.54	*0.8*	*1.1*	0.2964 ± 8.21	0.03958 ± 0.62	*0.68*	*91.6*	0.0543 ± 7.80
BC11-1.1_z10_BDS	*8*	*BDS*[a]	*No*	99.97 ± 0.49	*1.1*	*0.6*	0.1104 ± 7.57	0.01563 ± 0.49	*0.75*	*104.7*	0.0512 ± 7.21
BC11-1.1_z11_BDS	8	BDS[a]	No	66.32 ± 0.19	1.0	0.3	0.0687 ± 3.77	0.01034 ± 0.28	0.63	209.8	0.0482 ± 3.59
BC11-1.1_z12_BDS	8	BDS[a]	No	66.39 ± 0.14	1.1	0.3	0.0672 ± 2.80	0.01035 ± 0.21	0.61	256.9	0.0471 ± 2.68
BC11-1.1_z13_BDS	*8*	*BDS*[a]	*No*	254.53 ± 1.08	*1.0*	*1.1*	0.2907 ± 4.34	0.04027 ± 0.42	*0.55*	*162.4*	0.0523 ± 4.12
BC-1PR.z08_BDS	*12*	*BDS*[a]	*No*	66.95 ± 0.12	*1.1*	*0.4*	0.0684 ± 2.15	0.01044 ± 0.18	*0.55*	*315.4*	0.0475 ± 2.06
BC-1PR.z09_BDS	*12*	*BDS*[a]	*No*	209.57 ± 1.16	*1.4*	*0.1*	0.2253 ± 8.86	0.03304 ± 0.56	*0.72*	*94.7*	0.0494 ± 8.46
BC-1PR.z10_BDS	*12*	*BDS*[a]	*No*	72.89 ± 0.29	*1.1*	*0.5*	0.0746 ± 6.57	0.01137 ± 0.40	*0.73*	*119.4*	0.0476 ± 6.29
BC-1PR5.z01_BDS	*9*	*BDS*[a]	*No*	150.39 ± 0.42	*1.0*	*0.4*	0.1597 ± 1.47	0.02360 ± 0.28	*0.40*	*447.7*	0.0491 ± 1.39
BC-1PR5.z02_BDS	*9*	*BDS*[a]	*No*	172.68 ± 0.96	*1.3*	*0.7*	0.1800 ± 8.87	0.02715 ± 0.56	*0.72*	*93.7*	0.0481 ± 8.47
BC-1PR.Z03	12	BW[a]	No	66.44 ± 1.08	1.2	0.5	0.0730 ± 27.67	0.01036 ± 1.63	0.89	57.9	0.0511 ± 26.22
BC-1PR.Z04	12	BW[a]	No	66.54 ± 1.31	1.3	0.4	0.0685 ± 4.23	0.01038 ± 1.98	0.55	329.5	0.0479 ± 3.56
BC-1PR.Z06	12	BW[a]	No	66.51 ± 0.58	1.4	0.4	0.0680 ± 8.40	0.01037 ± 0.87	0.55	160.6	0.0475 ± 7.95
BC-1PR.Z07	*12*	*BW*[a]	*No*	76.75 ± 1.83	*1.5*	*0.5*	0.0794 ± 5.65	0.01198 ± 2.38	*0.51*	*248.9*	0.0481 ± 4.88
BC-2PR.Z01	12	BW[a]	No	65.95 ± 0.40	1.6	0.7	0.0694 ± 10.43	0.01028 ± 0.61	0.87	126.8	0.0490 ± 9.90
BC-2PR.Z02	12	BW[a]	No	65.91 ± 0.74	1.6	0.6	0.0722 ± 18.93	0.01028 ± 1.13	0.90	77.5	0.0510 ± 17.93
BC-2PR.Z03	12	BW[a]	No	66.06 ± 0.71	1.5	0.5	0.0723 ± 18.29	0.01030 ± 1.08	0.89	78.0	0.0509 ± 17.34
BC-2PR.Z04	12	BW[a]	No	65.49 ± 0.98	1.7	0.5	0.0663 ± 27.35	0.01021 ± 1.49	0.90	62.4	0.0471 ± 26.01
BC-2PR.Z05	12	BW[a]	No	66.26 ± 0.21	1.6	0.5	0.0713 ± 4.14	0.01033 ± 0.31	0.72	292.0	0.0500 ± 3.93
BC-2PR.Z07	12	BW[a]	No	66.17 ± 0.29	1.7	0.6	0.0667 ± 6.37	0.01032 ± 0.44	0.66	223.5	0.0469 ± 6.08

Table A.2: Data from the Bug Creek Null Coal tephra (BC-1PR and BC11-1) and a Bug Creek Z Coal tephra (BC-2PR).

Sample	CA time (h)	Spk	U-Pb sep.	$\frac{^{206}Pb}{^{238}U}$ (Ma)	Pb_c (pg)	$\frac{Th}{U}$	$\frac{^{207}Pb}{^{235}U}$ (%2σ)	$\frac{^{206}Pb}{^{238}U}$ (%2σ)	ρ	$\frac{^{206}Pb}{^{204}Pb}$	$\frac{^{207}Pb}{^{206}Pb}$ (%2σ)
HF-3PR.Z01	*12*	*BW*[a]	*No*	770.04 ± 1.95	*1.6*	*0.2*	3.7557 ± 0.32	0.12688 ± 0.25	*0.89*	*1600.4*	0.2147 ± 0.15
HF-3PR.Z02	12	BW[a]	No	65.94 ± 0.88	1.4	0.8	0.0710 ± 21.45	0.01028 ± 1.34	0.85	71.6	0.0501 ± 20.32
HF-3PR.Z03	*12*	*BW*[a]	*No*	73.84 ± 1.29	*2.3*	*0.6*	0.0836 ± 28.01	0.01152 ± 1.75	*0.88*	*56.1*	0.0526 ± 26.48
HF-3PR.Z04	12	BW[a]	No	65.59 ± 1.24	1.3	0.6	0.0689 ± 28.56	0.01023 ± 1.90	0.78	59.2	0.0488 ± 27.10
HF-3PR.Z05	12	BW[a]	No	65.54 ± 1.68	1.5	0.7	0.0729 ± 43.10	0.01022 ± 2.57	0.88	43.8	0.0517 ± 40.85
HF-3PR.Z06	12	BW[a]	No	66.42 ± 0.95	1.5	0.7	0.0779 ± 21.61	0.01036 ± 1.43	0.88	68.2	0.0545 ± 20.37
HF-3PR.Z07	12	BW[a]	No	65.20 ± 2.84	1.3	0.8	0.0759 ± 69.55	0.01017 ± 4.36	0.90	33.3	0.0541 ± 65.66
HF-3PR.Z08	12	BW[a]	No	65.23 ± 1.22	1.3	0.6	0.0670 ± 33.84	0.01017 ± 1.87	0.89	53.1	0.0478 ± 32.19
HF-3PR.Z09	12	BW[a]	No	65.61 ± 1.34	1.3	0.6	0.0684 ± 36.31	0.01023 ± 2.04	0.90	51.0	0.0485 ± 34.48
HF-3PR.Z10	12	BW[a]	No	65.74 ± 1.79	1.5	0.8	0.0822 ± 40.32	0.01025 ± 2.73	0.90	42.4	0.0581 ± 37.90
HF-3PR4.z02_BDS	12	BDS[a]	No	66.37 ± 0.31	1.2	0.7	0.0657 ± 7.67	0.01035 ± 0.46	0.71	108.2	0.0460 ± 7.35
HF-3PR4.z03_BDS	12	BDS[a]	No	66.03 ± 0.23	0.8	1.0	0.0679 ± 5.42	0.01030 ± 0.35	0.70	142.4	0.0478 ± 5.18
HF-3PR4.z04_BDS	12	BDS[a]	No	66.01 ± 0.33	0.7	0.8	0.0700 ± 7.75	0.01029 ± 0.50	0.76	118.4	0.0493 ± 7.38
HF-3PR4.z05_BDS	12	BDS[a]	No	65.66 ± 0.18	1.3	0.7	0.0646 ± 3.73	0.01024 ± 0.28	0.61	233.7	0.0458 ± 3.56
HF-3PR4.z06_BDS	12	BDS[a]	No	66.52 ± 0.50	1.5	0.7	0.0707 ± 11.87	0.01037 ± 0.75	0.74	74.1	0.0494 ± 11.33
HF-3PR4.z07_BDS	12	BDS[a]	No	65.62 ± 0.82	1.7	0.6	0.0557 ± 26.30	0.01023 ± 1.25	0.81	54.5	0.0395 ± 25.30
HF-3PR4.z08_BDS	*12*	*BDS*[a]	*No*	75.00 ± 1.12	*3.3*	*0.6*	0.0841 ± 12.51	0.01170 ± 1.49	*0.50*	*77.4*	0.0521 ± 11.84
HF-3PR4.z10_BDS	12	BDS[a]	No	66.20 ± 0.20	1.0	0.6	0.0650 ± 4.57	0.01032 ± 0.31	0.65	175.0	0.0457 ± 4.38
HF1PR.Z01	*12*	*BW*[a]	*No*	76.15 ± 1.17	*2.0*	*0.5*	0.0840 ± 25.99	0.01188 ± 1.54	*0.90*	*60.1*	0.0513 ± 24.62
HF1PR.Z02	*12*	*BW*[a]	*No*	74.41 ± 0.75	*1.7*	*0.7*	0.0774 ± 17.79	0.01161 ± 1.01	*0.88*	*84.4*	0.0483 ± 16.90
HF1PR.Z03	*12*	*BW*[a]	*No*	75.38 ± 0.50	*2.2*	*0.6*	0.0811 ± 10.25	0.01176 ± 0.66	*0.82*	*127.8*	0.0500 ± 9.72
HF1PR.Z04	12	BW[a]	No	66.15 ± 0.41	2.9	0.1	0.0684 ± 6.91	0.01031 ± 0.62	0.61	187.4	0.0481 ± 6.55
HF1PR.Z05	*12*	*BW*[a]	*No*	66.83 ± 0.32	*1.7*	*0.0*	0.0681 ± 1.65	0.01042 ± 0.48	*0.43*	*811.0*	0.0474 ± 1.50
HF1PR.Z06	*12*	*BW*[a]	*No*	116.75 ± 1.01	*1.9*	*0.5*	0.1222 ± 14.09	0.01828 ± 0.86	*0.82*	*102.5*	0.0485 ± 13.39
HF1PR.Z07	*12*	*BW*[a]	*No*	74.08 ± 0.39	*1.4*	*0.8*	0.0770 ± 7.07	0.01156 ± 0.52	*0.72*	*194.6*	0.0483 ± 6.71
HF-1PR.Z09	*12*	*BW*[a]	*No*	75.77 ± 0.82	*1.3*	*0.6*	0.0788 ± 18.99	0.01182 ± 1.08	*0.90*	*82.0*	0.0483 ± 18.03
HF-1PR.Z10	*12*	*BW*[a]	*No*	96.27 ± 1.72	*1.8*	*0.8*	0.1067 ± 29.66	0.01505 ± 1.79	*0.89*	*55.2*	0.0514 ± 28.08
HF-1PR.Z11	*12*	*BW*[a]	*No*	74.75 ± 3.77	*1.3*	*0.6*	0.0930 ± 75.80	0.01166 ± 5.05	*0.90*	*31.8*	0.0577 ± 71.28
HF-1PR_z12_BDS	*12*	*BDS*[a]	*No*	1927.79 ± 5.68	*1.1*	*0.2*	7.3048 ± 0.33	0.34857 ± 0.29	*0.94*	*5010.4*	0.1520 ± 0.11
HF-1PR_z13_BDS	*12*	*BDS*[a]	*No*	114.12 ± 0.67	*1.6*	*0.4*	0.1164 ± 9.10	0.01786 ± 0.59	*0.68*	*94.1*	0.0473 ± 8.71
HF-1PR_z14_BDS	*12*	*BDS*[a]	*No*	995.50 ± 3.16	*0.9*	*0.1*	2.3671 ± 0.62	0.16699 ± 0.32	*0.63*	*617.4*	0.1028 ± 0.49
HF-1PR_z15_BDS	*12*	*BDS*[a]	*No*	1745.63 ± 7.44	*0.9*	*0.3*	4.5945 ± 0.51	0.31100 ± 0.43	*0.87*	*2040.8*	0.1071 ± 0.25

Table A.3: Data from the Hauso Flats IrZ Coal tephra (HF-1PR) and the stratigraphically higher Hauso Flats HFZ Coal tephra (HF-3PR).

Sample	CA time (h)	Spk	U-Pb sep.	$\frac{^{206}Pb}{^{238}U}$ (Ma)	Pb_c (pg)	$\frac{Th}{U}$	$\frac{^{207}Pb}{^{235}U}$ (%2σ)	$\frac{^{206}Pb}{^{238}U}$ (%2σ)	ρ	$\frac{^{206}Pb}{^{204}Pb}$	$\frac{^{207}Pb}{^{206}Pb}$ (%2σ)
JT11-3.z01_BDS	*12*	*BDS*[a]	*No*	66.36 ± 0.29	*2.0*	*0.5*	0.0677 ± 7.38	0.01035 ± 0.43	*0.75*	*107.0*	0.0475 ± 7.06
JT11-3.z02_BDS	12	BDS[a]	No	65.94 ± 0.24	1.0	0.5	0.0653 ± 4.28	0.01028 ± 0.36	0.59	231.7	0.0460 ± 4.08
JT11-3.z03_BDS	12	BDS[a]	No	65.81 ± 0.19	0.8	0.6	0.0673 ± 3.60	0.01026 ± 0.29	0.59	211.5	0.0476 ± 3.44
JT11-3.z04_BDS	*12*	*BDS*[a]	*No*	66.80 ± 0.36	*0.9*	*0.5*	0.0738 ± 8.28	0.01042 ± 0.55	*0.74*	*97.9*	0.0514 ± 7.89
JT11-3.1_z01_BDS	*10*	*BDS*[a]	*No*	66.32 ± 0.16	*1.0*	*0.5*	0.0675 ± 1.08	0.01034 ± 0.24	*0.39*	*632.6*	0.0474 ± 1.01
JT11-3.1_z02_BDS	10	BDS[a]	No	66.06 ± 0.18	0.9	0.5	0.0683 ± 3.08	0.01030 ± 0.27	0.55	232.3	0.0481 ± 2.94
JT11-3.1_z03_BDS	10	BDS[a]	No	66.20 ± 0.12	1.0	0.7	0.0674 ± 1.66	0.01032 ± 0.18	0.48	444.5	0.0473 ± 1.58
JT11-3.1_z04_BDS	*10*	*BDS*[a]	*No*	96.01 ± 0.27	*1.2*	*0.7*	0.0996 ± 2.36	0.01501 ± 0.28	*0.45*	*290.5*	0.0481 ± 2.25
JT11-3.1_z05_BDS	10	BDS[a]	No	66.12 ± 0.11	1.1	0.5	0.0675 ± 1.35	0.01031 ± 0.16	0.45	515.1	0.0475 ± 1.29
JT11-3.1_z06_BDS	10	BDS[a]	No	66.06 ± 0.16	0.9	0.5	0.0670 ± 2.25	0.01030 ± 0.24	0.47	300.3	0.0472 ± 2.15
JT11-3.1_z07_BDS	*10*	*BDS*[a]	*No*	67.00 ± 0.20	*1.1*	*0.5*	0.0696 ± 3.75	0.01045 ± 0.30	*0.59*	*190.8*	0.0483 ± 3.58
JT11-3.1_z08_BDS	10	BDS[a]	No	66.12 ± 0.16	1.1	0.4	0.0677 ± 1.84	0.01031 ± 0.25	0.43	366.5	0.0476 ± 1.75
JT11-3.1_z09_BDS	10	BDS[a]	No	66.06 ± 0.13	0.9	0.4	0.0676 ± 2.06	0.01030 ± 0.20	0.50	338.8	0.0476 ± 1.97
JT11-3.1_z10_BDS	10	BDS[a]	No	66.16 ± 0.23	1.0	0.4	0.0678 ± 2.10	0.01032 ± 0.35	0.41	365.1	0.0476 ± 1.98
JT11-3.1_z11_BDS	*10*	*BDS*[a]	*No*	66.34 ± 0.12	*1.1*	*0.4*	0.0678 ± 2.02	0.01034 ± 0.18	*0.53*	*341.9*	0.0475 ± 1.93
JT11-3.1_z12_BDS	*10*	*BDS*[a]	*No*	66.70 ± 0.13	*0.9*	*0.4*	0.0677 ± 2.25	0.01040 ± 0.19	*0.55*	*314.3*	0.0472 ± 2.15
JT11-1.z01_BDS	*12*	*BDS*[a]	*No*	99.46 ± 0.38	*0.9*	*0.7*	0.1090 ± 4.93	0.01555 ± 0.38	*0.69*	*174.6*	0.0509 ± 4.68

Table A.4: Data from the Jared's Trike Z Coal, including the uppermost tephra (JT11-3) and the lowermost tephra (JT11-1).

Sample	CA time (h)	Spk	U-Pb sep.	$\frac{^{206}Pb}{^{238}U}$ (Ma)	Pb_c (pg)	$\frac{Th}{U}$	$\frac{^{207}Pb}{^{235}U}$ (%2σ)	$\frac{^{206}Pb}{^{238}U}$ (%2σ)	ρ	$\frac{^{206}Pb}{^{204}Pb}$	$\frac{^{207}Pb}{^{206}Pb}$ (%2σ)
LG11-1.1_z02_BDS	12	BDS[a]	No	66.08 ± 0.17	1.3	0.2	0.0684 ± 3.38	0.01030 ± 0.26	0.61	245.9	0.0481 ± 3.22
LG11-1.1_4z01_BDS	*12*	*BDS*[a]	*No*	86.19 ± 0.22	*1.6*	*0.2*	0.1160 ± 1.53	0.01346 ± 0.25	*0.46*	*339.0*	0.0625 ± 1.43
LG11-1.1_z04_BDS	*12*	*BDS*[a]	*No*	155.81 ± 0.47	*1.3*	*0.3*	0.4303 ± 1.50	0.02446 ± 0.30	*0.67*	*200.3*	0.1276 ± 1.32
LG11-1.1_z01_BDS[1]	*12*	*BDS*[a]	*No*	$- \pm -$	*1.0*	*0.3*	$- \pm -$	$- \pm -$	—	*5015.4*	0.2769 ± 0.09
MC11-3.z01_BDS	*10*	*BDS*[a]	*No*	964.00 ± 6.80	*1.1*	*0.1*	3.9338 ± 0.72	0.16130 ± 0.71	*0.99*	*14365.3*	0.1769 ± 0.09
MC11-3.z02_BDS	*10*	*BDS*[a]	*No*	652.91 ± 1.25	*1.2*	*0.1*	1.9754 ± 0.23	0.10659 ± 0.19	*0.90*	*4594.2*	0.1344 ± 0.10
MC11-3.z03_BDS	*10*	*BDS*[a]	*No*	116.88 ± 0.34	*0.9*	*0.1*	0.1868 ± 1.34	0.01830 ± 0.29	*0.48*	*419.7*	0.0740 ± 1.22
MC11-3.z04_BDS	*10*	*BDS*[a]	*No*	65.52 ± 0.13	*0.9*	*0.3*	0.0638 ± 2.44	0.01021 ± 0.19	*0.58*	*312.2*	0.0453 ± 2.34
MC11-3.z05_BDS	*10*	*BDS*[a]	*No*	268.91 ± 0.73	*1.3*	*0.2*	1.0231 ± 0.31	0.04260 ± 0.27	*0.92*	*1900.9*	0.1742 ± 0.13
MC11-3.z06_BDS	*10*	*BDS*[a]	*No*	86.45 ± 0.22	*0.8*	*0.2*	0.1541 ± 1.73	0.01350 ± 0.25	*0.62*	*266.9*	0.0828 ± 1.58
MC11-3.z07_BDS	10	BDS[a]	No	65.91 ± 0.19	0.9	0.3	0.0676 ± 3.32	0.01028 ± 0.29	0.56	242.2	0.0477 ± 3.17
MC11-3.z08_BDS	*10*	*BDS*[a]	*No*	582.47 ± 1.00	*1.3*	*0.1*	1.3055 ± 0.25	0.09456 ± 0.17	*0.80*	*2631.7*	0.1001 ± 0.15
MC11-3.z09_BDS	10	BDS[a]	No	66.01 ± 0.26	0.9	0.3	0.0671 ± 0.96	0.01029 ± 0.39	0.49	972.4	0.0473 ± 0.84
MC11-3.z10_BDS	10	BDS[a]	No	65.87 ± 0.14	0.8	0.3	0.0672 ± 0.88	0.01027 ± 0.21	0.39	899.9	0.0475 ± 0.82
MC11-3.z11_BDS	*10*	*BDS*[a]	*No*	304.27 ± 0.90	*1.1*	*0.2*	0.6078 ± 0.47	0.04833 ± 0.30	*0.68*	*2669.2*	0.0912 ± 0.34
MC11-3 z12	*10*	*BDS*[b]	*Yes*	78.69 ± 0.16	*2.9*	*0.2*	0.1003 ± 1.89	0.01228 ± 0.21	*0.57*	*291.9*	0.0592 ± 1.78
MC11-3 z13	10	BDS[b]	Yes	65.69 ± 0.18	1.1	0.1	0.0655 ± 4.24	0.01024 ± 0.27	0.62	191.5	0.0464 ± 4.08
MC11-3 z18	10	BDS[b]	Yes	65.90 ± 0.29	1.3	0.2	0.0643 ± 5.93	0.01028 ± 0.44	0.61	144.1	0.0454 ± 5.67

Table A.5: Data from a Lofgren Section Z Coal tephra (LG11-1) and the Lofgren Section X Coal tephra (MC11-3). [1] no U data collected; $^{207}Pb^{206}Pb$ age is 3.345 ± 0.0015 Ga.

Sample	CA time (h)	Spk	U-Pb sep.	$\frac{^{206}Pb}{^{238}U}$ (Ma)	Pb_c (pg)	$\frac{Th}{U}$	$\frac{^{207}Pb}{^{235}U}$ (%2σ)	$\frac{^{206}Pb}{^{238}U}$ (%2σ)	ρ	$\frac{^{206}Pb}{^{204}Pb}$	$\frac{^{207}Pb}{^{206}Pb}$ (%2σ)
MK12-1.1 cz01	*6*	*BDS*[b]	*Yes*	580.23 ± 1.34	*2.3*	*0.4*	2.6939 ± 0.26	0.09418 ± 0.24	*0.94*	*11928.3*	0.2074 ± 0.09
MK12-1.1 cz02	6	BDS[b]	Yes	65.75 ± 0.13	1.9	0.5	0.0667 ± 1.45	0.01025 ± 0.20	0.58	525.0	0.0472 ± 1.34
MK12-1.1 cz03	6	BDS[b]	Yes	65.82 ± 0.10	2.0	0.4	0.0671 ± 1.29	0.01026 ± 0.15	0.49	561.8	0.0474 ± 1.22
MK12-1.1 cz04	6	BDS[b]	Yes	65.81 ± 0.10	3.0	0.1	0.0673 ± 0.71	0.01026 ± 0.15	0.27	1207.8	0.0475 ± 0.69
MK12-1.1 cz05	6	BDS[b]	Yes	65.72 ± 0.14	2.0	0.1	0.0667 ± 0.97	0.01025 ± 0.22	0.39	754.9	0.0472 ± 0.90
MK12-1.1 cz06	6	BDS[b]	Yes	65.89 ± 0.22	1.9	0.6	0.0673 ± 1.55	0.01027 ± 0.34	0.51	450.1	0.0475 ± 1.41
MK12-1.1 cz07	6	BDS[b]	Yes	65.76 ± 0.11	1.2	0.4	0.0669 ± 0.82	0.01025 ± 0.17	0.41	864.6	0.0473 ± 0.77
MK12-1.1 cz08	6	BDS[b]	Yes	65.67 ± 0.11	1.3	0.4	0.0666 ± 0.86	0.01024 ± 0.17	0.39	894.7	0.0472 ± 0.80
MK12-1.1 cz09	6	BDS[b]	Yes	65.90 ± 0.11	2.5	0.5	0.0671 ± 1.87	0.01028 ± 0.17	0.52	350.9	0.0473 ± 1.78
MK12-1.1 cz10	6	BDS[b]	Yes	65.90 ± 0.20	2.9	0.5	0.0675 ± 2.32	0.01028 ± 0.31	0.46	300.1	0.0477 ± 2.20
MK12-1.1 cz11	6	BDS[b]	Yes	65.73 ± 0.13	3.5	0.1	0.0669 ± 0.78	0.01025 ± 0.19	0.45	918.8	0.0474 ± 0.71
MK12-1.1 cz12	6	BDS[b]	Yes	65.81 ± 0.12	1.7	0.1	0.0674 ± 1.01	0.01026 ± 0.18	0.42	922.2	0.0477 ± 0.95
MK12-1.1 cz13	*6*	*BDS*[b]	*Yes*	79.24 ± 0.10	*2.0*	*0.1*	0.1065 ± 0.44	0.01237 ± 0.13	*0.39*	*1165.1*	0.0624 ± 0.40
MK12-1.1 cz14	6	BDS[b]	Yes	65.72 ± 0.15	2.1	0.5	0.0671 ± 1.49	0.01025 ± 0.22	0.44	501.3	0.0475 ± 1.40
MK12-1.1 cz15	6	BDS[b]	Yes	65.81 ± 0.17	6.8	0.1	0.0673 ± 1.57	0.01026 ± 0.26	0.40	429.7	0.0476 ± 1.49
MK12-1.1 cz17	6	BDS[b]	Yes	65.71 ± 0.19	1.5	0.1	0.0671 ± 0.78	0.01025 ± 0.29	0.38	1119.6	0.0475 ± 0.72
MK12-1.1 cz18	*6*	*BDS*[b]	*Yes*	482.39 ± 1.37	*2.0*	*1.2*	2.0981 ± 0.33	0.07770 ± 0.29	*0.96*	*5445.8*	0.1958 ± 0.09

Table A.6: Data from a McKeever Ranch Y Coal tephra (MK12-1).

Sample	CA time (h)	Spk	U-Pb sep.	$\frac{^{206}Pb}{^{238}U}$ (Ma)	Pb_c (pg)	$\frac{Th}{U}$	$\frac{^{207}Pb}{^{235}U}$ (%2σ)	$\frac{^{206}Pb}{^{238}U}$ (%2σ)	ρ	$\frac{^{206}Pb}{^{204}Pb}$	$\frac{^{207}Pb}{^{206}Pb}$ (%2σ)
SS11-3z01_BDS	*9*	*BDS*[a]	*No*	1970.51 ± 6.38	*1.4*	*1.5*	9.5989 ± 0.37	0.35754 ± 0.32	*0.90*	*1052.9*	0.1948 ± 0.16
SS11-3z03_BDS	*9*	*BDS*[a]	*No*	799.15 ± 2.00	*1.3*	*0.5*	1.8810 ± 1.19	0.13198 ± 0.25	*0.58*	*282.8*	0.1034 ± 1.06
SS11-3z04_BDS	9	BDS[a]	No	64.47 ± 0.31	1.1	0.6	0.0584 ± 8.78	0.01005 ± 0.48	0.73	108.9	0.0422 ± 8.43
SS11-3_z02_BDS	9	BDS[a]	No	64.78 ± 0.51	1.8	0.6	0.0611 ± 15.34	0.01010 ± 0.79	0.77	62.0	0.0438 ± 14.74
SS11-1.1 z01	*12*	*BDS*[b]	*No*	133.55 ± 0.26	*0.6*	*0.3*	0.2263 ± 0.27	0.02093 ± 0.20	*0.79*	*3259.0*	0.0784 ± 0.17
SS11-1.1 z02	12	BDS[b]	No	64.95 ± 0.16	1.0	0.5	0.0650 ± 3.66	0.01013 ± 0.25	0.68	200.6	0.0465 ± 3.49
SS11-1.1 z03	*12*	*BDS*[b]	*No*	159.23 ± 0.20	*1.8*	*0.4*	0.3153 ± 0.27	0.02501 ± 0.13	*0.58*	*1382.7*	0.0914 ± 0.22
SS11-1.1 z04	*12*	*BDS*[b]	*No*	65.98 ± 0.59	*2.8*	*0.4*	0.0658 ± 15.93	0.01029 ± 0.90	*0.78*	*59.1*	0.0464 ± 15.24
SS11-1.1 z05	*12*	*BDS*[b]	*No*	797.89 ± 1.06	*1.1*	*0.2*	2.4100 ± 0.16	0.13176 ± 0.14	*0.93*	*6539.7*	0.1327 ± 0.06
SS11-1.1 z06	*12*	*BDS*[b]	*No*	1309.77 ± 3.48	*18.7*	*0.2*	3.5756 ± 0.49	0.22529 ± 0.29	*0.70*	*663.1*	0.1151 ± 0.35
SS11-1.1 z07	*12*	*BDS*[b]	*No*	2199.57 ± 3.04	*2.8*	*0.4*	13.2484 ± 0.20	0.40665 ± 0.16	*0.91*	*2169.4*	0.2363 ± 0.08
SS11-1.1 z08	12	BDS[b]	No	65.05 ± 0.22	2.4	0.5	0.0653 ± 3.14	0.01014 ± 0.34	0.47	220.5	0.0467 ± 3.00
SS11-1.1 z09	*12*	*BDS*[b]	*No*	246.59 ± 0.31	*0.8*	*0.3*	0.4925 ± 0.37	0.03899 ± 0.13	*0.47*	*1099.6*	0.0916 ± 0.33
GC12-3.1 cz01	*8*	*BDS*[b]	*Yes*	405.99 ± 0.46	*1.4*	*0.2*	1.2657 ± 0.23	0.06500 ± 0.12	*0.64*	*3043.8*	0.1412 ± 0.17
GC12-3.1 cz02	8	BDS[b]	Yes	65.77 ± 0.16	2.6	0.1	0.0671 ± 1.59	0.01026 ± 0.24	0.47	480.4	0.0474 ± 1.49
GC12-3.1 cz03	*8*	*BDS*[b]	*Yes*	702.52 ± 1.10	*1.8*	*0.9*	2.6869 ± 0.21	0.11514 ± 0.16	*0.90*	*4144.7*	0.1693 ± 0.09
GC12-3.1 cz05	*8*	*BDS*[b]	*Yes*	659.10 ± 1.09	*1.7*	*0.2*	2.5381 ± 0.19	0.10765 ± 0.17	*0.94*	*4876.1*	0.1710 ± 0.07
GC12-3.1 cz06	*8*	*BDS*[b]	*Yes*	66.33 ± 0.12	*2.0*	*0.0*	0.0718 ± 1.01	0.01034 ± 0.18	*0.36*	*648.6*	0.0504 ± 0.95
GC12-3.1 cz07	*8*	*BDS*[b]	*Yes*	290.02 ± 0.57	*3.0*	*0.9*	0.9114 ± 0.49	0.04602 ± 0.20	*0.75*	*651.6*	0.1436 ± 0.36
GC12-3.1 cz08	*8*	*BDS*[b]	*Yes*	509.36 ± 1.01	*1.4*	*0.3*	1.1791 ± 0.21	0.08222 ± 0.21	*0.91*	*6975.0*	0.1040 ± 0.08
GC12-3.1 cz09	*8*	*BDS*[b]	*Yes*	681.67 ± 1.21	*2.2*	*0.4*	3.0139 ± 0.20	0.11154 ± 0.19	*0.93*	*5586.1*	0.1960 ± 0.07
GC12-3.1 cz10	8	BDS[b]	Yes	65.74 ± 0.15	1.4	0.1	0.0671 ± 1.36	0.01025 ± 0.23	0.39	626.1	0.0475 ± 1.29
GC12-3.1 cz11	*8*	*BDS*[b]	*Yes*	94.53 ± 0.11	*1.5*	*0.2*	0.1347 ± 0.59	0.01477 ± 0.11	*0.40*	*850.6*	0.0661 ± 0.55

Table A.7: Data from two Saddle Section W Coal tephras and a Garbani Channel Y coal tephra (GC12-3). One W coal tephra (SS11-3) occurs at the top of the upper of the two W Coal lignites, the other (SS11-1) occurs near the bottom of the lower W Coal lignite.

Appendix B

Data tables for Chapter 4

Sample	CA time (h)	Spk	U-Pb sep.	$^{206}Pb/^{238}U$ (Ma)	Pb_c (pg)	$\frac{Th}{U}$	$^{207}Pb/^{235}U$ (%2σ)	$^{206}Pb/^{238}U$ (%2σ)	ρ	$^{206}Pb/^{204}Pb$	$^{207}Pb/^{206}Pb$ (%2σ)
OCH11-1.2-z02_BDS	12	BDS[a]	No	253.02 ± 1.65	1.4	0.9	0.2884 ± 4.04	0.04003 ± 0.65	0.42	159.3	0.0523 ± 3.81
OCH11-1.2-z03_BDS	8	BDS[a]	No	251.62 ± 0.63	0.8	0.4	0.2817 ± 0.36	0.03980 ± 0.25	0.75	3447.1	0.0513 ± 0.24
OCH11-1.2-z04_BDS	8	BDS[a]	No	252.39 ± 0.60	1.5	0.4	0.2851 ± 0.76	0.03993 ± 0.24	0.43	1036.5	0.0518 ± 0.69
OCH11-1.2-z05_BDS	8	BDS[a]	No	252.58 ± 0.55	0.9	1.0	0.2839 ± 0.64	0.03996 ± 0.22	0.45	1289.3	0.0515 ± 0.57
OCH11-1.2-z06_BDS	8	BDS[a]	No	252.03 ± 0.56	1.3	0.8	0.2795 ± 1.14	0.03987 ± 0.22	0.41	678.7	0.0508 ± 1.07
OCH11-1.2-z07_BDS	8	BDS[a]	No	252.51 ± 0.44	1.1	0.4	0.2835 ± 0.78	0.03995 ± 0.17	0.40	974.3	0.0515 ± 0.73
OCH11-1.2-z08_BDS	8	BDS[a]	No	251.96 ± 0.55	1.1	0.7	0.2798 ± 1.09	0.03986 ± 0.22	0.41	650.6	0.0509 ± 1.02
OCH11-1.2-z09_BDS	8	BDS[a]	No	251.49 ± 0.45	1.6	0.5	0.2819 ± 0.71	0.03978 ± 0.18	0.41	872.7	0.0514 ± 0.66
OCH11-1.2-z10_BDS	8	BDS[a]	No	251.61 ± 0.59	1.8	0.4	0.2784 ± 1.96	0.03980 ± 0.24	0.46	317.7	0.0507 ± 1.86
OCH11-1.2-z11_BDS	*8*	*BDS[a]*	*No*	253.20 ± 0.46	*1.3*	*0.4*	0.2894 ± 1.58	0.04006 ± 0.18	*0.49*	*403.7*	0.0524 ± 1.50
OCH11-1.2-z12_BDS	8	BDS[a]	No	251.53 ± 0.41	1.5	0.4	0.2804 ± 1.31	0.03979 ± 0.16	0.47	490.8	0.0511 ± 1.24
OCH11-1.1-z03_BDS	12	BDS[a]	No	251.92 ± 0.95	1.2	0.9	0.2812 ± 5.39	0.03985 ± 0.38	0.69	133.2	0.0512 ± 5.13
OCH11-1.1-z04_BDS	*12*	*BDS[a]*	*No*	254.92 ± 0.71	*0.8*	*0.8*	0.2875 ± 3.12	0.04034 ± 0.28	*0.58*	*230.4*	0.0517 ± 2.97
OCH11-1.1-z05_BDS	12	BDS[a]	No	252.88 ± 0.93	1.5	0.8	0.2922 ± 5.22	0.04001 ± 0.37	0.70	129.2	0.0530 ± 4.97
OCH11-3.z01_BDS	*12*	*BDS[a]*	*No*	254.33 ± 0.84	*2.6*	*0.8*	0.2771 ± 3.68	0.04024 ± 0.33	*0.56*	*199.7*	0.0499 ± 3.51
OCH11-3.z02_BDS	12	BDS[a]	No	251.55 ± 0.54	1.1	0.7	0.2817 ± 2.42	0.03979 ± 0.22	0.59	290.2	0.0513 ± 2.30
OCH11-3.2-z01_BDS	12	BDS[a]	No	252.34 ± 0.99	1.0	0.8	0.2829 ± 0.71	0.03992 ± 0.39	0.61	1367.5	0.0514 ± 0.56
OCH11-3.2-z02_BDS	12	BDS[a]	No	251.93 ± 0.68	1.2	0.4	0.2819 ± 0.88	0.03985 ± 0.27	0.43	819.6	0.0513 ± 0.80
OCH11-3.2-z03_BDS	*12*	*BDS[a]*	*No*	638.03 ± 1.14	*0.9*	*0.4*	1.1402 ± 0.29	0.10404 ± 0.18	*0.71*	*3082.9*	0.0795 ± 0.20
OCH11-3.2-z04_BDS	*12*	*BDS[a]*	*No*	252.70 ± 0.57	*1.1*	*0.4*	0.2895 ± 2.41	0.03998 ± 0.22	*0.56*	*264.7*	0.0525 ± 2.29
OCH11-3.2-z05_BDS	*12*	*BDS[a]*	*No*	1295.51 ± 4.72	*0.9*	*0.7*	3.0424 ± 0.72	0.22258 ± 0.36	*0.62*	*581.4*	0.0991 ± 0.57
OCH11-3.2-z06_BDS	12	BDS[a]	No	252.14 ± 0.75	1.1	0.6	0.2791 ± 3.20	0.03989 ± 0.30	0.56	222.5	0.0507 ± 3.05
OCH11-3.2-z07_BDS	*12*	*BDS[a]*	*No*	252.88 ± 0.81	*1.0*	*0.6*	0.2881 ± 1.80	0.04001 ± 0.32	*0.42*	*418.4*	0.0522 ± 1.69
OCH11-3.2-z08_BDS	*12*	*BDS[a]*	*No*	1201.10 ± 5.34	*1.1*	*0.7*	2.7702 ± 1.71	0.20481 ± 0.44	*0.54*	*224.3*	0.0981 ± 1.52
OCH11-3.3 z02	*12*	*BDS[a]*	*No*	265.18 ± 0.96	*2.3*	*0.4*	0.2946 ± 3.85	0.04199 ± 0.36	*0.60*	*223.0*	0.0509 ± 3.65
OCH11-3.3 z03	12	BDS[a]	No	250.89 ± 0.64	1.1	0.4	0.2833 ± 3.67	0.03969 ± 0.26	0.71	187.7	0.0518 ± 3.49
OCH11-3.3 z04	12	BDS[b]	No	252.00 ± 0.48	0.9	0.5	0.2819 ± 2.02	0.03987 ± 0.19	0.55	321.3	0.0513 ± 1.92
OCH12-13.1_z01_BDS	10	BDS[a]	No	395.49 ± 0.99	1.2	0.2	0.4743 ± 0.46	0.06327 ± 0.25	0.61	1803.4	0.0544 ± 0.37
OCH12-13.1_z02_BDS	10	BDS[a]	No	315.58 ± 0.85	1.0	0.8	0.3519 ± 1.33	0.05017 ± 0.27	0.40	729.9	0.0509 ± 1.25
OCH12-13.1_z03_BDS	10	BDS[a]	No	529.65 ± 1.28	1.7	0.2	0.6826 ± 0.65	0.08563 ± 0.24	0.48	1003.9	0.0578 ± 0.58
OCH12-13.1_z04_BDS	10	BDS[a]	No	287.23 ± 0.60	1.9	0.7	0.3261 ± 0.72	0.04556 ± 0.21	0.43	868.3	0.0519 ± 0.66
OCH12-13.1_z05_BDS	10	BDS[a]	No	286.14 ± 0.44	1.1	1.3	0.3253 ± 0.56	0.04539 ± 0.15	0.43	1234.1	0.0520 ± 0.51
OCH12-13.1_z06_BDS	10	BDS[a]	No	1417.87 ± 3.64	0.9	0.9	3.0545 ± 0.34	0.24601 ± 0.26	0.80	3614.3	0.0900 ± 0.21
OCH12-13.1_z07_BDS	10	BDS[a]	No	1250.93 ± 2.96	1.0	1.6	2.4205 ± 0.72	0.21416 ± 0.24	0.51	593.5	0.0820 ± 0.64
OCH12-13.1_z08_BDS	10	BDS[a]	No	483.53 ± 1.11	1.0	0.4	0.6121 ± 1.06	0.07789 ± 0.23	0.42	608.1	0.0570 ± 0.98
OCH12-13.1 z09	10	BDS[b]	No	244.47 ± 0.66	0.6	0.6	0.2709 ± 2.06	0.03865 ± 0.27	0.51	440.7	0.0508 ± 1.93
OCH12-13.1_z10_BDS	10	BDS[a]	No	1697.17 ± 4.68	1.5	0.4	3.4053 ± 0.53	0.30118 ± 0.28	0.60	1272.8	0.0820 ± 0.43
OCH12-13.1 z11	10	BDS[b]	No	306.37 ± 1.04	1.2	0.9	0.3520 ± 0.94	0.04867 ± 0.35	0.52	729.0	0.0524 ± 0.82

Table B.1: Data from the Lower (OCH11-1) and Upper (OCH11-3) Caprock tephra, as well as the detrital zircons (OCH12-13). For a detailed description of the columns and notations, see Table B.2.

Sample	CA time (h)	Spk	U-Pb sep.	$\frac{^{206}Pb}{^{238}U}$ (Ma)	Pb_c (pg)	$\frac{Th}{U}$	$\frac{^{207}Pb}{^{235}U}$ (%2σ)	$\frac{^{206}Pb}{^{238}U}$ (%2σ)	ρ	$\frac{^{206}Pb}{^{204}Pb}$	$\frac{^{207}Pb}{^{206}Pb}$ (%2σ)
OCH11-5.z01_BDS	12	BDS[a]	No	251.52 ± 0.82	1.1	1.2	0.2824 ± 3.05	0.03979 ± 0.33	0.53	242.6	0.0515 ± 2.89
OCH11-5.z03_BDS	12	BDS[a]	No	253.61 ± 2.12	1.4	1.0	0.2939 ± 13.22	0.04013 ± 0.84	0.77	61.0	0.0531 ± 12.59
OCH11-5.z04_BDS	12	BDS[a]	No	251.89 ± 1.92	1.4	1.4	0.2672 ± 12.45	0.03985 ± 0.76	0.74	71.8	0.0486 ± 11.90
OCH11-5.z05_BDS	12	BDS[a]	No	252.45 ± 0.98	1.7	1.0	0.2881 ± 5.17	0.03994 ± 0.39	0.65	137.7	0.0523 ± 4.93
OCH11-5.z07_BDS	12	BDS[a]	No	251.55 ± 0.78	1.1	1.1	0.2779 ± 3.63	0.03979 ± 0.31	0.58	186.9	0.0507 ± 3.45
OCH11-5.z08_BDS	12	BDS[a]	No	251.84 ± 0.54	1.4	1.7	0.2853 ± 2.34	0.03984 ± 0.21	0.56	274.8	0.0519 ± 2.23
OCH11-5.z09_BDS	12	BDS[a]	No	252.19 ± 0.75	1.0	1.2	0.2796 ± 2.45	0.03990 ± 0.30	0.47	281.7	0.0508 ± 2.32
OCH11-5.z10_BDS	12	BDS[a]	No	252.15 ± 1.51	1.3	1.2	0.2881 ± 4.45	0.03989 ± 0.60	0.50	222.4	0.0524 ± 4.19

Table B.2: Data from the Clarendon section. *CA Time* is the leaching time for chemical abrasion. *Spk* is the spike used for the analysis; [a] denotes samples corrected for mass fractionation using an average value for analyses of NBS 981, while [b] denotes cycle-by-cycle corrections from the $^{202}Pb/^{205}Pb$ ratio. *U-Pb sep.* indicates whether anion exchange chemistry was used. Pb_c is common Pb including analytical blank (blank composition is found in Table 2.1). *Th/U* ratio is the present-day Th/U ratio calculated from radiogenic $^{208}Pb/^{206}Pb$ and the $^{206}Pb/^{238}U$ age, assuming a Th/U of 4 for the crystallizing magma. The $^{206}Pb/^{204}Pb$ ratio is corrected for tracer contribution and mass fractionation. Other isotopic ratios are corrected for mass fractionation, tracer contribution, and common lead contribution. ρ is the correlation coefficient of radiogenic $^{207}Pb/^{235}U$ with $^{206}Pb/^{238}U$. Uncertainties are given at 2σ and do not include tracer calibration (0.1%) or decay constant (0.054%) uncertainties. Data excluded from weighted means are italicized and in red.

Sample	CA time (h)	Spk	U-Pb sep.	$^{206}Pb/^{238}U$ (Ma)	Pb_c (pg)	$\frac{Th}{U}$	$^{207}Pb/^{235}U$ (%2σ)	$^{206}Pb/^{238}U$ (%2σ)	ρ	$^{206}Pb/^{204}Pb$	$^{207}Pb/^{206}Pb$ (%2σ)
OCH12-2-z01_BDS	12	BDS[a]	No	251.30 ± 0.88	2.6	0.8	0.2821 ± 2.70	0.03975 ± 0.35	0.46	233.9	0.0515 ± 2.56
OCH12-2-z02_BDS	*12*	*BDS[a]*	*No*	254.43 ± 0.89	*1.1*	*0.7*	0.2931 ± 4.63	0.04026 ± 0.35	*0.66*	*146.7*	0.0528 ± 4.40
OCH12-2-z03_BDS	8	BDS[a]	No	252.76 ± 0.58	1.1	0.4	0.2791 ± 1.27	0.03999 ± 0.23	0.41	519.3	0.0506 ± 1.19
OCH12-2-z04_BDS	8	BDS[a]	No	251.48 ± 1.23	1.1	0.9	0.2841 ± 7.41	0.03978 ± 0.49	0.74	103.0	0.0518 ± 7.06
OCH12-2-z05_BDS	*8*	*BDS[a]*	*No*	254.96 ± 2.02	*1.1*	*0.9*	0.2789 ± 6.45	0.04034 ± 0.79	*0.51*	*205.8*	0.0501 ± 6.08
OCH12-2-z06_BDS	8	BDS[a]	No	252.11 ± 0.87	1.0	0.3	0.2804 ± 4.56	0.03988 ± 0.35	0.65	159.8	0.0510 ± 4.34
OCH12-2-z07_BDS	8	BDS[a]	No	249.85 ± 1.67	1.2	0.6	0.2619 ± 10.93	0.03952 ± 0.67	0.76	84.8	0.0481 ± 10.44
OCH12-2-z08_BDS	8	BDS[a]	No	251.65 ± 0.64	1.1	0.8	0.2805 ± 3.41	0.03981 ± 0.25	0.66	197.6	0.0511 ± 3.25
OCH12-2.3 z01	12	BDS[b]	No	251.93 ± 0.29	0.5	0.7	0.2807 ± 0.79	0.03985 ± 0.12	0.34	922.4	0.0511 ± 0.76
OCH12-2.3 z02	12	BDS[b]	No	251.50 ± 0.42	0.6	0.8	0.2827 ± 1.61	0.03978 ± 0.17	0.57	466.0	0.0515 ± 1.52
OCH12-2.3 z03	12	BDS[b]	No	250.48 ± 1.03	0.7	0.9	0.2808 ± 1.68	0.03962 ± 0.42	0.51	594.2	0.0514 ± 1.51
OCH12-3.z01_BDS	8	BDS[a]	No	251.39 ± 2.90	2.5	1.0	0.2735 ± 19.93	0.03977 ± 1.15	0.77	47.5	0.0499 ± 19.05
OCH12-3.2_z01_BDS	*8*	*BDS[a]*	*No*	252.55 ± 0.41	*0.8*	*0.4*	0.2823 ± 0.60	0.03995 ± 0.16	*0.43*	*1226.4*	0.0512 ± 0.55
OCH12-3.2_z02_BDS	*8*	*BDS[a]*	*No*	252.43 ± 0.38	*0.8*	*0.6*	0.2886 ± 1.12	0.03993 ± 0.15	*0.45*	*580.9*	0.0524 ± 1.06
OCH12-3.2_z03_BDS	8	BDS[a]	No	251.69 ± 0.48	0.9	0.8	0.2815 ± 1.36	0.03982 ± 0.19	0.44	500.0	0.0513 ± 1.28
OCH12-3.2_z04_BDS	*8*	*BDS[a]*	*No*	252.71 ± 0.40	*1.1*	*0.5*	0.2836 ± 0.95	0.03998 ± 0.16	*0.42*	*679.5*	0.0515 ± 0.89
OCH12-3.2_z05_BDS	8	BDS[a]	No	251.81 ± 0.41	0.7	0.5	0.2819 ± 0.62	0.03983 ± 0.16	0.41	1160.5	0.0513 ± 0.58
OCH12-3.2_z06_BDS	8	BDS[a]	No	251.54 ± 0.42	0.8	0.5	0.2822 ± 0.61	0.03979 ± 0.17	0.42	1208.4	0.0514 ± 0.57
OCH12-3.2_z07_BDS	8	BDS[a]	No	251.97 ± 0.60	0.9	0.5	0.2820 ± 1.33	0.03986 ± 0.24	0.42	489.4	0.0513 ± 1.26
OCH12-3.2_z08_BDS	8	BDS[a]	No	251.60 ± 0.56	1.0	0.4	0.2834 ± 2.67	0.03980 ± 0.22	0.61	244.0	0.0516 ± 2.54
OCH12-3.2_z09_BDS	8	BDS[a]	No	251.36 ± 0.45	0.6	0.4	0.2753 ± 1.36	0.03976 ± 0.18	0.45	542.8	0.0502 ± 1.29
OCH12-3.2_z11_BDS	8	BDS[a]	No	251.10 ± 0.46	0.5	0.7	0.2748 ± 1.84	0.03972 ± 0.18	0.53	384.6	0.0502 ± 1.75
OCH12-3.2_z12_BDS	8	BDS[a]	No	251.16 ± 0.60	1.2	0.4	0.2857 ± 1.39	0.03973 ± 0.24	0.41	526.5	0.0522 ± 1.31
OCH12-3.2_z13_BDS	*8*	*BDS[a]*	*No*	252.15 ± 0.34	*0.6*	*0.4*	0.2833 ± 0.55	0.03989 ± 0.13	*0.42*	*1324.3*	0.0515 ± 0.50
OCH12-3.2_z14_BDS	8	BDS[a]	No	251.62 ± 0.43	0.8	0.5	0.2810 ± 1.02	0.03980 ± 0.17	0.42	867.6	0.0512 ± 0.96

Table B.3: Data from the Lower (OCH12-2) and Upper (OCH12-3) Dickens tephra.

Sample	CA time (h)	Spk	U-Pb sep.	$\frac{^{206}Pb}{^{238}U}$ (Ma)	Pb_c (pg)	$\frac{Th}{U}$	$\frac{^{207}Pb}{^{235}U}$ (%2σ)	$\frac{^{206}Pb}{^{238}U}$ (%2σ)	ρ	$\frac{^{206}Pb}{^{204}Pb}$	$\frac{^{207}Pb}{^{206}Pb}$ (%2σ)
OCH11-4.z01_BDS	12	BDS[a]	No	252.28 ± 1.26	1.4	1.1	0.2882 ± 7.05	0.03991 ± 0.50	0.72	110.1	0.0524 ± 6.70
OCH11-4.z03_BDS	12	BDS[a]	No	251.76 ± 1.72	1.3	1.3	0.2828 ± 10.75	0.03983 ± 0.68	0.74	75.1	0.0515 ± 10.26
OCH11-4.z04_BDS	12	BDS[a]	No	250.91 ± 1.44	1.1	1.2	0.2573 ± 8.69	0.03969 ± 0.57	0.70	103.2	0.0470 ± 8.29
OCH11-4.z05_BDS	12	BDS[a]	No	251.51 ± 0.91	1.4	1.1	0.2880 ± 4.79	0.03979 ± 0.36	0.67	151.2	0.0525 ± 4.56
OCH11-4.z07_BDS	12	BDS[a]	No	251.29 ± 1.89	1.0	0.9	0.2821 ± 11.40	0.03975 ± 0.75	0.73	71.4	0.0515 ± 10.87
OCH11-4.z08_BDS	*12*	*BDS[a]*	*No*	253.88 ± 1.32	*0.9*	*1.8*	0.2902 ± 6.50	0.04017 ± 0.52	*0.62*	*116.6*	0.0524 ± 6.20
OCH11-4.z09_BDS	12	BDS[a]	No	252.46 ± 1.31	0.8	1.4	0.2926 ± 7.60	0.03994 ± 0.52	0.73	102.4	0.0531 ± 7.22
OCH11-4.z10_BDS	12	BDS[a]	No	250.25 ± 0.89	0.9	1.3	0.2851 ± 4.97	0.03958 ± 0.36	0.69	134.7	0.0522 ± 4.73
OCH11-4.z11_BDS	12	BDS[a]	No	251.45 ± 0.86	2.3	1.5	0.2799 ± 4.06	0.03978 ± 0.34	0.59	161.2	0.0510 ± 3.87
OCH11-4.z12_BDS	*12*	*BDS[a]*	*No*	253.29 ± 1.67	*1.4*	*1.3*	0.2978 ± 4.65	0.04007 ± 0.66	*0.46*	*144.4*	0.0539 ± 4.39
OCH11-4.z13_BDS	12	BDS[a]	No	250.62 ± 0.95	1.4	1.1	0.2756 ± 4.02	0.03964 ± 0.38	0.54	172.1	0.0504 ± 3.83
OCH11-4.z14_BDS	*12*	*BDS[a]*	*No*	254.00 ± 2.34	*2.0*	*1.0*	0.2847 ± 8.22	0.04019 ± 0.92	*0.51*	*103.3*	0.0514 ± 7.79
OCH11-4.z15_BDS	12	BDS[a]	No	252.31 ± 0.78	1.5	1.5	0.2838 ± 3.86	0.03992 ± 0.31	0.62	175.9	0.0516 ± 3.67
OCH11-4.z16_BDS	12	BDS[a]	No	250.64 ± 2.66	1.6	1.2	0.2515 ± 19.12	0.03965 ± 1.06	0.76	52.7	0.0460 ± 18.32
OCH11-4.2 cz01	8	BDS[b]	Yes	250.88 ± 1.41	9.9	1.3	0.2628 ± 9.66	0.03969 ± 0.57	0.74	82.4	0.0480 ± 9.25
OCH11-4.2 cz02	*8*	*BDS[b]*	*Yes*	253.67 ± 1.08	*2.7*	*1.1*	0.2898 ± 6.57	0.04013 ± 0.44	*0.69*	*108.5*	0.0524 ± 6.28
OCH11-4.2 cz03	8	BDS[b]	Yes	252.53 ± 0.74	2.1	1.1	0.2796 ± 3.87	0.03995 ± 0.30	0.63	198.5	0.0508 ± 3.69
OCH11-4.2 cz04	8	BDS[b]	Yes	252.27 ± 0.77	1.9	1.0	0.2694 ± 3.70	0.03991 ± 0.31	0.66	271.2	0.0490 ± 3.50
OCH11-4.2 cz05	*8*	*BDS[b]*	*Yes*	243.29 ± 5.75	*11.2*	*1.2*	0.2440 ± 45.23	0.03846 ± 2.41	*0.82*	*35.6*	0.0460 ± 43.28
OCH11-4.2 cz06	8	BDS[b]	Yes	252.77 ± 0.73	1.6	1.3	0.2886 ± 2.56	0.03999 ± 0.30	0.62	319.9	0.0523 ± 2.38
OCH11-4.2 cz07	8	BDS[b]	Yes	252.04 ± 1.11	1.4	1.0	0.2850 ± 1.77	0.03987 ± 0.45	0.42	609.8	0.0518 ± 1.63
OCH11-4.2 cz08	8	BDS[b]	Yes	251.99 ± 4.01	1.9	0.8	0.2634 ± 9.50	0.03986 ± 1.62	0.38	246.8	0.0479 ± 9.01
OCH11-4.2 cz10	8	BDS[b]	Yes	252.14 ± 0.51	1.3	1.0	0.2839 ± 2.15	0.03989 ± 0.21	0.41	400.4	0.0516 ± 2.07
OCH11-4.2 cz11	8	BDS[b]	Yes	251.13 ± 1.24	3.7	1.0	0.2789 ± 7.39	0.03973 ± 0.50	0.70	96.0	0.0509 ± 7.04
OCH11-4.2 cz12	8	BDS[b]	Yes	252.00 ± 1.02	1.1	1.0	0.2820 ± 3.02	0.03987 ± 0.41	0.74	368.2	0.0513 ± 2.73
OCH11-4.2 cz13	8	BDS[b]	Yes	251.33 ± 0.59	1.2	0.7	0.2821 ± 1.25	0.03976 ± 0.24	0.35	559.6	0.0515 ± 1.19
OCH11-4.2 cz14	*8*	*BDS[b]*	*Yes*	253.66 ± 0.85	*2.8*	*1.3*	0.2838 ± 4.88	0.04013 ± 0.34	*0.75*	*161.6*	0.0513 ± 4.63
OCH11-4.2 cz15	8	BDS[b]	Yes	251.12 ± 0.58	1.6	0.9	0.2794 ± 2.46	0.03972 ± 0.24	0.59	287.7	0.0510 ± 2.33
OCH11-4.2 cz16	8	BDS[b]	Yes	252.09 ± 0.44	1.6	1.0	0.2821 ± 1.51	0.03988 ± 0.18	0.49	439.7	0.0513 ± 1.43
OCH11-4.2 cz18	*8*	*BDS[b]*	*Yes*	255.09 ± 3.92	*13.4*	*1.2*	0.2854 ± 26.16	0.04036 ± 1.57	*0.76*	*39.4*	0.0513 ± 24.99

Table B.4: Data from the Highway 207 tephra.

Sample	CA time (h)	Spk	U-Pb sep.	$\frac{^{206}Pb}{^{238}U}$ (Ma)	Pb_c (pg)	$\frac{Th}{U}$	$\frac{^{207}Pb}{^{235}U}$ (%2σ)	$\frac{^{206}Pb}{^{238}U}$ (%2σ)	ρ	$\frac{^{206}Pb}{^{204}Pb}$	$\frac{^{207}Pb}{^{206}Pb}$ (%2σ)
OCH11-6.z07_BDS	12	BDS[a]	No	251.82 ± 1.58	0.7	1.2	0.2767 ± 2.44	0.03984 ± 0.63	0.42	411.4	0.0504 ± 2.25
OCH11-6.z08_BDS	12	BDS[a]	No	251.45 ± 1.01	0.7	0.8	0.2615 ± 2.72	0.03978 ± 0.40	0.43	314.5	0.0477 ± 2.57
OCH11-6.z09_BDS	*12*	*BDS[a]*	*No*	254.48 ± 1.37	*0.9*	*1.0*	0.2862 ± 3.40	0.04027 ± 0.54	*0.44*	*244.3*	0.0516 ± 3.20
OCH11-6.z10_BDS	12	BDS[a]	No	252.23 ± 0.53	1.2	1.1	0.2817 ± 2.03	0.03990 ± 0.21	0.52	319.3	0.0512 ± 1.93
OCH11-6.z11_BDS	12	BDS[a]	No	251.38 ± 0.92	0.9	1.1	0.2824 ± 4.84	0.03977 ± 0.37	0.65	141.7	0.0515 ± 4.60
OCH11-6.z12_BDS	12	BDS[a]	No	252.29 ± 1.33	0.9	1.0	0.2838 ± 1.03	0.03991 ± 0.53	0.57	1006.1	0.0516 ± 0.85
OCH11-6.z13_BDS	*12*	*BDS[a]*	*No*	253.88 ± 0.82	*1.2*	*1.2*	0.2859 ± 1.74	0.04017 ± 0.32	*0.41*	*395.1*	0.0516 ± 1.63
OCH11-6.z14_BDS	12	BDS[a]	No	251.08 ± 2.41	1.3	0.9	0.2765 ± 15.10	0.03972 ± 0.96	0.77	70.1	0.0505 ± 14.37
OCH11-6.z15_BDS	12	BDS[a]	No	252.90 ± 2.29	2.0	1.3	0.2819 ± 14.46	0.04001 ± 0.91	0.76	61.7	0.0511 ± 13.78
OCH11-6.z16_BDS	12	BDS[a]	No	250.67 ± 2.11	1.4	1.0	0.2563 ± 14.39	0.03965 ± 0.84	0.76	68.7	0.0469 ± 13.76
OCH11-6.z16_BDS	12	BDS[a]	No	251.81 ± 3.31	1.9	1.0	0.2684 ± 23.03	0.03984 ± 1.32	0.78	46.5	0.0489 ± 22.02
OCH11-6 cz01	12	BDS[b]	Yes	251.48 ± 0.54	1.0	1.0	0.2789 ± 1.01	0.03978 ± 0.22	0.33	737.1	0.0508 ± 0.96
OCH11-6 cz02	12	BDS[b]	Yes	251.75 ± 0.34	1.2	0.9	0.2805 ± 0.74	0.03982 ± 0.14	0.63	1038.3	0.0511 ± 0.66
OCH11-6 cz03	12	BDS[b]	Yes	250.86 ± 1.54	8.0	1.1	0.2605 ± 10.88	0.03968 ± 0.62	0.76	75.7	0.0476 ± 10.42
OCH11-6 cz04	12	BDS[b]	Yes	252.18 ± 0.78	0.9	1.0	0.2803 ± 0.85	0.03989 ± 0.32	0.66	1237.4	0.0510 ± 0.69
OCH11-6.1 mz01	6	BDS[b]	Yes	251.42 ± 1.86	4.3	0.9	0.2797 ± 1.22	0.03977 ± 0.76	0.74	1195.1	0.0510 ± 0.83
OCH11-6.1 mz02	6	BDS[b]	Yes	252.38 ± 0.61	3.4	0.9	0.2814 ± 0.92	0.03993 ± 0.25	0.42	703.5	0.0511 ± 0.85
OCH11-6.1 mz03	6	BDS[b]	Yes	252.14 ± 0.50	8.0	0.8	0.2808 ± 2.01	0.03989 ± 0.20	0.56	306.0	0.0511 ± 1.91
OCH11-6.1 mz04	*6*	*BDS[b]*	*Yes*	253.14 ± 0.66	*9.4*	*0.8*	0.2854 ± 2.83	0.04005 ± 0.27	*0.56*	*226.2*	0.0517 ± 2.69
OCH11-6.1 mz05	*6*	*BDS[b]*	*Yes*	326.07 ± 0.73	*1.5*	*0.6*	0.3817 ± 0.42	0.05188 ± 0.23	*0.65*	*2583.7*	0.0534 ± 0.32
OCH11-6.1 mz06	6	BDS[b]	Yes	251.65 ± 0.48	5.3	1.0	0.2818 ± 1.29	0.03981 ± 0.20	0.49	506.0	0.0513 ± 1.20
OCH11-6.1 mz07	*6*	*BDS[b]*	*Yes*	318.12 ± 0.43	*3.9*	*0.7*	0.3991 ± 0.24	0.05059 ± 0.14	*0.61*	*3114.8*	0.0572 ± 0.19
OCH11-6.1 mz08	6	BDS[b]	Yes	251.04 ± 0.54	7.1	1.1	0.2792 ± 0.96	0.03971 ± 0.22	0.39	671.6	0.0510 ± 0.89
OCH11-6.1 z01	6	BDS[b]	Yes	251.87 ± 0.70	2.5	1.2	0.2737 ± 1.98	0.03984 ± 0.28	0.56	479.4	0.0498 ± 1.84
OCH11-6.Z02	12	BW[a]	No	250.78 ± 2.42	1.3	1.2	0.2850 ± 14.62	0.03967 ± 0.97	0.84	94.3	0.0521 ± 13.82
OCH11-6.Z04	12	BW[a]	No	252.71 ± 0.97	1.6	0.9	0.2848 ± 4.07	0.03998 ± 0.38	0.62	361.7	0.0517 ± 3.85
OCH11-6.Z05	12	BW[a]	No	252.91 ± 1.38	1.4	1.3	0.2890 ± 7.69	0.04001 ± 0.55	0.78	157.9	0.0524 ± 7.27
OCH11-6.Z06	12	BW[a]	No	251.17 ± 2.99	1.5	1.4	0.2960 ± 18.13	0.03973 ± 1.19	0.87	77.9	0.0540 ± 17.11

Table B.5: Data from the Palo Duro (OCH11-6) tephra.

Sample	CA time (h)	Spk	U-Pb sep.	$\frac{^{206}Pb}{^{238}U}$ (Ma)	Pb_c (pg)	$\frac{Th}{U}$	$\frac{^{207}Pb}{^{235}U}$ (%2σ)	$\frac{^{206}Pb}{^{238}U}$ (%2σ)	ρ	$\frac{^{206}Pb}{^{204}Pb}$	$\frac{^{207}Pb}{^{206}Pb}$ (%2σ)
OCH12-7.z01_BDS	*12*	*BDS*[a]	*No*	255.80 ± 1.99	*1.3*	*1.2*	0.2906 ± 11.78	0.04048 ± 0.78	*0.79*	*83.8*	0.0521 ± 11.18
OCH12-7.z02_BDS	12	BDS[a]	No	249.46 ± 1.50	1.3	1.3	0.2498 ± 10.22	0.03946 ± 0.60	0.72	83.2	0.0459 ± 9.80
OCH12-7.z03_BDS	*12*	*BDS*[a]	*No*	253.70 ± 2.67	*0.7*	*1.3*	0.2941 ± 14.11	0.04014 ± 1.05	*0.70*	*63.7*	0.0531 ± 13.40
OCH12-7.z04_BDS	12	BDS[a]	No	252.06 ± 1.51	1.0	1.6	0.2629 ± 9.50	0.03987 ± 0.60	0.75	99.6	0.0478 ± 9.06
OCH12-7 cz01	12	BDS[b]	Yes	251.51 ± 0.56	1.3	1.2	0.2758 ± 3.40	0.03979 ± 0.23	0.70	197.3	0.0503 ± 3.24
OCH12-7 cz02	12	BDS[b]	Yes	251.69 ± 0.67	0.6	1.3	0.2719 ± 3.40	0.03982 ± 0.27	0.63	251.2	0.0495 ± 3.24
OCH12-7 cz04	*12*	*BDS*[b]	*Yes*	247.64 ± 1.01	*0.8*	*1.1*	0.2143 ± 5.06	0.03916 ± 0.42	*0.55*	*224.0*	0.0397 ± 4.84
OCH12-7 cz06	12	BDS[b]	Yes	251.60 ± 2.38	0.4	1.2	0.2170 ± 15.31	0.03980 ± 0.97	0.65	125.1	0.0395 ± 14.70
OCH12-7 cz07	12	BDS[b]	Yes	253.54 ± 1.42	0.9	1.1	0.2671 ± 8.32	0.04011 ± 0.57	0.71	116.5	0.0483 ± 7.92
OCH12-7 cz08	*12*	*BDS*[b]	*Yes*	235.67 ± 4.18	*0.9*	*1.1*	0.0279 ± 247.91	0.03724 ± 1.81	*0.83*	*63.7*	0.0054 ± 246.42
OCH12-7 cz09	12	BDS[b]	Yes	252.82 ± 1.11	0.9	1.1	0.2699 ± 5.48	0.04000 ± 0.45	0.64	172.1	0.0489 ± 5.20
OCH12-7 cz10	12	BDS[b]	Yes	250.83 ± 2.30	1.2	0.9	0.2223 ± 17.97	0.03968 ± 0.93	0.81	78.3	0.0406 ± 17.22
OCH12-7.1 mz01	6	BDS[b]	Yes	252.60 ± 0.61	1.8	1.0	0.2795 ± 0.52	0.03996 ± 0.25	0.65	1880.2	0.0507 ± 0.41
OCH12-7.1 mz02	6	BDS[b]	Yes	252.19 ± 0.37	1.9	1.0	0.2818 ± 0.35	0.03990 ± 0.15	0.53	2002.2	0.0512 ± 0.30
OCH12-7.1 mz03	6	BDS[b]	Yes	252.23 ± 0.60	2.7	1.1	0.2788 ± 0.88	0.03990 ± 0.24	0.41	890.2	0.0507 ± 0.81
OCH12-7.1 mz04	6	BDS[b]	Yes	252.25 ± 0.46	1.6	1.0	0.2818 ± 0.40	0.03991 ± 0.19	0.51	2005.3	0.0512 ± 0.35
OCH12-7.1 mz06	6	BDS[b]	Yes	251.78 ± 0.63	2.0	0.9	0.2821 ± 0.60	0.03983 ± 0.25	0.50	1272.5	0.0514 ± 0.52
OCH12-7.1 z01	6	BDS[b]	Yes	250.32 ± 1.08	2.3	1.1	0.2792 ± 1.56	0.03959 ± 0.44	0.35	511.6	0.0511 ± 1.46
OCH12-7.1 z02	6	BDS[b]	Yes	252.27 ± 0.46	1.8	1.3	0.2828 ± 1.15	0.03991 ± 0.18	0.47	631.8	0.0514 ± 1.08
OCH12-7.1 z03	6	BDS[b]	Yes	251.27 ± 0.57	1.5	1.1	0.2775 ± 1.70	0.03975 ± 0.23	0.50	400.9	0.0506 ± 1.60

Table B.6: Data from the second sampling location at Palo Duro (OCH12-7).